

**DEVELOPMENT OF A MONTE CARLO SIMULATION
TOOL FOR LIGHT TRANSPORT INSIDE SCINTILLATION
CRYSTALS**

By

XIN YANG

A Thesis

Submitted to the School of Graduate Studies

In Partial Fulfilment of the Requirements

for the Degree

Master of Science

McMaster University

© Copyright by Xin Yang, September 2012

Xin Yang

Medical Physics

MASTER OF SCIENCE (2012)

McMaster University

(Medical Physics and Applied Radiation Sciences)

Hamilton, Ontario

TITLE: Development of a Monte Carlo Simulation Tool for Light
Transport inside Scintillation Crystals

AUTHOR: Xin Yang

SUPERVISOR: Professor Thomas Farrell and Professor Hao Peng

NUMBER OF PAGES: xi, 130

Abstract

The scintillation crystal is a critical component in positron emission tomography (PET) systems. It impacts a number of PET system performance parameters, including spatial, energy, and time resolution. Our goal is to develop a new simulation tool to achieve improved accuracy by addressing several limitations in the existing packages (DETECT2000 [Moisan 2007], ZEMAX [Bauer *et al* 2009] and PHOTON [Tickener and Roach 2007]), including more advanced surface treatments, temporal dependency of photon arrival, and rigorous experimental validations. The comparison of preliminary Monte Carlo simulation results and analytical calculations for specular reflection suggest that the simulation model is working well. The time-resolved light output was studied for various crystal surface treatment configurations. The measured energy resolutions are in the range of approximately 10% to 15%, which are in good agreement with published literatures. Based on the simulation and experimental results, the polished surface treatment, used together with an external specular reflector, is able to provide the best energy resolution and timing resolution for a LYSO ($3 \times 3 \times 20 \text{ mm}^3$) and SiPM assembly we tested. The AsCut surface with external diffusion reflector is not desired due to its inferior energy and timing resolutions. The direction and recommendation of improvements of simulation regarding surface models and wavelength dependency, as well as potential optimization of experiment such as timing pickoff methods, are discussed.

Acknowledgements

Over the past two years many kindly people have stood by my side lending a helping hand. Without you, I would have been like a ship with no rudder sailing to nowhere.

I am especially grateful to Dr. Hao Peng, my supervisor, who led me into the domain of medical imaging, guided me through the project and assisted me in every possible aspect—from funding to lab equipment, from research design to conference presentations. An enthusiastic and devoted tutor, your influence on me is profound and everlasting.

To Dr. Thomas Farrell, my co-supervisor, I owe my deepest respect and gratitude. The knowledge of Monte Carlo simulation you provided was a vital part of the project. More importantly, I was constantly inspired, especially in times of confusion and frustration, by your cheerful insight into the research—and into values of life as well. To me, you are more than a supervisor.

My sincerest appreciation also goes to Dr. Kevin Diamond and Dr. Soo-Hyun Byun, whose advice on the project and enlightening lectures I attended were most invaluable. For me, you unlocked the door to an exciting field. The impact is beyond imagination.

Equally, I would like to express my heartfelt thanks to Dr. Troy Farncombe, who generously provided the lab and office and indispensable technical support.

With great appreciation, I want to thank my teammates, colleagues, staff and office secretaries for your encouragement and contributions. Thank you, Evan Downie for building the printed circuit board; Yicheng Liang and Ruibin Dai for teaching me how to use MATLAB; and Nasit Vurgun for assisting me in the experiment.

I am, indebted to nuclear medicine and health physics technologists who supplied radioactive sources, and to people of the machine shop, who helped construct some equipment.

As always, I feel very much blessed and thankful to my parents, who love me, understand me and, sunny and rainy, never lose hope in me.

I also consider myself lucky to have true friends, who are always ready to help. You are a strong shoulder I can rest on anytime.

You are great. I love you all.

(You can be proud that I didn't let you down.)

Table of Contents

Abstract	iii
Acknowledgements	iv
List of Abbreviations	vi
List of Figures	vii
List of Tables	xi
1. Introduction	1
1.1 Nuclear Medicine	1
1.2 PET Physics.....	2
1.3 PET detector developments	14
1.4 Recent Developments of PET Instrumentations	24
1.5 Motivation.....	27
2. Simulation of Optical Transportation within Scintillation Crystals	28
2.1 Background of Monte Carlo Simulation.....	28
2.2 Simulation Procedure.....	30
2.3 Simulation Data Analysis	49
2.4 Simulation Results	65
3. Experimental Validation of Monte Carlo Simulation	69
3.1 Experimental Set-up and Apparatus	69
3.2 Energy Resolution.....	72
3.3 Coincidence Timing Resolution.....	74
3.4 Experimental Results	79
4. Discussions and Conclusion	94
Appendices	
A. Investigation of SNR benefit for a time-of-flight (TOF) PET	103
B. Probability Density Function for Different Sampled Variables	109
C. Design of Light Tight Box and Collimator	112
Bibliography	123

List of Abbreviations

ADC	Analog-to-Digital Converter
APD	Avalanche Photodiode
CDF	Cumulative Probability Distribution Function
CFD	Digital Constant Fraction Discrimination method
DOI	Depth of Interaction
ESR	Enhanced Specular Reflector
FOV	Field of View
FWHM	Full Width at Half Maximum
LOR	Line of Response
MC	Monte Carlo
MRI	Magnetic Resonance Imaging
NECR	Noise Equivalent Count Rate
PDF	Probability Density Function
PET	Positron Emission Tomography
PMT	Photomultiplier Tube
ROI	Region of Interest
SiPM	Silicon Photomultiplier
SNR	Signal-to-Noise Ratio
SPECT	Single Photon Emission Computed Tomography
TOF	Time of Flight
TTS	Transit Time Spread

List of Figures

1.1 Na-22 radioactive decay	2
1.2 Photoelectric effect and Compton scattering	4
1.3 Positron range and Noncolinearity of 511 keV annihilation photons	6
1.4 Illustration of the depth of interaction	7
1.5 Demonstration of various DOI design concepts for PET	8
1.6 Examples of energy spectrum and the definition of energy resolution	9
1.7 Different types of coincidence events for PET	12
1.8 Scheme of the energy band structure in an activated scintillation crystal	15
1.9 Photofraction as a function of effective atomic number of different types of scintillators	16
1.10 Typical shapes of scintillation output signals	17
1.11 Construction of a PMT	21
1.12 Configuration of an APD	23
1.13 A state of art commercial PET/CT by CPS Innovations	25
1.14 Measurement of time-of-flight	25
2.1 Example of PDF of a sampled variable	29
2.2 Probability density function of a uniform distribution	29
2.3 Screenshot of Free Pascal software	30
2.4 The flow chart of simulation procedures for tracking one photon	31
2.5 Screenshot of “test.mon” file	32
2.6 The geometric diagram, surface equations, and definition of surface treatments and reflectors of crystals	34
2.7 Illustration of definition of S_{\min}	37
2.8 Illustration of a random surface and cosine distribution of the diffuse reflection	39
2.9 Schematic demonstration of dot-product expression for specular reflection	39
2.10 Illustration of two mechanisms of Lambertian reflection	40
2.11 The rejection method of sampling lambertian cosine distribution	41
2.12 Schematic demonstration of dot-product expression for refraction	42

2.13 Illustration of the Polish-Metal model and the Polish-Paint models	44
2.14 The geometry and flow chart of simulating “Ground-Paint” model	45
2.15 The simulation of local normal of planar micro-facets	46
2.16 The special cases of check points for directions of incident, reflected, and refracted light on micro-facet of crystal surface	47
2.17 The simulation timing results vs. analytical calculations for optic photons generated at middle points in a 3x3x3 mm ³ crystal	49
2.18 The Bowl-area models of calculating probability distribution for S _{total}	50
2.19 The smallest distance of the detected initially upward launched photon in a 3x3x3 mm ³ crystal	52
2.20 The boundary conditions of downward launched photons without interaction and total internal reflection on any of the four side faces	53
2.21 The boundary conditions of one and two reflections on one of side faces	54
2.22 The boundary conditions for initially upward launched photons	56
2.23 The 3D taper predictions of partial total internal reflections on side faces	57
2.24 The simulation timing results vs. analytical calculations for optic photons generated at different points in various crystals	62
2.25 The verification of exponential distribution of attenuated 511 keV photons	63
2.26 The simulation results of Green’s function approach method and Beer-Lambert exponential for a 3x3x20 mm ³ crystal	64
2.27 Jitter in leading-edge time derivation	65
2.28 Typical simulation propagation time results with selection of two points for rise-time slope calculation	66
2.29 Simulation results of relative light output and reciprocal of rise-time slopes for all four surface-reflectors combinations	68
3.1 Typical raw waveform of a detected signal by the SiPM	71
3.2 Raw waveform capture of detector signals with a free-running ADC	71
3.3 Illustration of experiment setup for energy resolution experiment	72
3.4 Illustration of experiment setup for coincidence timing resolution experiment	75
3.5 Illustration of selecting coincidence events between channel 0 & 1	76
3.6 An example of components for DCFD with PMT and SiPM signals	77

3.7	Illustration of linear (or exponential) rising edge fitting time pick-off method for PMT and SiPM signals	78
3.8	Na-22 energy spectra with Compton continuum for PMT with 1250V and SiPM with 71.5mV bias voltage before calibration	79
3.9	Calibration of channel numbers of ADC and energies with three energy peaks from two radioactive sources for both PMT and SiPM	80
3.10	Calibrated Na-22 energy spectra for PMT and SiPM	82
3.11	A typical calibrated Na-22 energy spectrum using triangular shaping method with Gaussian curve fitting method	83
3.12	Energy resolution versus number of measured annihilation photons	84
3.13	Energy resolution as a function bin numbers used in curve fitting and of triangular shaping parameters G and L.....	86
3.14	A typical coincidence time spectrum using the DCFD time pick-off method	86
3.15	Coincidence timing resolution as a function of the total number of coincidence events	87
3.16	Coincidence timing resolution as a function of the bin numbers used in curve fitting	88
3.17	Coincidence timing spectra of the “S/N 108341” crystal by CFD method for different D_s settings	89
3.18	The time spectra for DCFD, linear & exponential methods	91
3.19	Coincidence timing resolutions as a function of various surface-reflector combinations for three time pick-off methods	93
4.1	The simulation light output and measured energy resolutions of four different surface-reflector combinations for $3 \times 3 \times 20 \text{ mm}^3$ LYSO scintillation crystals	94
4.2	Coincidence timing resolutions of four different surface-reflector combinations for $3 \times 3 \times 20 \text{ mm}^3$ LYSO scintillation crystals for simulation and experiment with DCFD time pick-off method	98
A.1	Different reconstruction methods between conventional and TOF PET	103
A.2	Simulated Shepp-Logan phantom in MATLAB	104
A.3	The principle of back-projection	105
A.4	Examples of TOF-PET image reconstruction method for different kernel sizes and kernel shapes	106

A.5 The reconstructed images by TOF-PET reconstruction method with rectangular kernel shape and kernel sizes	107
B.1 Simulation verification results for comparing three Lambertian distribution sampling methods	111
C.1 Construction and components of designing and the external and internal views the light tight box	113
C.2 Configuration and cross-sectional view of collimator-crystal-source set	115
C.3 Demonstration of different situations and orientations of annihilation photons entrance to collimator	116
C.4 The plot and best-fitted equation of build-up factors	119
C.5 Scheme of inverse-square law contribution of reduction of intensity	120
C.6 The final designed collimator and its removable holder	121
C.7 The plot of I_c/I_0 versus different Z for $X_1=X_2=5$ cm	122
C.8 Example of recommended DOI experiment when annihilation photons are required to enter only the bottom layer of a 20 mm height crystal	123

List of Tables

1.1	Properties of an ideal scintillation crystal for PET scanner system	18
1.2	Properties of typical scintillation crystals for PET	20
2.1	XOR truth table	32
2.2	Definition of surface-reflector combinations	43
2.3	The boundary conditions of total path length for a number of reflections while photons are initially launched downward from a mid-point in a $3 \times 3 \times 3 \text{ mm}^3$ LYSO crystal	55
2.4	Parameters of crystals and reflectors applied in simulations	65
2.5	Statistical uncertainty evaluation results for all surface-reflector combinations	66
2.6	Simulation results of light output and rise-time slopes for four typical reflection coefficients of Teflon tape	67
3.1	The LYSO crystals used in experiments	70
3.2	Measured energy resolutions of $3 \times 3 \times 20 \text{ mm}^3$ LYSO crystals with different surface-reflector combinations	90
3.3	Coincidence timing resolution results for $3 \times 3 \times 20 \text{ mm}^3$ LYSO crystals by DCFD, linear and exponential rising edge fitting time pick-off methods	92
4.1	The terminologies of surface treatment combinations used in experiment and simulation	95
A.1	Size of kernels in terms of pixel numbers and calculated timing resolutions	106
A.2	Comparison between theoretical SNR gain and simulated relative SNR results by TOF-PET image reconstruction method	108
C.1	Parameters of collimator and limitations of Z of the four boundary conditions for $X_1=X_2=5\text{cm}$	120

Chapter 1

Introduction

1.1 Nuclear Medicine

Nuclear medicine is a medical imaging technique that uses tiny amounts of radioactive tracers in the diagnosis and treatment of various diseases, including cancers, neurological disorders, and cardiovascular diseases. The elemental radionuclides are chemically bound to other elements or compounds to form radiopharmaceuticals to be injected to patients [Bailey *et al.* 2005, Chapter 1]. The radiopharmaceuticals could either be inhaled as a gas or be injected into a vein, which are then biologically bound to specific molecules and reveal a number of physiological information, such as cancer malignancy, metabolism, blood flow and cell proliferation [Saha 2010, Chapter 10]. Compared to other imaging modalities such as X-ray and MRI, one major benefit of nuclear medicine is that it is able to provide valuable diagnostic information (e.g., physiological /functional/cellular) in early stages due to its superior molecular sensitivity, well before that can be detected using other imaging modalities. On the other hand, even though nuclear medicine provides nice physiologic information, it offers relatively limited spatial resolution, thus make it unable to delineate fine anatomical structures [Peng and Levin 2010]. Two widely used imaging modalities in nuclear medicine are: Single Photon Emission Computed Tomography (SPECT) and Positron Emission Tomography (PET).

1.1.1 SPECT

SPECT is an imaging technique based on the detection of gamma photons from radiotracers using gamma cameras. The three-dimensional image dataset is formed by applying a tomographic reconstruction algorithm to multiple 2D images acquired at different angles. The common radiotracers used for SPECT include technetium-99m (^{99m}Tc), iodine-123 (^{123}I), and indium-111 (^{111}In) [Wernick and Aarsvold 2004, Chapter 7]. Two major differences between SPECT and PET are the presence of collimators and the need to rotate cameras in SPECT.

1.1.2 PET

PET is a nonvasive imaging technique that is based on the coincidence detection of 511 keV annihilation photons emitted from positron-emitting radionuclides. A positron is first emitted through a nuclear transition process and then travels a short distance (known as *positron range*) [Cherry and Dahlbom 2006], and ultimately annihilates with a surrounding electron to produce two 511 keV annihilation photons that move in the

opposed directions. These two annihilation photons are to be detected in a coincidence window (typically several nanoseconds) by two PET detectors, and form a *line of response* (LOR) that will be used for image reconstruction to identify the original location of annihilation.

The radionuclides used for PET have relatively shorter half-lives than SPECT leads to lower cumulated doses, including ^{11}C (~20 min), ^{13}N (~10 min), ^{15}O (~2 min) and ^{18}F (~110 min) [Bailey *et al.* 2005, Chapter 1]. Similar to SPECT, the 3D image of an object is reconstructed from sets of projections in PET.

1.2 PET Physics

Here, a brief review of PET physics is provided, including several aspects that are highly relevance to PET instrumentation and detector design: physics of positron emission and annihilation, photon interaction in matter, PET system performance and recent advancement of high performance PET system design.

1.2.1 Physics of Positron Emission and Annihilation

Positron emission tomography (PET) employs the decay mode *positron emission* (also known as β^+ , or beta-plus decay), which occurs by converting a proton into a neutron in proton rich isotopes [Bailey *et al.* 2005, Chapter 2]:



where p is the proton, n is the neutron, ν is the neutrino, β^+ is the positron, which is the antiparticle to the electron. Figure 1.1 is the schematic diagram of a typical positron emission isotope, Na-22.

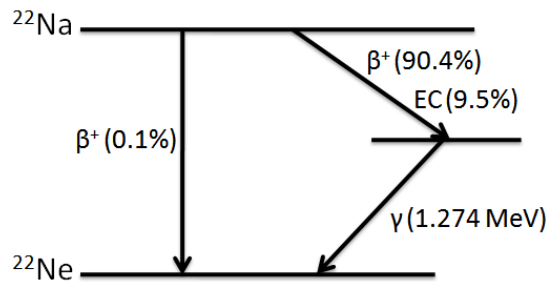


Figure 1.1: Na-22 radioactive decay [Pedroso de Lima J J 2011, Chapter 3]. The positron emission is dominant in low Z (atomic number) nuclei.

The produced positron carries an initial kinetic energy after emission that has a continuous energy spectrum due to a three-body process. The positron travels a distance and deposits its energy by interacting with the surrounding matter. Eventually it combines with an electron at rest, leading to annihilation, where the positron and electron disappear and their mass is converted into two annihilation photons due to the conservation of momentum and energy [Cherry and Dahlbom 2006].

1.2.2 Interactions of 511 keV Annihilation Photons with Matter

Unlike a charged particle depositing its energy continuously through collision with other particles in the surrounding medium, annihilation photons may travel a long distance without any interactions, which is associated with its mean free path and energy. Once an interaction occurs, a photon may deposit a large fraction of its energy to the surrounding medium, such as a patient's body, scintillation crystal, and collimators (lead or tungsten), following the Beer's law below:

$$I = I_0 e^{-\mu x} \quad (1.2)$$

where I_0 is the initial intensity of a mono-energetic ray of annihilation photons, μ is the linear attenuation coefficient, which depends on energy of incidence photon, as well as density and effective atomic numbers of medium. Note that the mean free path is the reciprocal of linear attenuation coefficient: $\frac{1}{\mu}$. For PET, there are mainly two interaction mechanisms involved: photoelectric effect and Compton scattering.

1.2.2.1 Photoelectric effect

A photon transfers all of its energy while it interacts with an orbital electron, which is then ejected from the shell after collision and leaves a vacancy. The kinetic energy carried by the photoelectron is equal to the initial energy of incoming photons minus the shells' binding energy, as illustrated in Figure 1.2 (a). Typically, the vacancy of the ionized atom is quickly filled by capturing an electron from the medium or other shells, which leads to the emission of a characteristic X-ray [Bailey *et al.* 2005, Chapter 2]. Alternatively, the excessive energy can be removed by ejecting an Auger electron from the atom. The probability of photoelectric interaction at a given energy strongly depends on the atomic number and the density of the medium, following a relationship of Z^{3-4} [Magdy and Khalil 2011]).

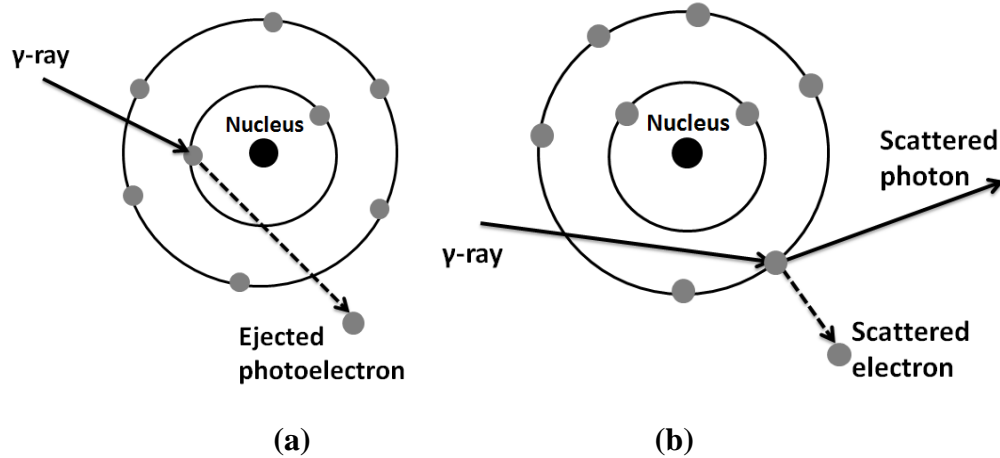


Figure 1.2: Schematic illustration of (a) photoelectric effect, which involves the process of whole energy of incident photon being transferred to an inner shell electron, and (b) Compton scattering, in which only part of energy from incident photon transfers to target electrons that is loosely bound to outer shells [Bailey *et al.* 2005, Chapter 2].

1.2.2.2 Compton scattering

In Compton scattering (Figure 1.2(b)), the incident photon interacts with a loosely bound or free electron, transferring only part of its energy and scattering towards a new direction. Due to the conservation of energy and momentum, the Compton kinetics are described as [Knoll 2000, Chapter 2]:

$$E_{SC} = \frac{E_{Inc}}{1 + \frac{E_{Inc}}{m_0 c^2} (1 - \cos\theta)} \quad (1.3)$$

where E_{SC} is the energy of photon after scattering, E_{Inc} is the incidence energy of photon, θ is the scattering angle, $m_0 c^2$ is the rest-mass energy of electron (511 keV). For 511 keV incidence energy, this equation reduces to:

$$E_{SC} (keV) = \frac{511}{2 - \cos\theta} \quad (1.4)$$

The probability of Compton scattering interaction at a given energy is linearly proportional to the atomic number of medium (Z). The angular distribution of scattered photons is predicted by Klein-Nishina equation and is strongly dependent on the energy of incoming photons [Cherry *et al.* 2003].

It should be pointed out that another photon interaction process, Rayleigh scattering, occurs at low energy level (less than 50 keV) and in those mediums of high atomic number. For PET, it is often neglected in annihilation photons interaction since there is almost no energy transferring after interaction, except the deflection of the photon's path (also known as "elastic scattering"). However, the effect of Rayleigh scattering is not negligible when modeling the light transportation, especially for low energy visible light (scintillation light) since the angle of deflection decreases as its energy increases [Bailey *et al.* 2005, Chapter 2]. Another interaction, pair production, occurs for photons having an energy exceeding 1.022 MeV and is not relevant to PET.

1.2.3 PET system performance.

1.2.3.1 Spatial resolution

The spatial resolution in PET imaging is defined as the minimum distinguishable and detectable distance between two points of an image. It determines the system's ability to resolve small lesions and identify fine anatomical structures of interests. A mathematical expression of spatial resolution in PET is described as follows [Pedroso de Lima J J 2011, Chapter 5]:

$$\text{Resolution}_{\text{FWHM}} = 1.25\sqrt{(d/2)^2 + (0.0022D)^2 + S^2 + b^2} \quad (1.5)$$

where d is the crystal width, D is the diameter of the detector ring, s is the effective source size (or positron range), the factor of 1.25 is due to image reconstruction, b is a factor empirically determined from BGO block detectors that ranges from 0 to 2.2 depending on specific detector designs [Moses and Derenzo 1993].

Besides this empirical expression, some other factors that determine the spatial resolution are discussed below.

- Positron range

As mentioned above, positron travels a short distance (losing most of its energy by interacting with electrons) after it is emitted from nucleus and then undergoes annihilation process with an electron. As a result, the true annihilation location is not exactly the position of emission and the spatial resolution is degraded. This distance is called the *positron range*, which follows a cusp-like distribution and typically has a full-width-half-

maximum (FWHM) ranging from 0.3 to 4 mm in water, depending on the positron's energy of different isotopes [Cherry et al. 2003, chapter 18].

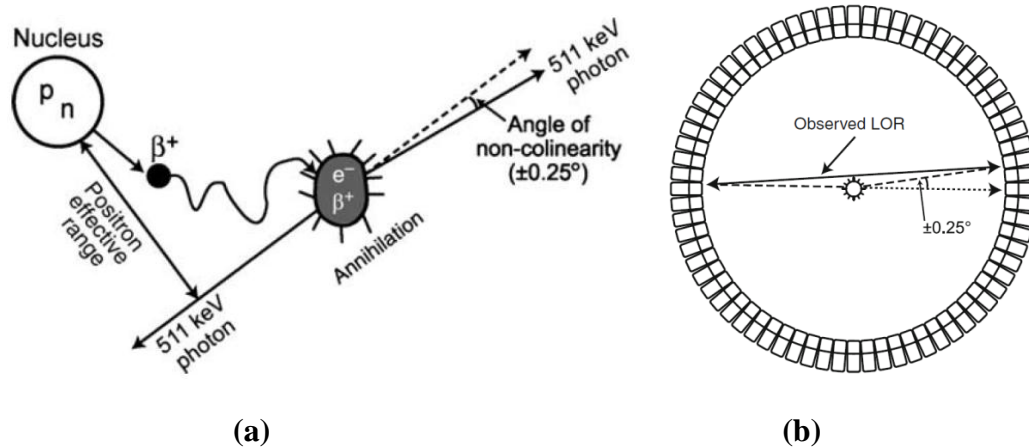


Figure 1.3: (a) Illustration of positron range and noncollinearity effects (b) Noncollinearity of 511 keV annihilation photons along LOR between detectors. Both effects degrade the spatial resolution of PET system [Saha 2010].

- Non-collinearity

PET detects two coincidence photons travelling along nearly the opposite direction ($\sim 180^\circ$). Due to the fact that there is some residual momentum (or kinetic energy) when the annihilation occurs, a LOR does not exactly pass through the annihilation site as illustrated in Figure 1.3. The degree of deviation from 180° , of a magnitude of $\pm 0.25^\circ$ (or 0.5° FWHM), is called the *noncollinearity* (or *acollinearity*) effect which gives rise to the displacement from the annihilation position and thus degrades spatial resolution. Such degradation is dependent on a PET system's diameter and leads to the term of $0.0022 \times D$ term in (Eq. 1.5). For example, a typical whole-body PET of 80 cm diameter will suffer a resolution degradation of 1.76 mm FWHM, due to the noncollinearity effect.

- Parallax error

The parallax error is another resolution limiting factor which results from the absence of information about the *depth of interaction* (DOI) of the 511 keV photons within the detectors. In particular, when the coincidence events occur at the edges of the transaxial *field of view* (FOV) with oblique angles instead of the centre FOV, PET detectors are unable to determine the accurate annihilation position as explained in Figure 1.4). The spatial resolution can be degraded by up to 40% of FWHM (approximately 3 mm) for a clinical PET system when the source is located 10 cm away from the center, and it increases linearly as a function of the radial distance [Cherry et al. 2003, chapter 18].

Increasing the system's diameter or deploying shorter crystals can help mitigate the DOI effect. However, the two solutions will comprise the detection efficiency of 511 keV annihilation photons.

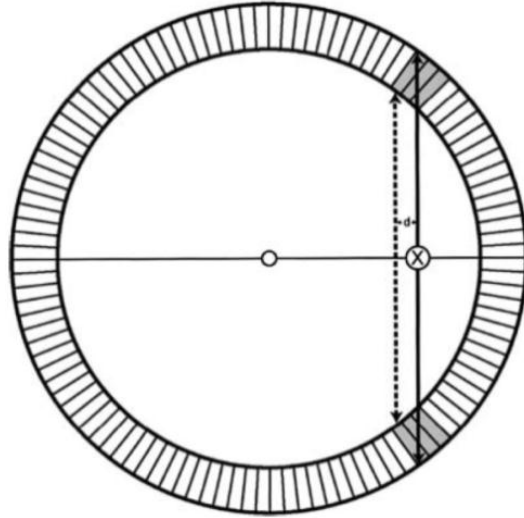


Figure 1.4: Illustration of the depth of interaction (DOI). The annihilation photons interact in neighboring crystals and produce incorrect line of response if no DOI information is provided. [Pedroso de Lima Chapter 3].

Another solution to address DOI challenges is through novel detector design of depth-encoding capability [Ito *et al.* 2010, Maas *et al.* 2009, Ling T *et al.* 2008, Yang Y *et al.* 2009, Du H *et al.* 2009], as illustrated in Figure 1.5. One design is to use phoswich detector [Carrier *et al.* 1988, Mosset *et al.* 2006, Du *et al.* 2009] by using two different types of crystals with significantly different decay times and obtaining the DOI information based upon pulse shape (i.e., rise/decay times). Another design is to deploy dual-layer photodetector/crystal assembly [James *et al.* 2009, Levin *et al.* 2002, Rafecas *et al.* 2001, Yang *et al.* 2006, Yang *et al.* 2008]. A simple example is placing photodetectors at both ends of scintillation crystals and the relative amplitude (i.e., number of scintillation photons) of signals from two photodetectors provide the DOI information.

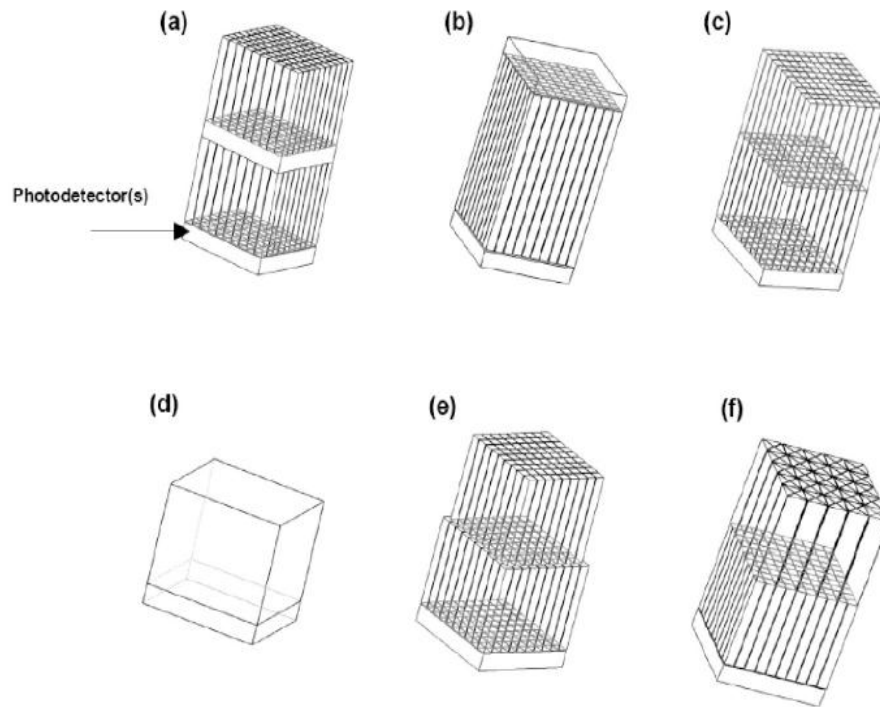


Figure 1.5: Demonstration of various DOI design concepts for PET. (a) Dual crystal-photodetector(s) layers. (b) Single crystal layer with photodetectors at each end. (c) Phoswich design with two different types of scintillation materials. (d) Statistical positioning with a monolithic crystal block. (e) Dual layer crystals with offset positions. (f) Dual layer crystals of mixed shapes [Peng and Levin 2010].

Another two critical performance parameters of a PET system are energy resolution and time resolution achievable with high performance PET detectors, which rely on several design aspects including scintillator materials, crystal dimension, surface treatment and reflectors, photodetectors, as well as readout electronics and signal processing. The optimization of energy resolution and time resolution of a clinical PET detector is the primary focus of this thesis. In this work, energy resolutions and coincidence timing resolutions of pairs of scintillation crystals along an 180° LOR of different crystals were measured in order to investigate light outputs as a function of crystal configurations (please see Chapter 3 for more details).

1.2.3.2 Energy Resolution

One important property of radiation detection system is energy resolution, which is ability to discriminate incoming signals of similar energies. Good energy resolution is desired to reject Compton scatter efficiently by setting a lower energy threshold.

The performance of a radiation detection system is commonly characterized using a specific distribution called *response function* [Knoll 2000, Chapter 4], as illustrated in

Figure 1.6. In reality, the width of photo-peak is always broader due to a large amount of fluctuation from pulse to pulse and that the peak is mathematically described by a Gaussian distribution instead of a delta function. The width of full energy peak reflects the system's *energy resolution* and its capability to separate two adjacent energy peaks. Note that, in real energy spectra, due to the incomplete deposition of energy by incident radiation, such as energy lost due to Compton scatter of 511 keV photons, there exists a continuous region (Compton continuum in Figure 1.6) locating at the left-side (i.e. lower energies) of the full energy peak.

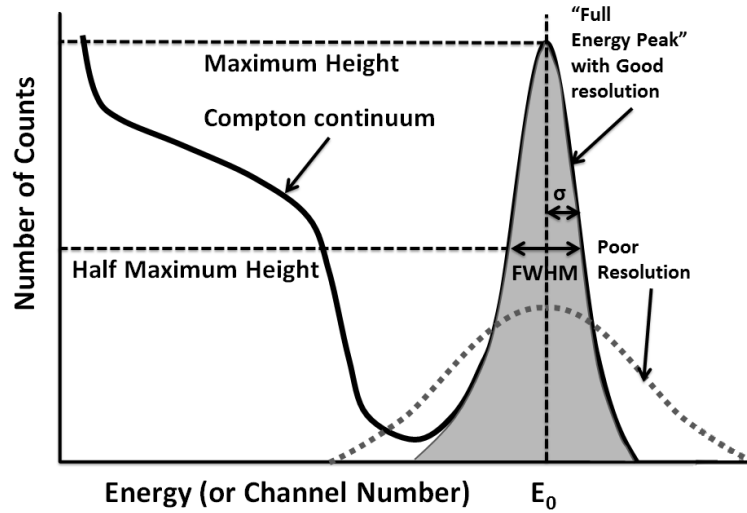


Figure 1.6: Examples of energy spectrum and the definition of energy resolution. Good energy resolution (green peak, solid line) and poor energy resolution (dashed line) are provided for comparison. Given the same area under each peak, the ideal response of a detector exhibits a very narrow peak.

The energy resolution (in percent) is quantitatively defined as:

$$R = 100\% \times \frac{\text{FWHM}}{E_0} \quad (1.6)$$

where E_0 is peak center (or the energy of the incident radiation), FWHM mathematically defines the width (or fluctuation) of the full energy peak. Besides other physical factors affecting the energy resolution such as non-linearity of light emission in scintillator materials and photodetectors, the statistical fluctuation in the process of converting the deposited energy into signal carriers to be detected by photodetectors can be modelled as a response function of Gaussian-shape:

$$\text{FWHM} = 2.355\sigma \quad (1.7)$$

$$G(E) = \frac{A}{\sigma\sqrt{2\pi}} e^{\left(-\frac{(E-E_0)^2}{2\sigma^2}\right)} \quad (1.8)$$

where σ is the standard deviation and E_0 is the energy of the incident radiation (or peak position).

Under the assumption that the generation of signal carriers follows Poisson statistics such as in a scintillator and photomultiplier assembly, the peak amplitude and the standard deviation can be quantitatively defined in the following way: for a given number of N charge carriers, E_0 is proportional to N as:

$$E_0 = kN \quad (1.9)$$

where k is a proportionality constant; the standard deviation is $k\sqrt{N}$, which further gives as:

$$\text{FWHM} = 2.355k\sqrt{N} \quad (1.10)$$

Consequently, the energy resolution due to Poisson statistics only is [Knoll 2000, Chapter 4]:

$$R = \frac{\text{FWHM}}{E_0} = \frac{2.355K\sqrt{N}}{KN} = 2.355 \frac{1}{\sqrt{N}} \quad (1.11)$$

This important equation implies that the energy resolution is fundamentally limited by the number of signal carriers to be detected.

Besides Poisson statistics, there are a number of additional factors affecting the energy resolution, such as noise from detector electronics (R_{noise}) and operating conditions during measurements (R_{others}), such as detector stability [Knoll 2000, Chapter 4]:

$$R_{\text{overall}}^2 = R_{\text{statistical}}^2 + R_{\text{noise}}^2 + R_{\text{others}}^2 \quad (1.12)$$

The contributions of R_{noise} can be further divided into two parts [Dorenbos *et al.* 1995, Dorenbos 2002]:

$$R_{\text{noise}}^2 = R_S^2 + R_M^2 \quad (1.13)$$

where R_S and R_M are resolution terms associated with scintillator and PMT, respectively. R_S consists of two parts: transfer resolution (R_p) and crystal intrinsic energy resolution

(R_i). R_p is determined by quantum efficiency (QE) of PMT, optical coupling between crystal and PMT, crystal surface coating, and transmittance of the scintillator, etc. R_i refers to the crystal's intrinsic energy resolution and is mainly associated with the inhomogeneity of crystals, which cause both local variations in the scintillation light output and the non-proportionality effect of scintillator light output as a function of the annihilation photons' energy [Kelly et al. 1956, Prescott and Narayan 1969].

1.2.3.3 Coincidence Timing Resolution

In PET, two 511 keV annihilation photons traveling along two opposite directions are detected by a pair of detectors. The detector's ability to determine the arrival time information of incoming radiation is referred as the coincidence timing resolution, which is typically around 2-6 ns for conventional PET. In practice, a time window of twice the width of the time resolution is applied to reject those random (also known as accidental) annihilation photons.

It is very likely that the coincidence events of two annihilation photons will be detected by the two detectors along LOR owing to the 180° property. These two coincidence photons are emitted from anywhere within the FOV of PET therefore there is always a timing difference owing to the annihilation photons' propagation. For instance, for a typical 80 cm diameter conventional PET, the maximum of this arrival time difference could be 2 to 3 ns, which means the timing window is not able to be reduced less than 2 to 3ns even with an ideal detector system (very fast scintillation crystals with extremely small timing resolution).

For a typical PET detector configuration including scintillator and photodetectors, a generalized framework has been developed to investigate the physical factors that limit the time resolution of a PET detector [Spanoudaki and Levin 2011]:

$$t_{\text{event}} = t_{\text{flight}} + t_{\text{DOI}} + t_{\text{OTT}} + t_{\text{CTT}} \quad (1.14)$$

where t_{flight} is the flight time of 511 keV annihilation photons from the site of annihilation to the front surface of the detector, t_{DOI} is the combination of two processes: 1) propagation time of annihilation photons from the front surface edge of detector to the interaction sites; and 2) subsequent flight time of the generated scintillation photons (unscattered) within the crystal to the location of photodetector, t_{OTT} is the optical transit time of scintillation photons experiencing significant scattering within crystals, and t_{CTT} is the transit time of photoelectrons before they are detected and form the signal to be

processed. Here the timing fluctuation due to the photodetector's response and electronics is assumed to be identical for individual detectors.

As a result, the overall timing resolution can be described using the formula below: [Spanoudaki and Levin 2011]:

$$\Delta t_{\text{overall}} = \Delta t_{\text{flight}} + \Delta t_{\text{DOI}} + \Delta t_{\text{OTT}} + \Delta t_{\text{CTT}} \quad (1.15)$$

The Δt_{DOI} and Δt_{OTT} terms are inherent timing resolution from scintillation crystals. Superior timing resolution leads to higher NECR, as to be discussed in the next section, since the ability of rejecting random events is improved. The importance of timing properties of scintillator-based detectors facilitates different groups to contribute their efforts for investigating the temporal limits of PET [Binkley *et al.* 1994, Clinthorne *et al.* 1990, Moses *et al.* 2006, Moszynski *et al.* 1996, Petrick *et al.* 1991, Post and Schiff 1950].

1.2.3.5 Random & Compton coincidences

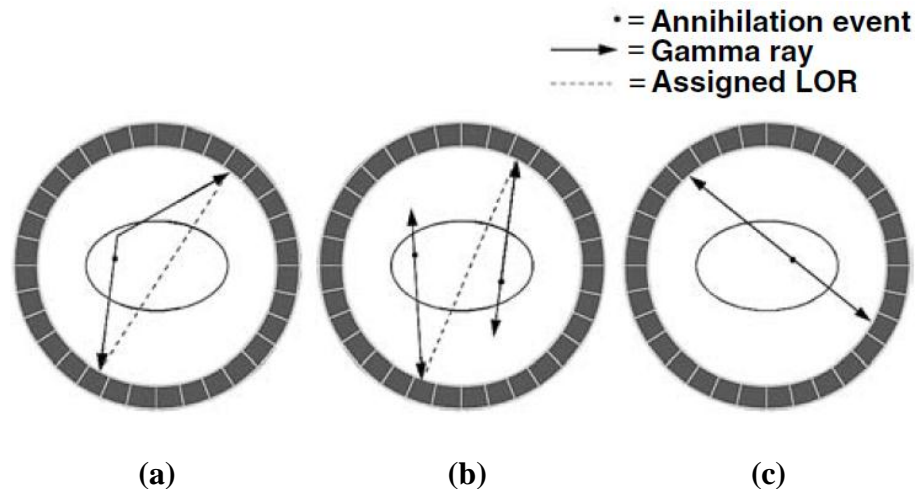


Figure 1.7: Three different types of coincidence events for PET: (a) scattered coincidence, (b) random coincidence, and (c) true coincidence [Wernick and Aarsvold 2004].

The ideal photon detection condition, or called *true coincident* event (Figure 1.7(c)), requires two 511 keV photons are detected by a detector pair along the LOR passing through the emission position. In practice, however, this is actually not achievable since usually some undesired background types of events are happening. *Random coincidences* (Figure 1.7(b)) are one of those events. Random coincidences occur as a result of detecting two unrelated annihilation coincident events from two separate positions are detected by detector pair along the LOR within the same time window. This results in a

high background image, false position information, and reduction of the image contrast. The random coincidence rate in a PET scanner is estimated as [Magdy and Khalil 2011]: $R_{ij} = 2\tau S_a S_b$, where 2τ is the time window for coincidence events (τ is the time resolution of the system), S_a and S_b are the singles rates of two detectors a and b, respectively defining a given LOR. From the above equation, one way to reduce the random coincidence rate is to applying narrow coincidence timing window during data acquisition. Hence, a fast detector with superior timing resolution is necessary. On the other hand, the number of true events is reduced if applying a shorter timing window. Therefore there is a trade-off between reduction of undesired events and sensitivity [Magdy and Khalil 2011].

The *scatter coincidence* (Figure 1.7(a)) is another common undesired type of events. Due to the Compton scattering of 511 keV photons in the patient, annihilation photons might change their direction from their true LOR without much loss of energy, resulting in the situation that one true annihilation photon and one scattered photon or both scattered photons fall within the same coincidence time window. This could produce false position information and reduce the image contrast as well. One way to correct this type of event is applying a narrow energy window around 511keV photopeak. Since the amount of energy lost is relatively small, excellent energy resolution is necessary to reject the scatter coincidence without compromising photon sensitivity. These undesired coincidence events are acting as background noise in reconstructed image.

The noise equivalent count rate (NECR) accounts for a better measure of signal-to-noise ratio, *SNR*, and it provides a link between image *SNR* and those coincidence events [Strother *et al.* 1990]:

$$\text{NECR} = \frac{T^2}{S+T+kR} \quad (1.16)$$

where T, S, and R are the trues, scatter, and random rates, respectively; k is a constant (between 1 and 2) that depends on the phantoms/organs being imaged [Peng and Levin 2010].

1.2.3.4 Sensitivity

Another challenge of PET system development is detection sensitivity of 511 keV annihilation photons. The sensitivity of a PET scanner is defined as the number of counts per unit time detected by the system for each unit of activity present in a source [Saha

2010]. Sensitivity is mainly determined by geometric and intrinsic efficiency discussed below. A higher sensitivity will allow for improved counting statistics and image quality. The sensitivity is around 1-3% and 6-9% for a clinical and small animal PET system, respectively.

The intrinsic efficiency depends on several physical properties of scintillation crystals, including effective atomic number, density, thickness and decay time. For a point source at the center of a single ring scanner, the intrinsic efficiency is described as [Magdy and Khalil 2011]:

$$\varepsilon_i = (1 - e^{-\mu l})^2 \quad (1.17)$$

where μ is the linear attenuation coefficient for 511 keV annihilation photons and l is the thickness of detector. Note that higher intrinsic efficiency could be achieved by increasing the crystal's thickness. However, this benefit can only be achieved at the cost of DOI errors (see section 1.2.3.1).

The geometric efficiency is defined by the fraction of 4π covered by the solid angle covered by the PET detectors [Magdy and Khalil 2011]. High geometric efficiency requires a large detector surface area or/and smaller diameter of the PET ring. However, similar to intrinsic efficiency, simply decreasing the system's diameter would introduce more DOI errors and compromise the uniformity of spatial resolution. Another factor affecting the geometric efficiency is packing fraction, which refers to the ratio of the effective detection area to the total circumferential ring area [Wong 1988] and is associated with detector packaging and system integration.

1.3 PET detector developments

1.3.1 Scintillation Crystals

Scintillation detectors, which are classified into organic (aromatic hydrocarbons) and inorganic (alkali halides or oxides) materials, are widely used in radiation detection. Due to its high stopping power, which is characterized by the linear attenuation coefficient, for high energy annihilation photons and good light yield, inorganic scintillators are the primary choice for PET imaging. To avoid confusion, it is important to emphasize that two types of photons are involved in the operation of scintillation detectors: high energy annihilation photons (511 keV annihilation photons) and low energy optical photons (scintillation light of a few eV).

1.3.1.1 Scintillation Mechanism

In inorganic crystal, scintillation light generation is characterized by the energy band structures as shown in Figure 1.8.

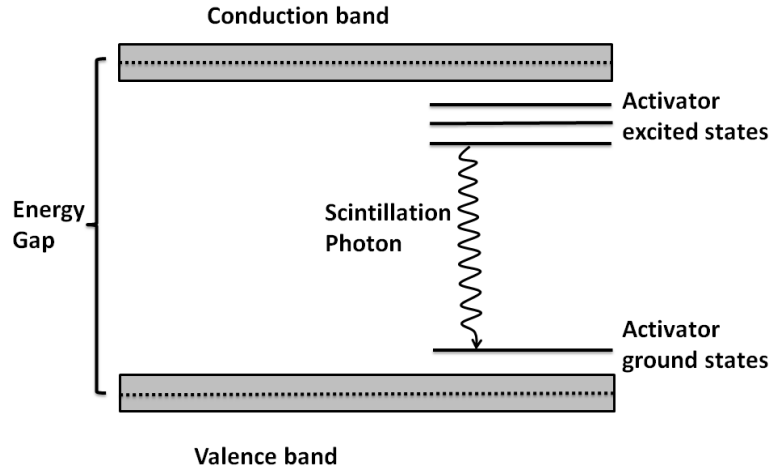


Figure 1.8: Schematic diagram of the energy band structure in an activated scintillation crystal. Optical photons are emitted by de-excitation of electrons back to valence band. [Bailey *et al.* 2005, Chapter 2].

The energy gap between conduction band and valence band is typically on the order of a few eVs (~4-12 eV). Once those electrons in the valence band absorb energy through photoelectric (PE) or Compton Scatter (CS) with incoming 511 keV annihilation photons, they will reach to the conduction band crossing the forbidden band, leaving holes in the valence band and creating electron-hole pairs. Subsequently, the elevated electrons de-excite and return to the ground states by releasing scintillation photons. However, large band gaps typically exist between the conduction band and the valence band, which limit the efficiency of conversion process. To address this problem, most inorganic scintillation crystals contain impurities in forbidden bands, also called activators, in order to adjust the band gap suitable for the emission of visible light photons to be detected by photodetectors [Derenzo and Weber 2003]. The overall efficiency of converting the deposited energy of a annihilation photon to scintillation light photons is characterized as below [Magdy and Khalil 2011]:

$$\eta = \beta S Q \quad (1.18)$$

where β is conversion efficiency of γ -ray energy to electron hole pairs, S is the efficiency with which the electron hole pairs transfer energy to luminescence centers, and Q is the quantum efficiency of the luminescence centers.

1.3.1.2 Properties of scintillation crystals

For radiation detection, it is desirable to have scintillation crystals of large atomic number, high density, good light yield, as well as fast time response. Photoelectric and Compton scattering are the two major interaction mechanisms for detecting 511 keV annihilation photons [Magdy and Khalil 2011], as discussed in section 1.2.2. Photofraction is commonly used as a measure of relative probability of these two interactions and is defined as:

$$\varepsilon = \frac{\sigma_p}{\sigma_p + \sigma_c} \quad (1.19)$$

where σ_p and σ_c are cross section of photoelectric effect and Compton scattering, respectively. The probability of PE interaction for 511 keV photons as a function of Z_{eff} is shown in Fig, which increases continuously as Z_{eff} increases. On the other hand, the attenuation length is also dependent on Z_{eff} , which defines the mean distance that a photon travelled before it deposits its energy. A short attenuation length (i.e. high *stopping power*) is desired in order to stop 511 keV annihilation photons effectively [Moses 2002]. This also results in improvement of the parallax effect as discussed in 1.2.3.1 since no requirement of relatively large size of scintillator.

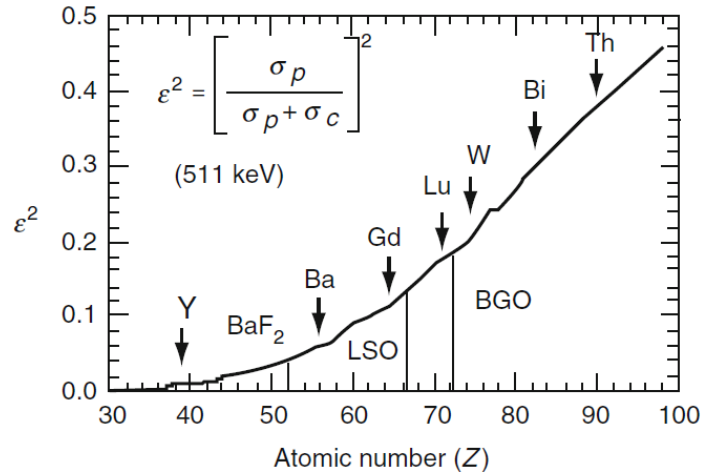


Figure 1.9: Photofraction as a function of effective atomic number of different types of scintillators. The ε^2 indicates the type of interaction of both 511 keV photons is photoelectron [Moses and Derenzo 1996].

Light output, also called light yield, is another important physical property of crystals. It is defined as the number of scintillation photons per energy deposited, usually in units of photons/MeV. Higher light output is advantageous in several aspects for PET detectors, such as energy resolution, timing resolution as well as spatial resolution [Aykac *et al.*

2006, Dorenzo *et al.* 2003]. Besides the high light output, increasing light detection efficiency and mitigating light loss is also important. The loss of scintillation light during propagation to the photodetector occurs by self-absorption or transmission on crystal surfaces, which can be minimized by applying various types of reflection coatings around crystals [Knoll *et al.* 1988, Janecek and Moses 2010].

As shown in Figure 1.10, another important property of scintillation crystal is the *decay time* from the excited state back to the ground state, which determines how fast the scintillation photons are created after an annihilation photon deposit its energy. A short decay time is desirable in order to reject random coincidence events efficiently, as well as to handle high counting rates (e.g., short-lived radionuclides with high activities and/or 3D PET). For energy measurement, a scintillation crystal of large decay time will have long tail on its output signal, which is more likely to suffer from the pile-up effect [Knoll 2000, Chapter 17]. For time measurement, a fast scintillator has a high rate of photon emission and leads to output pulses of fast *rise time*. As to be seen in section 1.4.2, this is of particular importance for TOF-PET.

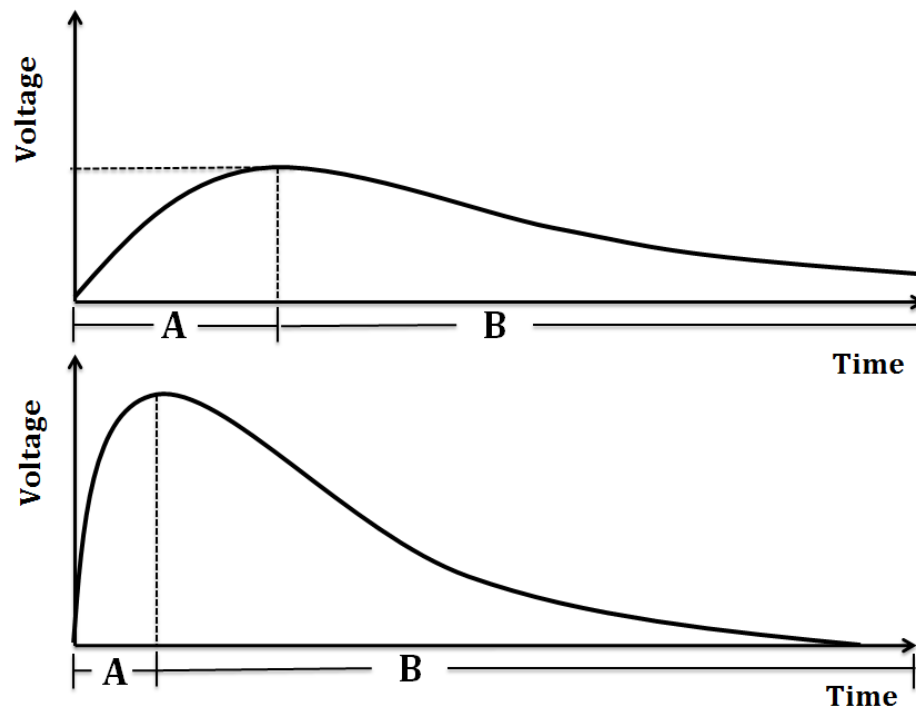


Figure 1.10: The typical shape of scintillation output signals for two extremes of large (top) and small (bottom) time constants. The region A and B represents the rise and decay time constants, respectively. Fast rise time is associated with fast time performance, and fast decay time helps to minimize the signals pile-up effect.

Table 1.1 lists all of the major physical and scintillation properties for an ideal scintillator.

Table 1.1: Properties of an ideal scintillation crystal for PET scanner system [Melcher 2000].

Crystal Property	Purpose
High density, high atomic number	High γ -ray detection efficiency
Short decay time	Good coincidence timing
High light output (yield)	Allow higher fraction of crystal elements per photodetector and higher energy & time resolutions
Emission wavelength near 400 nm	Good match to photodetector response
Transparent to Emission wavelength	Avoid self-absorption for high collection efficiency and less light loss
Index of refraction (in the range of 1.4 to 2.2)	Good transmission of visible light from crystal to photodetector
Nonhygroscopic/Rugged	Facilitate packaging and allows for small crystal elements fabrication

1.3.1.3 Common inorganic scintillation materials

The overall performance of high stopping power, high light output and fast timing response of scintillation crystal indicates a way to choose a suitable scintillator for PET system. Table 1.2 lists the typical scintillators used for PET.

Thallium activated sodium iodide, or NaI(Tl), was the primary choice for PET and SPECT imaging system back to 1970s due to its high light output ability leading to good energy ($\sim 41,000$ photons/MeV) [Lecomte 2009]. However, owing to its low detection efficiency for 511 keV photons and poor timing resolution leading high random coincidence events, NaI(Tl) is not frequently used in application of PET (still extensively being used in SPECT). Another limitation of NaI(Tl) is its hygroscopic property which means hermetical sealing is required to prevent moisture effects.

Bismuth germanate oxyorthosilicate (BGO) replaced NaI(Tl) and had become the most extensively used scintillator for many years until the end of 1990s [Cherry *et al.* 1995] due to the superior high detection efficiency for 511 keV annihilation photons, as well as the high photofraction and nonhygroscopic nature. However, the decay time (slow

response) and light output ($\sim 12,000$ photons/MeV) leading to poor energy resolution are inferior compared to other crystals which makes BGO not suitable for fast timing usage, such as TOF-PET.

Lanthanum bromide (LaBr_3) is a relatively new scintillation material [van Loef *et al.* 2001] and studies are contributed to investigate performance of this type of crystal [Witherspoon *et al.* 2008]. Despite hygroscopic property (again, hermetic sealing is required), LaBr_3 has excellent performances such as high light output ($\sim 60,000$ photons/MeV), high photofraction, and very short decay time which make itself a good candidate for TOF-PET application. However, in order to have enough stopping power, generally larger size of LaBr_3 crystal is desirable attributing to its lower detection efficiency and lower photofraction (spatial uncertainty due to multiple scattering), thus DOI information is required with less parallax effect.

Lutetium orthosilicate (LSO), or a similar version, Lutetium Yttrium orthosilicate (LYSO) has been considered as the most common choice nowadays for PET, particularly for TOF-PET because of the combination of advantages of high light output of NaI ($\sim 30,000$ photons/MeV) and high detection efficiency of BGO [Moses 2002], as well as the fast response: short decay time as 40 ns (or 47 ns [Ludziejewski 1995]) and short rise time as 0.5 ns [Shao 2007]. Usually LSO (or LYSO) is doped with Cerium in order to further improving the performance [Lempicki *et al.* 1998, Spurrier *et al.* 2008]. Note that the major difference between LSO and LYSO is that LYSO is easier and cheaper to grow since some lutetium is replaced by yttrium atoms [Qin *et al.* 2005]. Despite introducing some amount of yttrium [Pepin *et al.* 2004], conventionally, LSO shares the same parameters, such as density, decay time and output, with LYSO. Similar to BGO, LSO (LYSO) is nonhygroscopic and it is mechanically possible to produce small sizes of crystal. However, non-proportionality effect, which leads to degradation of energy resolution, is one of the main limitations of LSO (LYSO) crystal. Another disadvantage for LSO (LYSO) is the presence of self-radioactive (β^- decay) isotopes (^{176}Lu , 2.6 % abundance) [Bailey *et al.* 2005, Chapter 2]. However, the impact of these isotopes is negligible in clinical PET scanner (except dedicated small animal PET [Humm *et al.* 2003]) since the background counts coming from these isotopes is about 12 per second per gram and only within the 126-154 keV energy window (PET has much higher energy windows). Therefore, for scintillation crystal in PET, LSO (or LYSO) is a good choice of balancing all the properties without compromising others too much.

Table 1.2: Properties of typical scintillation crystals for PET [Magdy and Khalil 2011]. Note that the two values of decay times for GSO are because of the multi-exponential pulse shapes.

	Nal(Tl)	BGO	GSO:Ce	LSO:Ce	LYSO:Ce	LaBr ₃	BaF ₂
Density (gm/cm³)	3.67	7.13	6.7	7.4	7.1	5.3	4.89
Effective atomic number (Z)	51	74	59	66	64	47	54
Linear attenuation coefficient (1/cm)	0.34	0.92	0.62	0.87	0.86	0.47	0.44
Light yield (% Nal[Tl])	100	15	30	75	75	160	5
Decay time (ns)	230	300	6.5 60	40	41	16	0.8
Emission maximum (nm)	410	480	440	420	420	370	220
Hygroscopic	Yes	No	No	No	No	Yes	Slightly
Photoelectric effect (%)	17	40	25	32	33	13	12
Refractive Index	1.85	2.15	1.85	1.82	1.81	1.88	1.56

1.3.2 Photodetectors

After the creation of scintillation photons in crystals, these visible photons are detected by photodetectors in the form of electrical signals. However, this electrical signals needs to be amplified as a consequence of weak light output (or less amount of photons) of the scintillation pulse. Also, to ensure sufficient amount of scintillation photons are collected, optical grease is usually coupled between scintillators and photodetectors as a way of matching the index of refraction of these two media so that more scintillation photons experience transmission to photodetectors instead of reflection back to scintillators. The photodetectors for PET system are essentially sorted into two groups: *photomultiplier tubes* (PMT) and *solid-state photodetectors* [Cherry and Dahlbom 2006].

1.3.2.1 Photomultiplier tubes

Figure 1.11 schematically depicts standard structure of a PMT, which essentially consists of a photocathode (e.g. bialkali with peak sensitivity at 420 nm), a series of multiplication stages (electrodes called *dynodes*) and an anode. All of the components are enclosed in a vacuum environment by borosilicate glass.

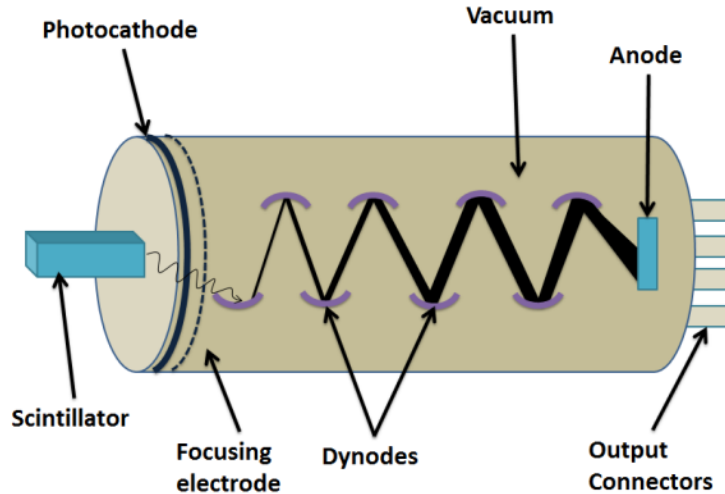


Figure 1.11: Construction of a PMT. The photoelectrons are accelerated and multiplied by applied high operating voltage. The figure is reproduced based on [Cherry et al. 2003].

When scintillation photons strike the entrance window (photocathode), electrons can be released by photoelectric effect if the photon energy could overcome the inherent potential barrier (or workfunction) in order to reach the energy level of the vacuum [Meschede 2007]:

$$E_{kin} = hv - W \quad (1.20)$$

where W is the workfunction, hv is the photon energy, and E_{kin} is the rest of photon energy (or kinetic energy of the electron). The secondary produced electrons are called photoelectrons, which are then accelerated towards the first dynode with a higher energy due to the present of electric field. The probability of liberating a photoelectron in photocathode is described by so-called *quantum efficiency* of PMTs, which is wavelength dependent and has typical value of 20-30% [Knoll, Chapter 9]. The scintillator emission spectrum should match to the absorption spectrum of photodetector in order to have higher quantum efficiency.

After the strike on the first dynode, more photoelectrons are emitted and migrating to the second dynode in which even more photoelectrons are in turn liberated from dynode.

This process is repeated 10 to 12 times (dynodes) results in a cascade of electrons which are finally collected in anode. The signal for one scintillation photon is amplified with commonly a factor (*gain*) of 10^5 to 10^7 [Wernick and Aarsvold 2004]. Another important property of PMTs is the transit time, which is the propagation time required for photoelectrons moving from photocathode to anode during multiplications, and the transit time spread (TTS), which is the fluctuation of transit time. The properties such as high gain, stability, low dark current, linear amplification of the signal, and low noise (higher SNR) enable PMTs to detect small scintillation signals. Besides the conventional type, there are other advanced modes of PMTs which are commercially available, for instance multichannel plate PMTs, that consist of parallel compact microchannels and fast response; or Position sensitive PMTs, which have multiple anodes and are able to provide spatial distribution of scintillation light from crystal.

1.3.2.2 Semiconductor Photodetectors

Photodiodes

The principle of semiconductor (solid-state) photodetectors is similar to that of scintillation crystals, containing valence, conduction, and forbidden bands. The excited electrons are liberated and leave positive holes in valence band. As in scintillation crystals, several discrete energy levels within the forbidden band are created by doping impurities. The semiconductor photodetectors are named *p-type* if the discrete energy levels are closer to valence band from which electrons are easily liberated or *n-type* if the discrete energy levels are closer to conduction band such that electrons are easily to elevate. A depletion region is created due to the drifting of electrons and holes. The thickness of this depletion region is determined by the applied reverse bias voltage [Knoll, Chapter 13]. The electrons created in the depletion region drift toward the n-side (holes toward p-side) due to the applied electric field. This results in the flow of charges (current) that is measured by an external circuit. However, the internal gain of conventional photodiodes does not increase significantly.

Avalanche Photodiodes

The operation principle (Geiger mode) for avalanche Photodiodes (APD) is essentially the same as that of photodiodes except for a higher applied voltage (or electric field) (Figure 1.12).

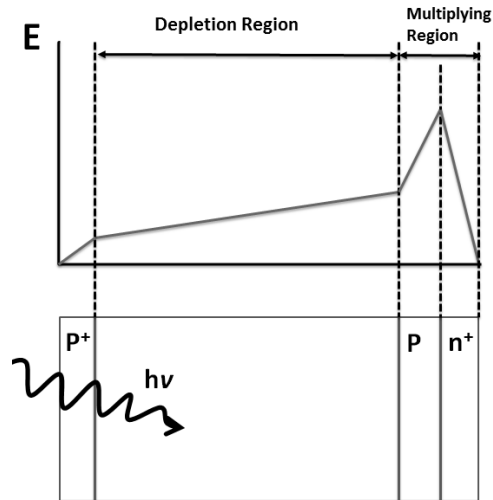


Figure 1.12: Configuration of an APD (top) and the resulting electric field with applied bias voltage (bottom). This figure is reproduced based on [Knoll 2000, Chapter 9].

If the bias voltage is higher than a limit, or *breakdown voltage*, the excited electrons gain sufficient energy to ionize silicon atoms so that more secondary electrons are created. These secondary electrons are accelerated by the electric field and further ionize more atoms result in avalanche effect. Note that a quenching circuit is required for stopping avalanche effect. The quantum efficiency of photodiodes (or APD) is much higher than that of PMT (60% to 80%) since photoelectrons are not required to escape from photocathode surface as in PMT (to overcome workfunction). Also, the transit time is much shorter owing to the thin active layer of photodiodes so that the timing performance is better than that of PMT. Another advantage of photodiodes is its compact size allowing close packing (reduce dead space in PET), plus magnetic fields retardant, lower cost, and low operation voltage, etc. However, the lower gain (10^2 to 10^3) of APD comparing to that of PMT (again, 10^5 to 10^7) limits its application in PET system since energy or timing performances are determined by gain (even though APD has shorter transit time) [Wernick and Aarsvold 2004]. In addition, the gains of APD are sensitive to temperature changes and variation of applied bias voltage. Therefore, additional signal amplification are electronics usually incorporate with APDs, which are operated at intermediate gains.

Silicon photomultipliers

Although PMTs are still the reliable benchmark candidates of photodetectors, recently, the disadvantages of PMTs (expensive, magnetic sensitive, large size, and lower quantum efficiency) make researchers starting to focus on investigation of PET by applying

semiconductor photodetectors [Saha 2010]. Silicon photomultiplier (SiPM), or generally multipixel photon counter (MPPC), is the novel version in photodiodes family. SiPMs comprise highly packed matrix of APD pixels ($25 \times 25 \mu\text{m}^2$ - $100 \times 100 \mu\text{m}^2$) that are connected in parallel and are all operated in Geiger mode. The output signal of SiPM thus is proportional to the number of operating pixels (or summation of outputs from each pixel). Therefore, the high gain characteristic of SiPMs (10^5 to 10^6) is associated with the existent advantages of photodiode, and this leads to the fact that SiPM has been becoming a popular photodetectors for PET [Renker and Lorenz, 2009]. Additionally, the amplification circuit used for APD is not necessary for SiPM. Note that although semiconductors have relatively high quantum efficiency, the photo detection efficiency (20% to 70%) depends on other factors as well, for instance ratio of effective active area to total area of SiPM (space between APD pixels required for resistors, etc). Therefore larger area of one APD pixel is desirable for higher detection efficiency. On the other hand, the dynamic range is dropped by reducing number of APD pixels if the area of each pixel is increased. Another major issue for SiPM is its relatively high thermal dark count rate due to the free carriers in conduction band (0.1 to 10 Mcps). Digital SiPM (dSiPM) which is commercially available from Philips [Degenhardt et al. 2009, Frach et al. 2009] is the advanced version of conventional SiPM. The output signals from dSiPM are converted into digital signals by internally integrated time-to-digital converter.

1.4 Recent Developments of PET Instrumentations

1.4.1 Multimodality

Nowadays, almost all of the PET systems are incorporated with a CT scanner owing to the excellent anatomic/functional localization from CT and powerful molecular imaging strength from PET. Also, the high-resolution anatomic information from CT can correct for annihilation photon attenuation correction [Beyer *et al.* 1995]. A dual modality system of PET-CT has already been developed since 1998 [Townsend *et al.* 1998]. Figure 1.13 shows a PET/CT system manufactured by CPS Innovations. Due to the superior soft-tissue contrast of Magnetic Resonance Imaging, i.e. MRI (but limiting sensitivity to reveal metabolites), another dual modality candidate is the simultaneous PET-MRI which is technologically more challenging than PET-CT, particularly for brain imaging [Schlemmer *et al.* 2008]. In order to successfully integrate these two imaging systems, PET has to be insensitive to magnetic field (replace the photodetectors) and compact, plus minimize interfere with the magnetic field gradients and radiofrequency pulses of MRI [Pichler *et al.* 2010].

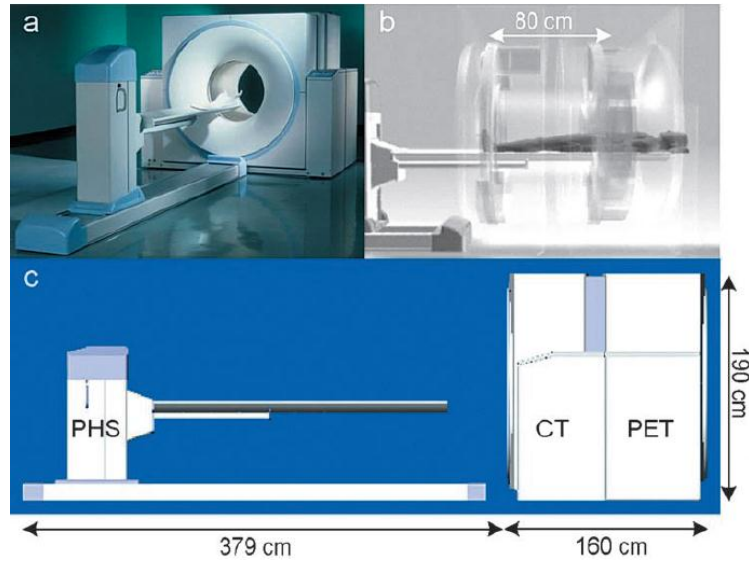


Figure 1.13: (a) Demonstration of a state of art commercial PET/CT by CPS Innovations (b) Patient positioned within the tunnel during a PET acquisition. (c) Basic dimensions of components [Wernick and Aarsvold 2004].

1.4.2 Time-of-Flight PET

As mentioned, in PET imaging, two coincident annihilation photons are emitted from the annihilation position and reach two detectors along LOR. This annihilation position could be directly determined by the difference of arrival times of the two annihilation photons [Budinger 1983]:

$$\Delta t = \frac{2\Delta x}{c} \quad (1.21)$$

where c is the speed of light in vacuum, Δx is the distance from the center of LOR to annihilation position and Δt is the difference of photons travel times (Figure 1.14). Note that this equation is only true for homogeneous objects.

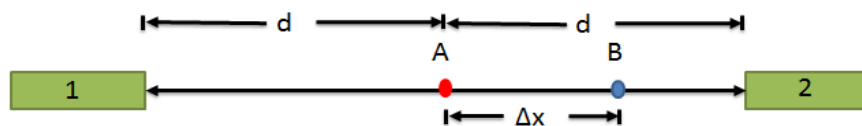


Figure 1.14: Measurement of time-of-flight. A is the middle point between two detectors, and B is the location of annihilation. For instance, for a 1 ns coincidence timing window, the position of annihilation occurs at 15 cm from the center of LOR since light travels about 30 cm/ns in air.

The annihilation position would ideally be a point (delta function) if the Δt is determined accurately. However, due to the limitation of detector performance (e.g. light propagation in scintillation crystals), there is an uncertainty of determining the position (Δx) according to the time difference of arrival photons (Δt), which is limited by the coincidence timing resolution of two PET detectors. Therefore, a good timing resolution (small coincidence time window) not only indicates the ability of rejecting random events, but also how well the spatial resolution could be determined. At the time of introduction of TOF PET in 1980's, the scintillation crystals either have poor stopping power and low light output (such as CsF or BaF₂), or slow timing performance (such as BGO). The progress of developing TOF PET was slow due to this limitation until early 1990's [Allemand *et al.* 1980, Lewellen *et al.* 1988, Mazoyer *et al.* 1990, Pogossian *et al.* 1982, Wong *et al.* 1984]. The renaissance of TOF PET started later when faster PMTs, stability of electronics, advanced image reconstruction methods, and new generation of scintillation crystals with fast timing performance and high light output (such as LSO, LYSO) were introduced to the world [Karp *et al.* 2005, Kuhn *et al.* 2004, Moszynski *et al.* 2006, Schaart *et al.* 2010]. Nowadays, a coincidence timing resolution of several hundreds of ps is achievable. The first commercial TOF PET was introduced by Philips in June 2006 with 600 ps time resolution [Surti *et al.* 2007]. However, the time resolution of 600 ps is not enough to improve the spatial resolution since the typical spatial resolution of whole body PET is a few mm. The important attribute of TOF PET is the improvement of statistical properties of PET image by reducing noise due to the image reconstruction procedures [Karp *et al.* 2008, Moses *et al.* 2007]. Note that Eq. (1.21) helps to back project over the position uncertainty, Δx , instead of whole LOR for conventional PET in image reconstruction. Therefore the source of background noise is only from Δx rather than the whole LOR. This leads to an improvement of SNR (SNR gain) for TOF PET compared with conventional PET [Budinger 1983]:

$$\frac{\text{SNR}_{\text{TOF}}}{\text{SNR}_{\text{Non-TOF}}} = \sqrt{\frac{D}{\Delta x}} = \sqrt{\frac{2D}{c \cdot \Delta t}} \quad (1.22)$$

where D is the patient diameter, Δx is the position uncertainty.

From the above equation, SNR gain benefit increases as timing resolution improves (smaller value) or larger size of patients (heavy patients) who usually have relatively poor image quality due to more attenuation and scatter [Karp *et al.* 2008]. It should be pointed out that extraction of the DOI information is typically considered for small animal PET systems since DOI is dominant in small FOV. However this DOI information can be incorporated with TOF in the development of dedicated PET systems for specific organs (e.g. breast and brain) [Heiss *et al.* 2004, Zhang *et al.* 2007]. Since sensitivity is

incorporated with SNR, the advantage of gain in SNR can be translated into an effective sensitivity gain [Budinger 1983]:

$$\text{Sensitivity Gain} = \frac{2D}{c\Delta t} \quad (1.23)$$

Hence, the improvement of timing resolution not only benefits the random events rejection but also improves the system in the same way as increase in sensitivity.

Please see appendix A for investigation of SNR gain for TOF PET.

1.5 Motivation

Our group aims to develop a whole body PET/MRI system of both depth-of-interaction (DOI) and time-of-flight (TOF) capability with the use of silicon photomultipliers (SiPMs) based Anger scintillation block detector technology. The scintillation crystal is a critical component in positron emission tomography (PET) systems. It impacts a number of PET system performance parameters, including spatial, energy, and time resolution. The temporal resolution is of particular importance for the development of PET systems of TOF capability that use novel scintillation crystal materials (i.e., LaBr₃) and photodetector technologies.

The benefits of Monte Carlo simulation of light transport are significant in its ability to predict the performance of real light transport systems before they are built such that the complex system are optimized without manufacturing expensive testing equipment. Presently, DETECT2000 is mainly applied for simulating the scintillation light emission and transportation process in the detector [Cayouette *et al.* 2002, Magdy and Khalil 2011, Moisan 2007, Saha 2010]. The validation, however, of DETECT is not provided or perfectly explained. They have not been thoroughly validated with experiments, in particular for the modeling of various surface treatments.

Recently, many published papers aimed to study the light output and energy & spatial resolution of crystals with various surface treatment, including the type of reflectors, and the results indicate a highly dependency of light output on different types of reflections on crystal surface [Heinrichs *et al.* 2002]. Timing information is the primary concerning for TOF-PET. Therefore our main attention is focusing on improving timing resolution of appropriate candidate crystals for TOF-PET. Hence, in this study, our goal is to develop a new TOF-PET dedicated simulation tool to achieve improved accuracy by addressing several limitations in the two existing packages, including more advanced surface treatments, temporal dependency of photon arrival, and rigorous experimental validations.

Chapter 2

Simulation of Optical Transportation within Scintillation Crystals

2.1 Background of Monte Carlo Simulation

Monte Carlo method (MC) simulation, which is named from a gambling city in Monaco, is a numerical stochastic technique on the basis of repeated random number sampling for solving probability statistical problems. MC methods are extremely useful in different applications such as modeling particle transport, dosimetry calculations for radiation therapy, evaluating financial investment behavior and regulating flow of traffic. By implementing theoretical algorithms, MC allows us to examine complex systems that are otherwise impossible to investigate with conventional analytical methods. One of the most frequent applications of MC is simulating the radiation transport of particles such as electrons, neutrons, and photons in various propagation media. To facilitate this, there are several MC codes available such as Electron Gamma Shower (EGSn) for coupled electron-photon transport [Bielajew *et al.* 1994], GEometry ANd Tracking (GEANT4) for high energy physics [Allison *et al.* 2006], Monte Carlo Neutral Particle (MCNPn) for nuclear reactor simulations [Briesmeister 2000], and Geant4 Application to Tomographic Emission (GATE) for PET, SPECT and CT simulations [Strul *et al.* 2003]. Since MC requires a tremendous number of events, fast and novel processors leading to high computation performance are beneficial to make the process more practical and feasible, for instance implementation of Graphics Processing Unit. As mentioned previously, one of the major MC codes among light transportation toolkits such as ZEMAX [Bauer *et al.* 2009] and PHOTON [Tickener and Roach 2007] is DETECT2000, which is adopted for the light transportation toolkit in GEANT4 and GATE packages.

MC models the optical behavior numerically and efficiently and tracks history of each photon by tracing their three-dimensional trajectories, or path length. MC simulates actual detector characteristics (i.e. dimensions and geometries) as well as considering physical interaction principles such as scatterings and reflections, and thus the information regarding these interactions such as scattering and absorption coefficients and indices of refraction are required. After the photon is terminated by internal absorption or exiting crystal by transmission, the next photon is then initialized and the entire process will be repeated again.

MC is subject to statistical uncertainty and depends on the accuracy of mathematical models. The number of simulated photons has to be sufficient for acceptable statistical uncertainty. Two million photons were used in these simulations in order to avoid statistical fluctuation. In addition, it is crucial to build a model that includes all of the

factors present in actual situations. The models include stochastic variables representing the various previously mentioned factors in different physical processes (e.g. position and direction of photons) and these variables, x , are randomly sampled from probability distributions that are expressed as functional forms called probability density functions (PDF, or $\text{pdf}(x)$ in Figure 2.1). Each variable has its own PDF.

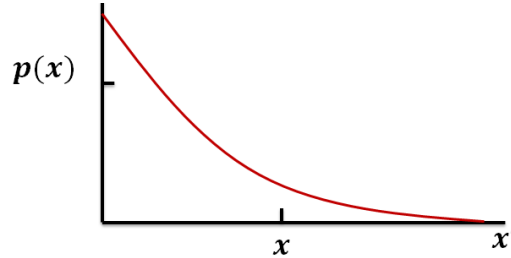


Figure 2.1: Example of PDF of a sampled variable.

The stochastic models convert some uniformly sampled pseudo random numbers to a known probability distribution. As shown in Figure 2.2, the probability density function of the continuous uniform distribution over interval $[a, b]$ is:

$$p(xr) = \begin{cases} \frac{1}{b-a} & \text{for } a \leq xr \leq b \\ 0 & \text{for } xr < a \text{ or } xr > b \end{cases} \quad (2.1)$$

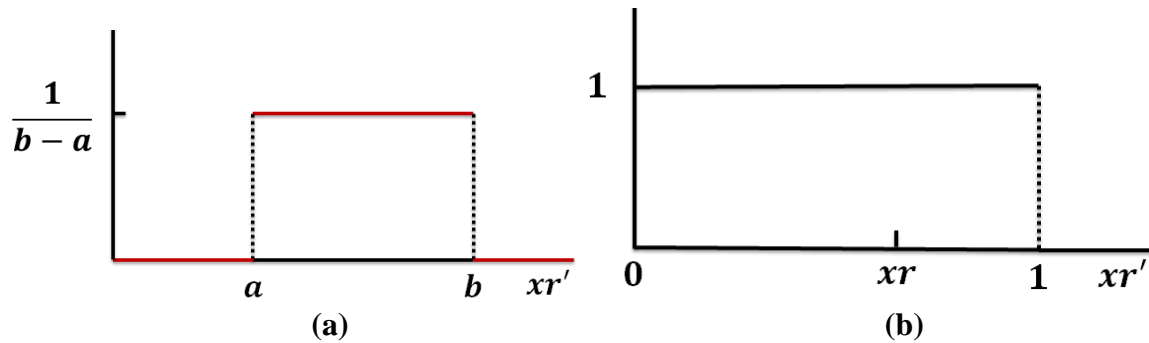


Figure 2.2: (a) Probability density function of a uniform distribution in interval of $[a, b]$. (b) The random numbers are usually sampled from 0 to 1, thus the relative PDF is one within interval $[0, 1]$.

The fundamental principles of MC imply that the probabilities of the sampled variable, x , have to be equalized to the probabilities of the random number, xr , by:

$$p(x')dx' = p(xr')d(xr') \quad (2.2)$$

Integrating on both sides,

$$\int_0^x p(x')dx' = \int_0^{xr} p(xr')d(xr') \quad (2.3)$$

The integration of pdf(x) over interval [0, x] is called cumulative probability distribution function, cdf(x). To obtain functions of variables on random numbers, the random numbers are incorporated with cdf(x).

$$\int_0^x p(x')dx' = xr = \text{cdf}(x) \quad (2.4)$$

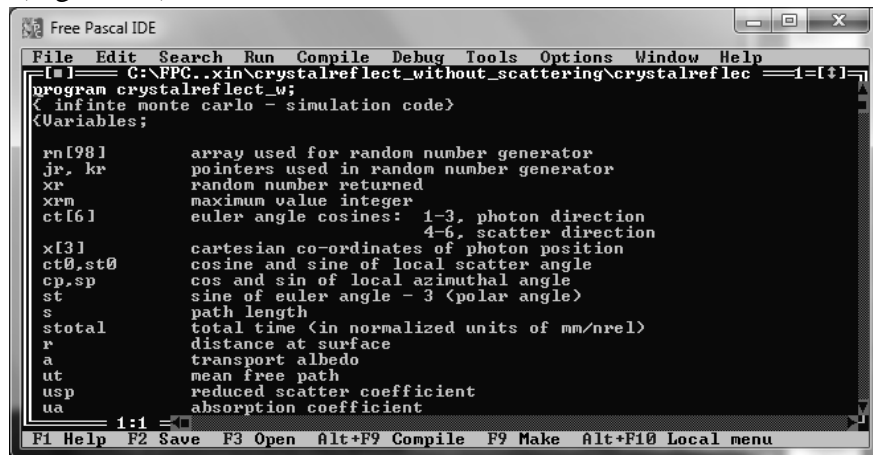
Then the variables x are solved by the inverse distribution method of random sampling and are applied into MC code:

$$x = \text{cdf}^{-1}(xr) \quad (2.5)$$

However, it is not always the situation that this inverse function is possible or simple to solve. In such cases, a powerful alternative sampling method, called rejection method, can be used, and thus the procedure of solving any complex equation is avoided. Instead of sampling only one variable, x, with one random number, two random numbers, xr_1 and xr_2 , are sampled in rejection method. One of them is used to sample a value of x while the other is used to check if this value is acceptable as a properly sampled value. If it is not, then a new random number representing x is generated until the condition is fulfilled. Faster simulation speed can be achieved because some of complicated and time consuming calculations such as trigonometric functions are avoided.

2.2 Simulation Procedure

Our Monte Carlo simulation was based on the PASCAL programming language because of the available framework from previous studies. The relative compiler was *Free Pascal* (Figure 2.3).



```

Free Pascal IDE
File Edit Search Run Compile Debug Tools Options Window Help
C:\NPGC..xin\crystalreflect_without_scattering\crystalreflec 1:1
program crystalreflect_w;
< infinite monte carlo - simulation code >
(Variables;
rn[98]      array used for random number generator
jr, kr     pointers used in random number generator
xr         random number returned
xrm        maximum value integer
ct[6]      euler angle cosines: 1-3, photon direction
           4-6, scatter direction
x[3]       cartesian co-ordinates of photon position
ct0,st0    cosine and sine of local scatter angle
cp,sp      cos and sin of local azimuthal angle
st         sine of euler angle - 3 (polar angle)
s          path length
stotal     total time (in normalized units of mm/nrel)
r          distance at surface
a          transport albedo
ut         mean free path
usp        reduced scatter coefficient
ua         absorption coefficient
1:1
F1 Help F2 Save F3 Open Alt+F9 Compile F9 Make Alt+F10 Local menu

```

Figure 2.3: Screenshot of Free Pascal software.

The general procedure of tracking photons and relative physics are introduced in this subsection. The overall structure of our simulation model is illustrated in Figure 2.4.

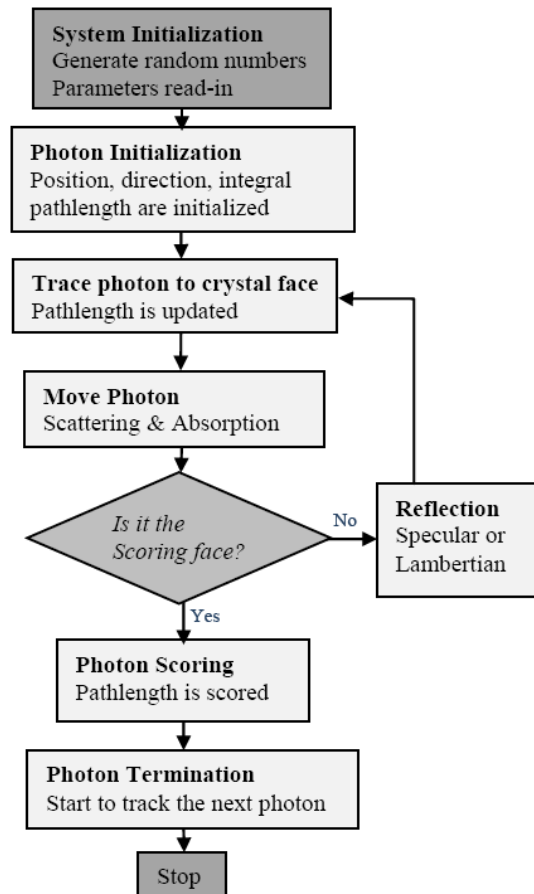


Figure 2.4: The flow chart of simulation procedures for tracking one photon.

2.2.1 System Initialization

The first step was the initialization of the simulation including random number generation and input parameters. The random numbers in our simulation were generated in an isolated file, called 'rand98.dat', rather than within the main program file which was named as 'crystalreflect_w.pas'. The 'rand98.dat' had 98 changeable numbers. One of these 98 numbers (e.g. at the i^{th} array) was first selected, and another number located at the next 27th number relative to the first selected number, i.e. $(i+27)^{\text{th}}$, was selected too. Then these two selected numbers were compared each other based on *exclusive or* (i.e. xor) method (Table 2.1)

Table 2.1: XOR truth table.

INPUT		OUTPUT
A	B	A XOR B
0	0	0
0	1	1
1	0	1
1	1	0

If the output was not zero, the i^{th} number was then divided by the maximum value integer which was always 32767, and this eventually generated a random number which was between 0 and 1.

Refer to Figure 2.5 for the parameters such as geometric parameters defining the crystals (normal vector information, length, and width of crystal faces), interaction lengths, attenuation coefficient of 511keV annihilation photons, and reflectance properties of the crystal walls (i.e. relative indices at surface and reflection coefficients of different reflectors) that were loaded from an independent file, called ‘test.mon’. The final simulation results were written in this file as well.

```

test - Notepad
File Edit Format View Help
Owner
xin
Relative indices at surface - Reflection coefficient of specular/diffusion coating
1.820 0.985 0.950
Attenuation coefficient of 511keV gamma rays (mm^-1)
0.087
Interaction, scatter, and absorption lengths of optical photons (mm)
138.000 138.000 0999999996000.000
Russian Roulette: Number of reflections - Survival Fraction
1000 0.250
Thousands of photons: Done - Total
0 2000
Number of Crystal Faces
6
Normal vector information of faces: (x, y, z, b)
0.0000 1.0000 0.0000 0.5000
-1.0000 0.0000 0.0000 0.5000
0.0000 0.0000 1.0000 20.0000
0.0000 -1.0000 0.0000 0.5000
1.0000 0.0000 0.0000 0.5000
0.0000 0.0000 -1.0000 0.0000
width and Length of crystal face (mm)
1.000000000E+00 20.000
Now the data:
0.000000000E+00 0.000000000E+00 0.000000000E+00 0.000000000E+00 0.000000000E+00
0.000000000E+00 0.000000000E+00 0.000000000E+00 0.000000000E+00 0.000000000E+00
7.980000000E+03 7.762000000E+03 7.369900391E+03 7.682950195E+03 7.220000000E+03
3 3.691873535E+03 3.669260010E+03 3.640444580E+03 3.597079102E+03 3.570000000E+03

```

Figure 2.5: Screenshot of “test.mon” file. The numbers on the bottom were number of scored photons at different bins, where each bin corresponds to 0.1 mm of total path length.

Refer to Table 1.2, in our simulation, the linear attenuation coefficient of LYSO was 0.086 mm^{-1} , the index of refraction for LYSO scintillator was 1.81, decay time was 41 ns, and the rise time was assumed to be 0.5 ns which was the rise time for LSO [Shao 2007].

However, the available data of rise time for scintillation pulses is very limited [Seifert *et al.* 2010] in which paper measurement of rise time (90 ps) of LYSO crystal has been reported. The reflection coefficient of ESR (specular) and Teflon Tape (Lambertian) were both 98.5%. However, experimental measurements of these reflection coefficients vary from group to group leading to significant uncertainties of predicting absolute simulation results. Generally reflection coefficients of ESR (around 98.5% at peak wavelength) have good agreement between different groups [Motta *et al.* 2005, Pepin *et al.* 2001] and the data sheet provided by the manufacturer. However, reflection coefficients of Teflon Tapes vary from 92% to 99% among different publications [Barton *et al.* 2007, Cherry *et al.* 1995, Labsphere 1998, Pepin *et al.* 2001, Saoudi *et al.* 2000, Waldwick *et al.* 2007, Weidner *et al.* 1981]. The index of refraction of the scintillator is also important as this determines how efficiently optical photons can be transmitted from the scintillator to the photodetector. The effect of large mismatches in index is more significant at the scoring face (i.e. scintillator-photodetector boundary) than that at the reflection surfaces since the light transmission to the photodetector is reduced due to significant total internal reflection, whereas most of the refracted photons can still be reflected back to scintillator by reflection coatings.

Conventionally, the shape of scintillation crystal is a rectangular parallelepiped. Note that other geometries of crystals such as a trapezoidal design can also be expressed by these equations with different orientation of normal vectors. The shape of the crystal was mathematically expressed by the following equations of normal vectors with different faces (Figure 2.6 (a)(b)). By definition, the normal vector of a face is perpendicular to its own face. Assuming the normal vectors of all six faces were pointing outward, the equation of one face was:

$$\vec{n} \cdot \vec{r} = ax + by + cz = D \quad (2.6)$$

where D was the distance from origin to location of the face, \vec{n} was the unit normal vector (a, b, c), \vec{r} was the Cartesian coordinate system. For instance, refer to Figure 2.6 (a)(b), the normal vector of face ① was (0, 1, 0) and distance D is $w_y/2$, where w_y was the width of the crystal on the y-axis, therefore the final equation of face was:

$$\vec{n}_1 \cdot \vec{r} = 0 + y + 0 = D = \frac{w_y}{2} \quad (2.7)$$

or, simply $y = w_y/2$.

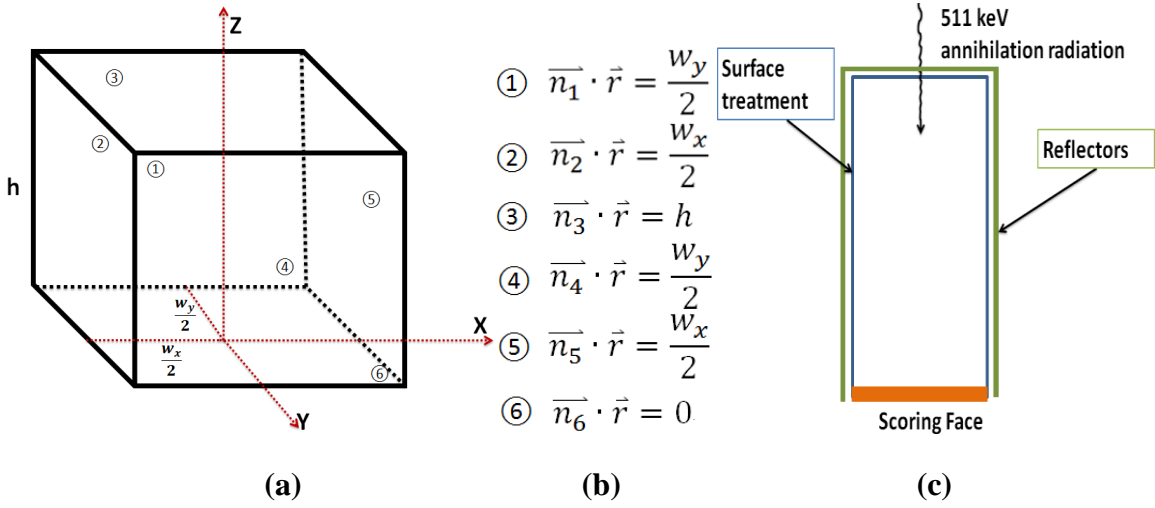


Figure 2.6: (a) The geometric diagram of crystals. (b) Surface equations. (c) Definition of surface treatments and reflectors. The origin of our coordinate system was set at the middle of the scoring face. h was the height (or length) of the crystal, W_x and W_y were widths of the crystal in x and y direction, respectively.

The origin was set at center point of bottom face (i.e. face 6 in Figure 2.6 (a)), which was the exiting face for scoring. The remaining five faces were reflection faces with or without reflection coatings. The entrance face of 511 keV annihilation photons was appointed as the top face (i.e. face 3 in Figure 2.6 (a)).

2.2.2 Photon Initialization

The initial phase vector of each photon was initialized in the second step. This includes position, direction, integral path length, wavelength, etc. sampled randomly from appropriate probability distributions.

At any stage of propagation, directional cosines, which refer to the cosine of the angle from the cardinal axes, were used to represent the direction of each photon. Each photon was assumed to be launched isotropically, thus the mathematical expression of initial direction of each generated photon was:

$$\vec{ct} = \begin{pmatrix} ct_x \\ ct_y \\ ct_z \end{pmatrix} = \begin{pmatrix} \sin\theta \cos\varphi \\ \sin\theta \sin\varphi \\ \cos\theta \end{pmatrix} \quad (2.8)$$

where \vec{ct} was directional cosine of a photon, $\cos\theta$, $\sin\theta$, $\sin\varphi$, $\cos\varphi$ were associated

with random number, xr as follows:

$$\begin{cases} \cos\theta = 1 - 2 \cdot xr = 2 \cdot xr - 1 \\ \sin\theta = \sqrt{1 - \cos^2\theta} \\ \varphi = 2\pi \cdot xr \\ \cos\varphi = \sqrt{1 - \sin^2\varphi} \end{cases} \quad (2.9)$$

The random numbers for sampling θ and φ are not equal to each other. For derivations of all of PDF, please see Appendix B for details.

The locations of photons were expressed by three points: X, Y, and Z correspond to x-axis, y-axis, and z-axis components respectively. The new positions of tracked photons with a displacement of S, direction of photon, and present positions were expressed as follows:

$$\vec{r} = \begin{pmatrix} X \\ Y \\ Z \end{pmatrix} = \begin{pmatrix} X_0 + S \cdot ct_x \\ Y_0 + S \cdot ct_y \\ Z_0 + S \cdot ct_z \end{pmatrix} \quad (2.10)$$

where x, y, z were new positions, S was path length, $X_0, Y_0,$ and Z_0 were current positions. At photon initialization status, S was equal to zero so that the new position was the current position

At initial positions, the optical photons were uniformly generated in x-y directions, and exponentially distributed in z-direction due to exponential attenuation of 511 keV high-energy photons in the crystal according to Beer-Lambert law. Therefore, the X, Y, and Z were associated with random numbers as follows based on their specific PDF:

$$\begin{cases} X = (xr - 0.5) \cdot W_x \\ Y = (xr - 0.5) \cdot W_y \\ Z = \ln[1 + (e^{\mu h} - 1) \cdot xr] / \mu \end{cases} \quad (2.11)$$

where μ was linear attenuation coefficient and W was the width of the crystal if W_x was equal to W_y .

Ideally, each photon was tracked until it was terminated according to different

conditions such as scoring, absorption and transmission. Then another new photon was supposed to be tracked again. A more advanced method called survival weighting technique was used in our simulation. This technique is as follows: once any photon is at a situation of termination (except scoring), this photon is assumed to have survived but with a reduced weight based on survival probabilities, which are associated with reflection or absorption coefficients. Then this weight-reduced photon was continuously tracked until the photon was scored. For example, assuming the weight of a photon was initially 1, after it reflected on a reflection surface with reflection coefficient of 97%, this photon would either be killed by a chance of 3% or it would be still alive but with a new weight of 0.97.

The survival-weighting technique can speed up the simulation since the tracking time would not be wasted for a photon which was supposed to be killed. Plus, this technique can reduce the variation since the sample numbers (or number of sampled photons) in output results was invariant with respect to the initially generated photon numbers. Therefore, initially the photon weight starts at one, and numbers of reflections and/or scatterings are set to zero in initial status of simulated photon.

2.2.3 Determination of Photon Direction

The initial direction for the photon was sampled randomly from an isotropic distribution. The nearest face that corresponds to this direction was determined in this step before launch of this photon to that face. The trajectory of each photon was tracked along propagation path length (or S) with this known direction of photon, and any intersection with only the nearest crystal face was considered by combining equations of photon's new anticipated position (Eq. 2.9) with equations of crystal faces (Figure 2.6 (b)):

$$S = \frac{D - \vec{n} \cdot \vec{r}}{\vec{n} \cdot \vec{ct}} \quad (2.12)$$

where D was the distance from origin to location of face.

To avoid mistakenly picking up the wrong intersection of photon with an extension of the wrong face, the intersection with smallest value of S (or S_{\min}) was temporarily saved (Figure 2.7). This S_{\min} determined what face that photon would go to, and it was added to the cumulative path length such that the total path length was increased.

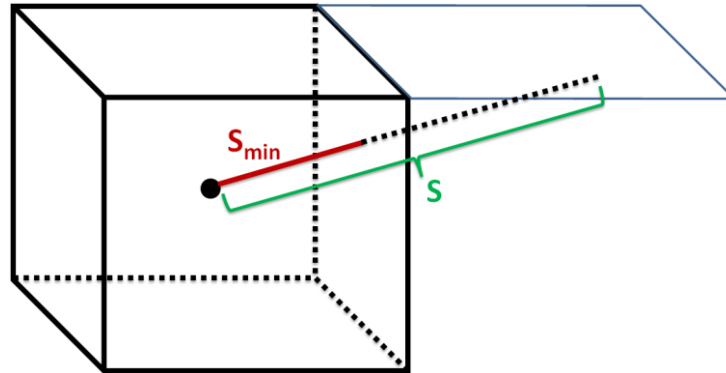


Figure 2.7: Illustration of definition of S_{\min} . For one sampled direction, the photon moved toward one of crystal surfaces. Only the smaller path length (red S_{\min}) rather than the larger value of path length (green S) which corresponds to incorrect intersection point on extension of top face was used.

2.2.4 Photon Propagation

Once direction and destination information (what face) was known, the photon would move toward that face and the integral path length of the photon history was updated. During the path to that face the photon could be experiencing scatterings and absorptions, where the former would reduce the photon weight and the later would give a new direction to that photon. Thus, scattering and absorption within the crystal was modeled in this step since the direction and weight of photon might change due to scattering and absorption. Because of the low energy of optical photons, the type of scattering would be coherent such as Rayleigh. Scattering and absorption within the crystal was modeled according to their respective interaction lengths. The scattering & absorption lengths were constrained through the following relationship [Karp *et al.* 2008]:

$$\frac{1}{L_t} = \frac{1}{L_s} + \frac{1}{L_a} \quad (2.13)$$

where L_t was the total attenuation/interaction length, L_s was the scattering length, and L_a was the absorption length. Referring to [Moisan *et al.* 1996, van der Laan *et al.* 2010], the L_t was assumed to be equal to L_s (i.e. 138 mm) at LSO peak emission wavelength (i.e. 420 nm). The scattering & absorption lengths are wavelength dependent and are acquired from transmission spectrum by optical measurements.

The probability of occurrence of interaction followed an exponential manner which is similar to the Beer-Lambert law for attenuation. Hence total interaction length, l_t , was randomly sampled with the following expression:

$$L_i = -L_t \cdot \ln(xr) \quad (2.14)$$

L_i was then compared in simulation with path length, S , which had been previously calculated. If L_i was smaller than S , then photon would interact with crystal in a manner of being absorbed or deviating away from previous direction. Otherwise the photon would keep propagating towards the predetermined face. For deciding the type of interactions, a single scattering albedo, α , was defined as the fraction of interactions being scatters:

$$\alpha = \frac{\mu_s}{\mu_s + \mu_a} \quad (2.15)$$

where μ_s was the scattering coefficient (inverse of scattering length) and μ_a was the absorption coefficient (inverse of absorption length). A random number was generated and the albedo was compared with this random number. If the albedo was larger than generated random number, the interaction was scatter; otherwise it was absorption. The photon weight was reduced by a factor of α after each interaction. In the case of scattering, the direction of the photon would change according to different angular probability distributions, which could be assumed as isotropic (Eq. 2.8) or Rayleigh ($1 + \cos^2 \theta_s$), where θ_s was the angle between incoming and scattered photons.

2.2.5 Reflection & Transmission

After propagation, the photon reaches the designated face, which could either be the bottom scoring face where the detector was located or the remaining five reflection faces. Generally, the physical and geometric models are two approaches to study reflection of surface. The former considers the characterization of electromagnetic waves of optics, whereas the latter analyses geometrical properties of a surface. The geometrical model is only applicable when dimensions of the surface roughness is larger compared to the wavelength of incident light, plus it is commonly the premier choice of modeling surface due to its simpler mathematical forms [Nayar *et al.* 1989].

2.2.5.1 Types of reflection

The simplest geometric model of a random roughness reflection surface is composed of two basic types of reflections: specular and diffusion (or Lambertian) reflections.

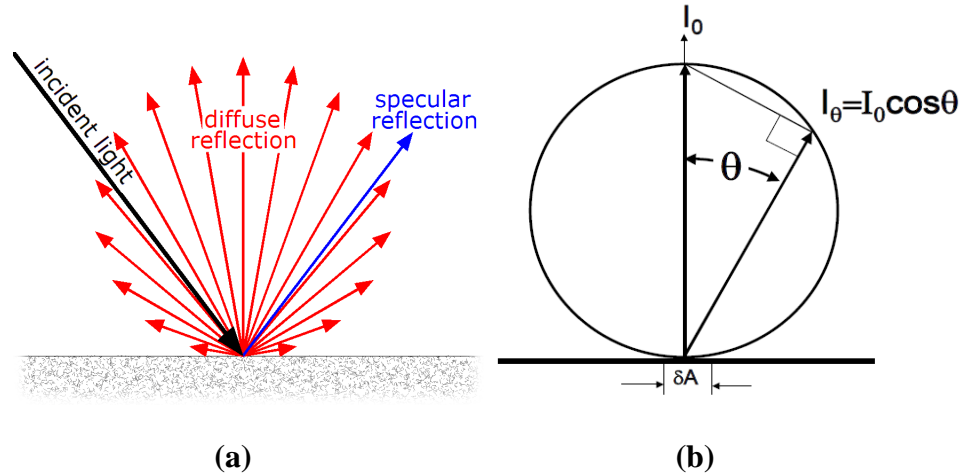


Figure 2.8: (a) A random surface consists of both specular and diffuse reflections. (b) Cosine distribution of diffusion reflection (with radiant intensity instead of radiance). [Yuming 2012].

The specular reflection is a mirror-like reflection of incident light on the reflection surface. The incident angle of incoming light is equal to that of the outgoing reflected light (Figure 2.9).

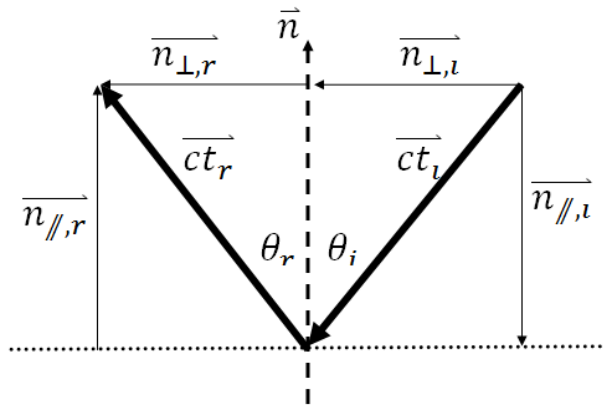


Figure 2.9: Schematic demonstration of dot-product expression for specular reflection.

The mathematical expression of the relationship between directions of reflected photons, \vec{ct} , and directions of incidence photons, \vec{ct}_i , was:

$$\vec{ct}_r = \vec{ct} - 2(\vec{n} \cdot \vec{ct})\vec{n} \quad (2.16)$$

where \vec{n} , was the normal vector of reflection surface. All directions of light were expressed in terms of vectors instead of trigonometric equations due to the lack of inverse trigonometric library of Free Pascal, and the speed of simulation was increased by doing this since the calculation of trigonometric equations takes longer time than that for vectors. Therefore all the trigonometric equations were mathematically replaced in forms of dot-product.

The properties of diffuse reflection are similar to those of specular reflection except that the angle between direction of reflected light and surface normal is not identical to that of incoming light as is the situation in specular reflection. Instead, the direction of reflected light (or radiant intensity) follows a cosine distribution (Lambertian distribution). A perfect diffuse reflection surface appears equally bright (radiance) from all directions. The mechanisms that cause Lambertian reflection are multiple external reflections and/or internal scattering. In the former situation (Figure 2.10 (a)), a diffusion surface is composed of many randomly oriented micro-facets on a microscopic scale. Light rays incident on this surface are reflected multiple times by these micro-facets before they return back to free space. In the internal scattering situation (Figure 2.10 (b)), light rays penetrate into a diffusion surface and scatter from microscopic subsurface inhomogeneities. Instead of penetrate through the whole surface as refraction, some part of light rays are reflected back to original free space.

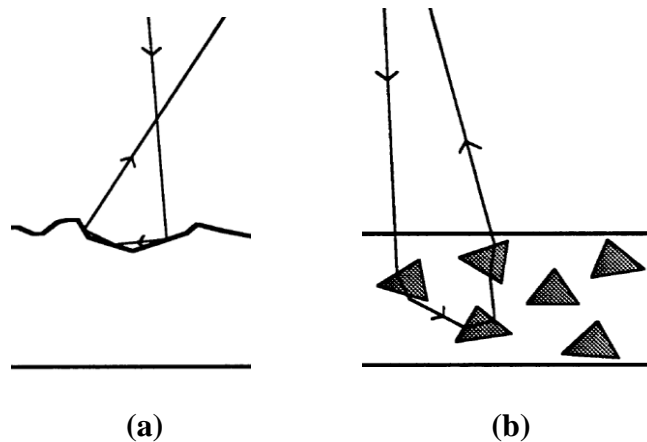


Figure 2.10: Illustration of two mechanisms of Lambertian reflection: (a) multiple reflections (b) internal scattering [Nayar *et al.* 1989].

Similar to DETECT, the rough surface was assumed to consist of irregular micro-facets following Lambertian cosine distribution with the following probability density functions:

$$\begin{cases} P(\theta) = 2 \sin \theta \cos \theta \\ P(\varphi) = \frac{1}{2\pi} \end{cases} \quad (2.17)$$

where φ was the azimuth angle, and θ was the polar angle. Instead of an inverse function method, the rejection method was used to simulate the cosine distribution. Figure 2.11 shows the linear relationship between Lambertian cosine distribution and a random number. First the expression of $\cos\theta$ was directly sampled by a generated random number (i.e. $\cos\theta = xr$, or the linear line in Figure 2.11). Therefore the green lower region in Figure 2.11 represents the sampled cosine distribution. Another new random number was then generated to compare with the linear line. If this number falls in the lower green region (the blue star), i.e. within cosine distribution region, the criterion was fulfilled; otherwise, if this number falls in the upper white region (the red star), then this random number was flipped back to the cosine region (the blue star) by " $\cos\theta = 1 - \cos\theta$ " instead of re-sampling another random number. This is possible since both regions have the same probability.

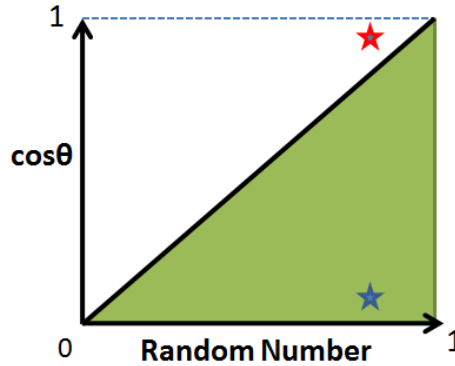


Figure 2.11: The rejection method of sampling lambertian cosine distribution.

In addition to reflections, incident photons could penetrate through the surface. The probability of occurrence of reflection is called reflection coefficient and is specified by the Fresnel's law:

$$R = \frac{R_s + R_p}{2} \quad (2.18)$$

where

$$R_s = \left(\frac{n_1 \cos\theta_i - n_2 \cos\theta_t}{n_1 \cos\theta_i + n_2 \cos\theta_t} \right)^2 \quad (2.19)$$

and

$$R_p = \left(\frac{n_1 \cos \theta_t - n_2 \cos \theta_i}{n_1 \cos \theta_t + n_2 \cos \theta_i} \right)^2 \quad (2.20)$$

where θ_i and θ_t are the incident and refracted angles, respectively; n_1 and n_2 are the index of refraction of incidence and refraction medium, respectively. And θ_i and θ_t are related by Snell's Law:

$$\frac{\sin \theta_i}{\sin \theta_t} = \frac{n_2}{n_1} \quad (2.21)$$

In simulation, the mathematical expression of relationship between direction of refracted photon and incidence photon was:

$$\vec{ct}_t = - \left[\sqrt{1 - \left(\frac{n_1}{n_2} \right)^2 (1 - (\vec{ct}_i \cdot \vec{n})^2)} \right] \vec{n} + \frac{n_2}{n_1} (\vec{ct}_i - (\vec{ct}_i \cdot \vec{n}) \vec{n}) \quad (2.22)$$

where \vec{n} was the normal vector of the surface (or micro-facet), \vec{ct}_i , \vec{ct}_t , were the directional cosine of incident and transmitted (refraction) photon, respectively as shown in Figure 2.12.

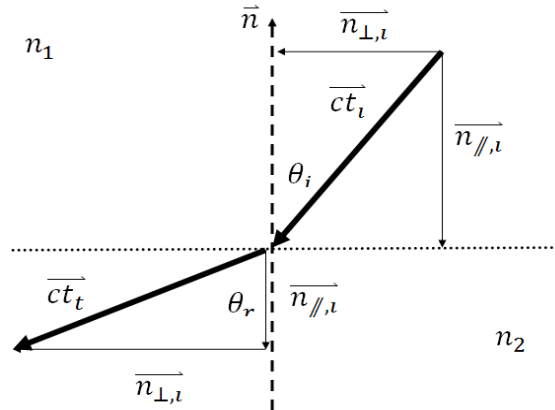


Figure 2.12: Schematic demonstration of dot-product expression for refraction.

As shown in Figure 2.6 (a), the normal vector of the surface was assumed to be pointing from crystal surface to reflector, thus Eq. 2.22 indicates that the incident photon was intending to transmit back to the crystal. For the case of incident photo transmitting from crystal to reflector (Figure 2.6(c)), the negative sign in front of square root in Eq. 2.22 would be positive.

2.2.5.2 Four combinations of surface-reflector

DETECT2000 offers four options: METAL, PAINT, POLISH or GROUND. In the METAL model, smooth (polished) surface is assumed with specular reflector as reflection coating. In PAINT model, the surface is still smooth but covered with Lambertian reflector instead. However, no transmission is considered in these two models. POLISH and GROUND models are more advanced since transmission of photons is involved and reflectors may or may not be in contact with surface in these two models.

In our simulation, optical behaviour of each reflection face was specified by four combinations of different surface treatments and types of reflectors according to specular and diffusion reflections. The terminologies of four options in DETECT2000 were used and revised. The METAL and PAINT in our simulation represented specular and Lambertian reflectors respectively. For surface treatment, POLISH represented smooth surface with specular reflection behaviour as its name implied. And GROUND represented rough surface that consists of many local micro-facet following Lambertian distribution. Therefore, the surface-reflector combinations were grouped in four options as listed in Table 2.2.

Table 2.2: Definition of surface-reflector combinations.

Model	Surface Treatment	Reflectors
Polish-Metal	Specular	Specular
Polish-Paint	Specular	Lambertian
Ground-Metal	Lambertian	Specular
Ground-Paint	Lambertian	Lambertian

Polish-Metal & Polish-Paint

Figure 2.13 demonstrates both Polish-Metal and Polish-Paint models. The crystal was assumed to be air-coupled (index of refraction is 1) with reflectors. It would be just a simple change of index of refraction if reflectors were glued on crystal surfaces. The gap between a crystal surface and its reflector is neglected due to its negligible value. The incident photons on crystal surface were tested with a reflection coefficient calculated from Fresnel's law based on incident angle. If a generated random number was less than reflection coefficient, then the incident photons, \vec{ct} , would reflect back into crystal, \vec{ct}_r according to specular equation (Eq. 2.16). Otherwise the incident photons would transmit through crystal surface, \vec{ct}_t according to refraction equation (Eq. 2.22) and incident on the bottom reflector which could either be specular (Metal) or Lambertian (Paint). Then those photons would bounce back from the reflector with reduced photon weights according to

reflection coefficients of that reflector, and eventually the photons would penetrate the crystal surface again and return back to the crystal medium. In Polish-Paint model, if photon failed to cross the surface back into the crystal, a new direction of reflected photon from reflector would be selected according to Lambertian cosine distribution until it successfully returns to crystal. The major difference between these two models was type of reflection on reflector leading to different directions of final reflected photons on surface-reflector face, \vec{ct}' . Note that the direction of \vec{ct}' was identical to that of \vec{ct} in the Polish-Metal model.

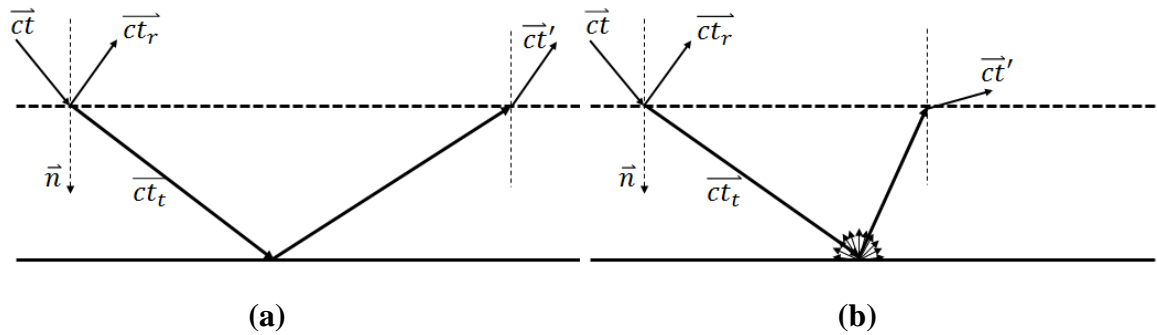
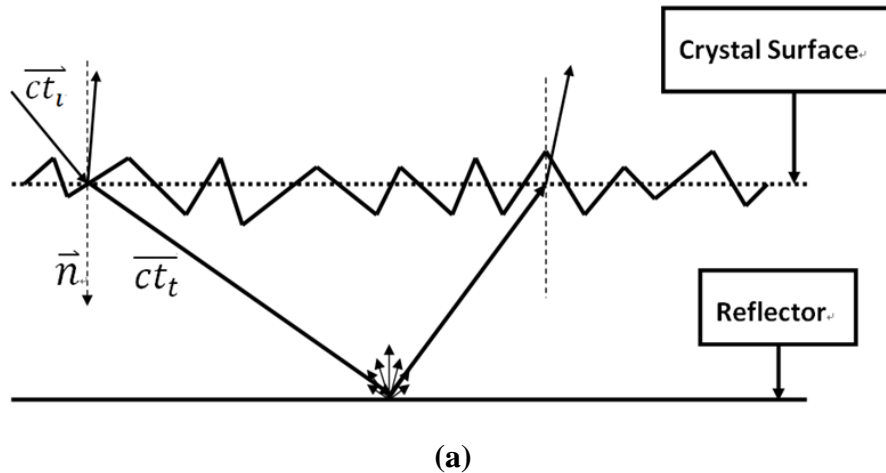


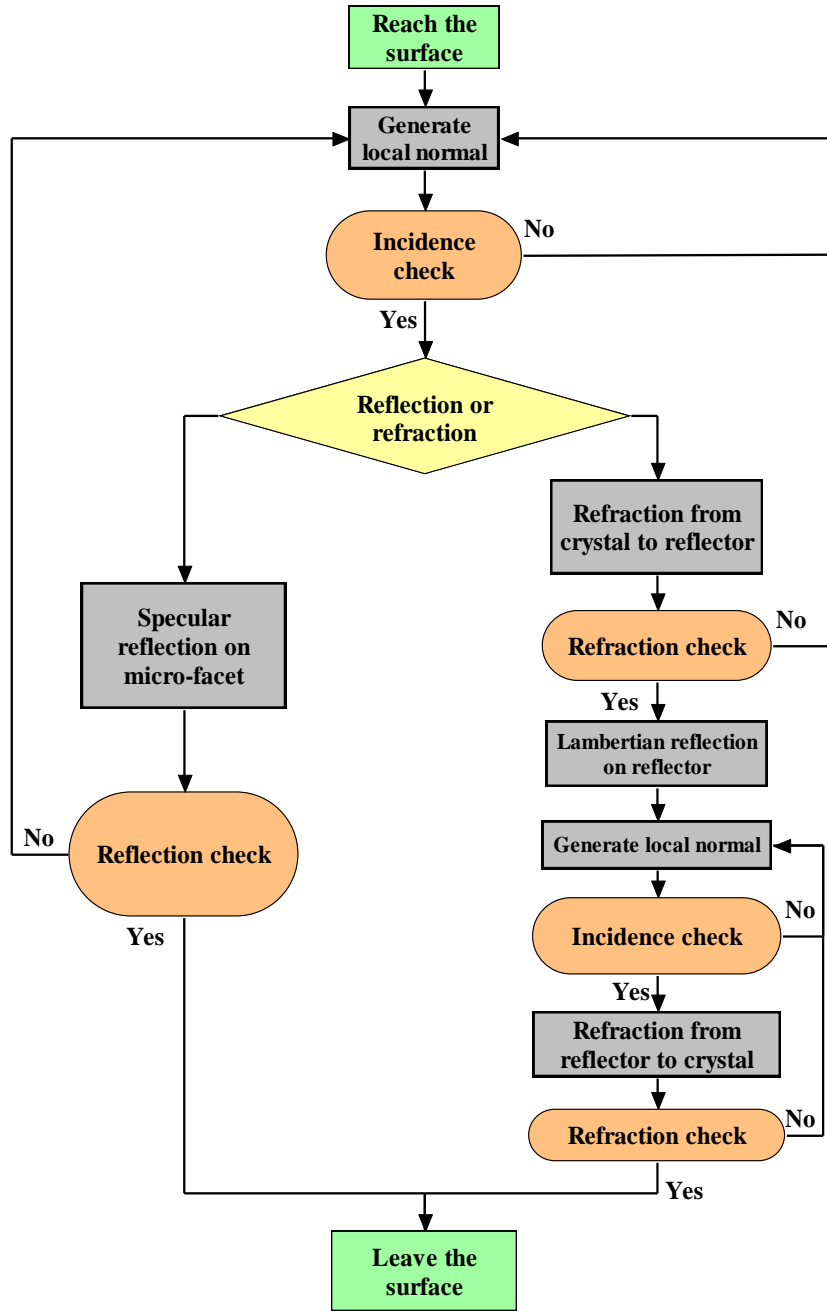
Figure 2.13: (a) Polish-Metal model; (b) Polish-Paint model. \vec{n} is the normal vector of the crystal surface. The bottom solid line and top dashed line represent reflector and crystal surface, respectively.

Ground-Metal & Ground-Paint

Figure 2.14 (a) schematically demonstrates Ground-Paint models. Similar to the above two Polish surface models, the only difference between Ground-Metal and Ground-Paint is the type of reflection on reflector, therefore only Ground-Paint is shown. Ground surface models are more complex than Polish surface models. In addition, the flow chart of simulating photon propagation in Ground-Paint model is shown in Figure 2.14 (b).



(a)



(b)

Figure 2.14: (a) The geometry and (b) flow chart of simulating “Ground-Paint” model. The bottom solid line and top dashed line in (a) represent reflector and crystal surface, respectively.

Instead of a smooth mirror-like surface as in Polish surface, the crystal surface is roughened in PAINT models with many micro-facets that have their own local normal vectors following Lambertian cosine distribution (Figure 2.15).

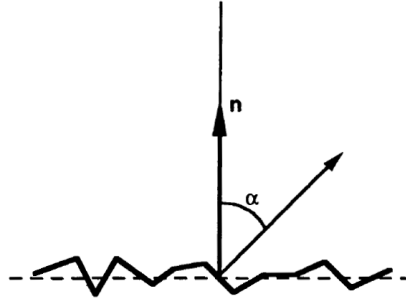


Figure 2.15: α , angle between a given micro-facet and the mean surface follows a Lambertian distribution for GROUND, or 0 for POLISH. Normal vectors of local micro-facet (local normal) were generated by Lambertian sampling the angle, α , between the average surface normal (from its plane equation) and local normal [Nayar *et al.* 1989].

A decision was made for the photon to either refract toward the reflector or specularly reflect on the micro-facet (including total internal reflection situation of refraction) back to the crystal with a random generated local normal by checking the reflection coefficient based on Fresnel's equation. If a generated random number was less than the reflection coefficient, then the incident photons, \overrightarrow{ct}_i , would be reflected back to crystal on that micro-facet (\overrightarrow{ct}_r in Figure 2.14 (a)); otherwise the incident photons would transmit through crystal surface (\overrightarrow{ct}_t in Figure 2.14 (a)) and be incident on the reflector which could either be specular (Metal) or Lambertian (Paint). Then those photons would be bounced back from reflector with dropped photon weights due to the reflection coefficients of the reflector in the same manner as in the Polish models. Finally, the photons penetrated a generated micro-facet on crystal surface again and returned back to crystal medium. Similar to Polish-Ground model, if a photon failed to cross the surface back into the crystal, a new direction of micro-facet rather than that of reflected photons from reflector was selected according to Lambertian cosine distribution until it successfully returns to crystal.

In addition, there were several new features for Ground surface models in order to prevent unrealistic situations. Figure 2.16 (a) shows the ideal realistic case of incident, reflected and refracted light on micro-facet. However, it was not always correct with certain local normal vectors of a micro-facet. The red solid line in Figure 2.16 (b) shows unrealistic incident light which comes from the wrong side of the micro-facet. The correct direction, \overrightarrow{ct} , is also shown in Figure 2.16 (b) with a black solid line. Therefore, an

incident angle check was set before photons cross the crystal surface (Figure 2.14 (b)). If the dot-product of incident light direction with local normal was less than zero, a new local normal was randomly selected until this dot-product was greater than zero. With the same test method, check points of reflected (and refracted) lights were set after photons reflect from (and refract through) micro-facets on crystal (Figure 2.16 (c) and (d), respectively).

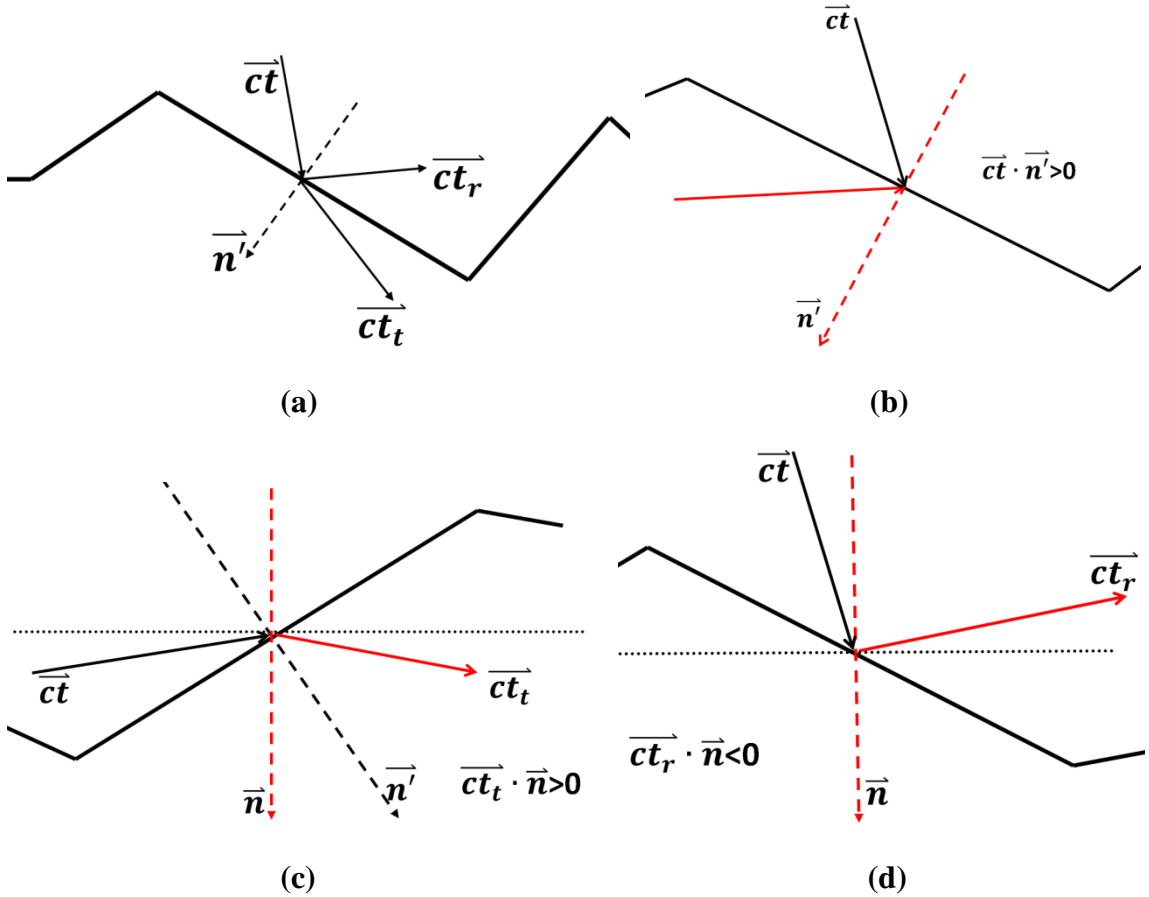


Figure 2.16: The (a) ideal realistic situations of direction of incident, reflected, and refracted light on micro-facet of crystal surface; (b) incident check with realistic condition of $\vec{ct}_i \cdot \vec{n}' > 0$; (c) reflected check with realistic condition of $\vec{ct}_t \cdot \vec{n} > 0$; and (d) refracted check with realistic condition of $\vec{ct}_r \cdot \vec{n} < 0$.

In conclusion, both specular and Lambertian reflectances were modeled in reflection & transmission section, and the photon weight was adjusted by the reflectance probability appropriate for the reflectance type. The photon history was continued by looping back to the trace photon to a crystal face (Figure 2.4).

2.2.6 Photon Termination

2.2.6.1 Photon Scoring

Despite the five reflection faces, when photons hit the detector face, the results in the form of total cumulative path length, S_{total} , were scored in different bins corresponding to magnitude of S_{total} . This means one count was added into the bin number that corresponds to the specific S_{total} . However, the one count was multiplied by the final remaining photon weight, wt , rather than a real one unit count since the weight of detected photon had dropped due to interactions such as transmission and absorption. Eventually the final simulation results were distributions (or histograms) of S_{total} and this integral path length of each photon's trajectory determined the propagation time of each photon within crystals, which was then used to generate time-resolved light output. Therefore, the simulation results were in fact the distribution of the integral path lengths (or propagation time) of all generated optical photons. All of the simulation results were convolved with a normalized intrinsic timing resolution function for simulating photon emission times due to the complicated luminescence process [Shao 2007]:

$$f(t) = \left(\frac{\tau_d + \tau_r}{\tau_d^2} \right) \cdot e^{-\frac{t}{\tau_d}} \cdot (1 - e^{-\frac{t}{\tau_r}}) \quad (2.23)$$

where τ_d was decay time constant (e.g. 0.5 ns for LYSO crystal), τ_r was rise time constant (e.g. 40 ns for LYSO crystal) (Table 1.2).

2.2.6.2 Other Photon Terminations

In fact, there were a wide variety of fates of individually generated photons as they propagated through the scintillation crystal not only by scoring but also in many other termination conditions such as the path length being too long (S_{max}) or the photon weight being too small (wt_{min}). If there were too many numbers of scatterings or reflections, the photon might be terminated by *Russian Roulette*, which was a variance reduction technique used to avoid tracking low weight photons endlessly. Once the total number of reflections was over an anticipated threshold ($n_{\text{ref}_{\text{max}}}$), a random number was generated and compared with a pre-set constant called *Roulette parameter*, R . If the random number was smaller than R then the photon was terminated, otherwise the weight of this photon was increased by multiplying a factor of $\frac{1}{R}$. In our simulation, R was 0.25; S_{max} was 500 mm; wt_{min} was 10^{-6} ; and $n_{\text{ref}_{\text{max}}}$ was 1000.

2.3 Simulation Data Analysis

2.3.1 Preliminary Analytical Verification

In this section, the detailed geometric analysis of the preliminary simulation results of a $3 \times 3 \times 3 \text{ mm}^3$ crystal is presented. The preliminary result of a $3 \times 3 \times 3 \text{ mm}^3$ crystal is shown in Figure 2.17 in which all of the generated photons were launched isotropically from a single point at the geometric centre of this crystal (i.e. 1.5 mm from the bottom of crystal, where is the presumed location of photodetector). To enable further analysis, only specular reflection and no reflector, scattering & absorption were considered. Nevertheless, this would allow us to gain a good understanding about several fundamental processes of light transport inside crystals.

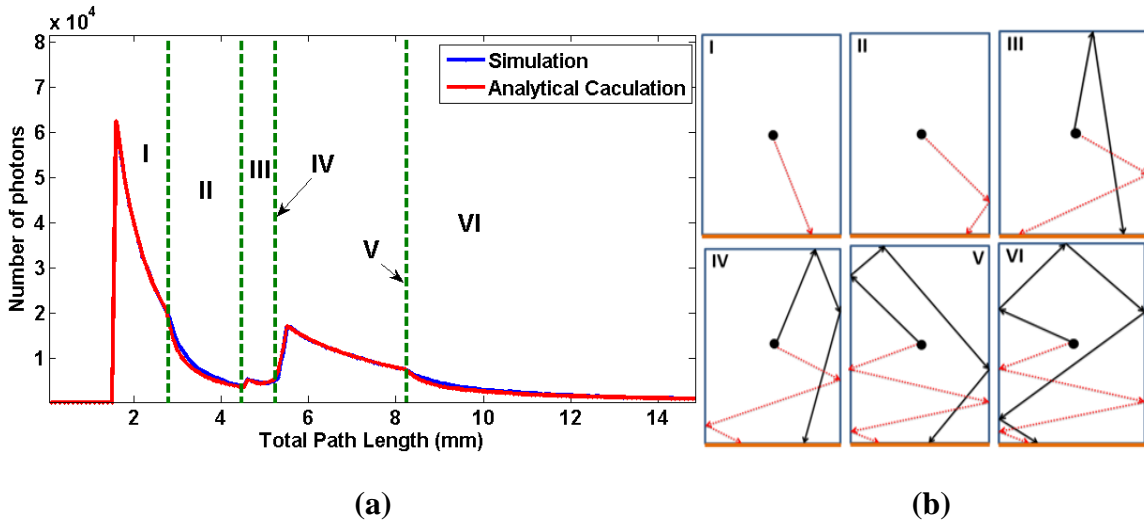


Figure 2.17: (a) The number of photons versus S_{total} . (b) Different regions of geometrical analysis for tracking each photon step by step with specular reflection.

Figure 2.17 (b) represents different possible scenarios of path length of each photon. Analytic validation was implemented merely based upon solid angle coverage (i.e., summing up all photons falling within a given scenario). Under these conditions the time-resolved light output could be calculated analytically from the geometry of the problem. The analytic solution was obtained by tracking the photon, geometrically through multiple reflections, and finding the solution separately in different time regions corresponding to different paths.

I: This is the region for photons launched directly downward without reflection from the side faces.

II: This is the region for photons launched downward with reflection from the side faces with photon weights dropped. For some other tested dimensions (or launched positions), total internal reflection occurs hence no photon weight is dropped.

III: This region includes two components: launched downward with reflection from the side faces (red), plus photons that originally are launched upward and bounced back from the top face (black); both components drop photon weights because of reflections.

IV & V: These are the total internal reflection regions which consist of the same two components as region III, but the upper component (black) is total internal reflection. Thus, only the lower component (red) drops photon weights due to the reflections.

VI: This last region is similar to region III but more numbers of reflections for both components.

The physical analysis in the aspect of reduction of photons due to both probability distribution and reflections (specular) on four side faces as well as top face are shown in the following subsections.

2.3.1.1 General probability distribution

The analysis commenced at evaluating probability distribution of direction of one photon for a specific total path length (i.e. S_{total}) without considering reflection.

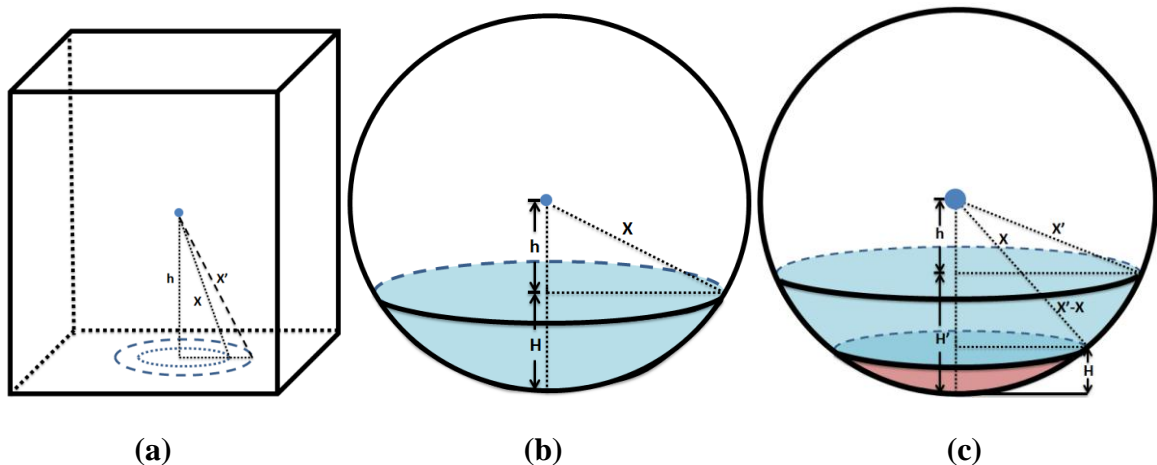


Figure 2.18: (a) Schematic demonstration of the first three S_{total} : h , X , and X' . (b) Bowl-area models of calculating probability distribution for S_{total} equals to X ; (c) for S_{total} equals to X' , the probability is associated with the red bottom bowl area.

Refer to Figure 2.18 (a), as assumed before, the photon is launched at mid-point of crystal, or h equals to 1.5 mm for a $3 \times 3 \times 3$ mm³ cubic crystal. Thus, h is the smallest S_{total} that indicates the situation of one photon is straightly shooting downward to center of bottom face of crystal. Then one full count is scored into the bin corresponding to this S_{total} since no reduction of photon weight due to reflection. For the next higher level bin, i.e. S_{total} (or X in Figure 2.18) equals to 1.6 mm, the circle on bottom of crystal is the scoring position of a photon having $S_{\text{total}}=1.6$ mm. And the probability or proportionality of detecting the number of photons within 1.5 to 1.6 bin with respect to all the possible S_{total} is calculated as the ratio of area of the bowl corresponding to this X (Figure 2.18 (b)) to the entire area of solid-angle sphere:

$$P_{1.6} = \frac{2\pi H X}{4\pi X^2} = \frac{H}{2X} = \frac{1.6-1.5}{2 \cdot 1.6} = \frac{1}{32} \quad (2.24)$$

Thus, for whatever the amount of isotropically launched photons (two million photons in our simulation), 1/32 of them are detected with final path length of 1.6 mm. And for the next bin, i.e. $S_{\text{total}}=1.7$ mm (X' in Figure 2.18 (a) (c)), the probability of detecting the number of photons within 1.6 to 1.7 bins is calculated as difference of areas of bowl with $X=1.7$ to the area of bowl with $X=1.6$ bins:

$$P_{1.7} = \frac{2\pi H' X' - 2\pi H X}{4\pi X'^2} = \frac{(1.7-1.5) \cdot 1.7 - (1.7-1.7 \frac{1.5}{1.6}) \cdot 1.7}{2 \cdot 1.7 \cdot 1.7} = \frac{(1.7-1.5) - (1 - \frac{1.5}{1.6}) \cdot 1.7}{2 \cdot 1.7} \quad (2.25)$$

Following the same manner, the probability of detecting the number of photons within the X^{th} to $(X+1)^{\text{th}}$ bins are mathematically described as:

$$P_X = \frac{2\pi X(X-h) - 2\pi X(X - X \frac{h}{X-0.1})}{4\pi X^2} = \frac{h(\frac{X}{X-0.1} - 1)}{2X} = \frac{h(\frac{S_{\text{total}}}{S_{\text{total}}-0.1} - 1)}{2S_{\text{total}}} \quad (2.26)$$

where again h is 1.5 mm for $3 \times 3 \times 3$ mm³ cubic crystal.

Note that this probability distribution of specific path length is applied for all of photons that are launched downward regardless of subsequent interactions such as reflections.

For the probability distribution of photons that are initially launched upward, the only difference is that the h is now 4.5 mm rather than 1.5 mm since the shortest distance of upward launched photons is 4.5 mm (Figure 2.19).

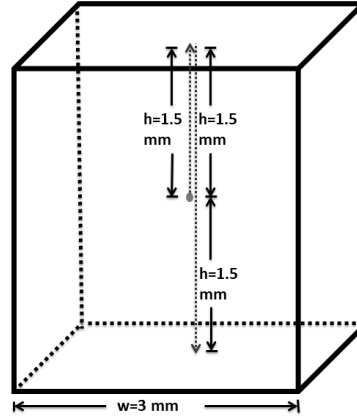


Figure 2.19: The distance of the first detected initially upward launched photon is $3h$ (4.5 mm).

Hence the probability distribution function is:

$$P'_X = \frac{3h\left(\frac{X}{X-0.1} - 1\right)}{2X} = \frac{3h\left(\frac{S_{total}}{S_{total}-0.1} - 1\right)}{2S_{total}} \quad (2.27)$$

2.3.1.2 Boundary conditions of number of reflections on side faces

For studying reduction of photons due to reflections, those photons that are initially launched downward (lower part of crystal) are first investigated. Refer to Figure 2.20 (a), the S_{total} (or X) gradually increases from a region of straightly shooting toward the bottom face to a region of interacting with four side faces where there is occurrence of reflections. As shown in Figure 2.20 (a), two boundary conditions of S_{total} for deciding if photons were interacting with side reflection faces can be simply determined. The shorter boundary S_{total} (blue dashed line in Figure 2.20 (a)) is the distance from launch point to midpoint of the edge of side faces and is calculated as $\sqrt{h^2 + a^2} = \sqrt{1.5^2 + 1.5^2} = 2.12$ mm. The longer boundary S_{total} (green dashed line in Figure 2.20 (a)) is the distance from launch point to the bottom corner point and is calculated as $\sqrt{(a^2 + a^2) + h^2} = \sqrt{(1.5^2 + 1.5^2) + 1.5^2} = 2.598$ mm.

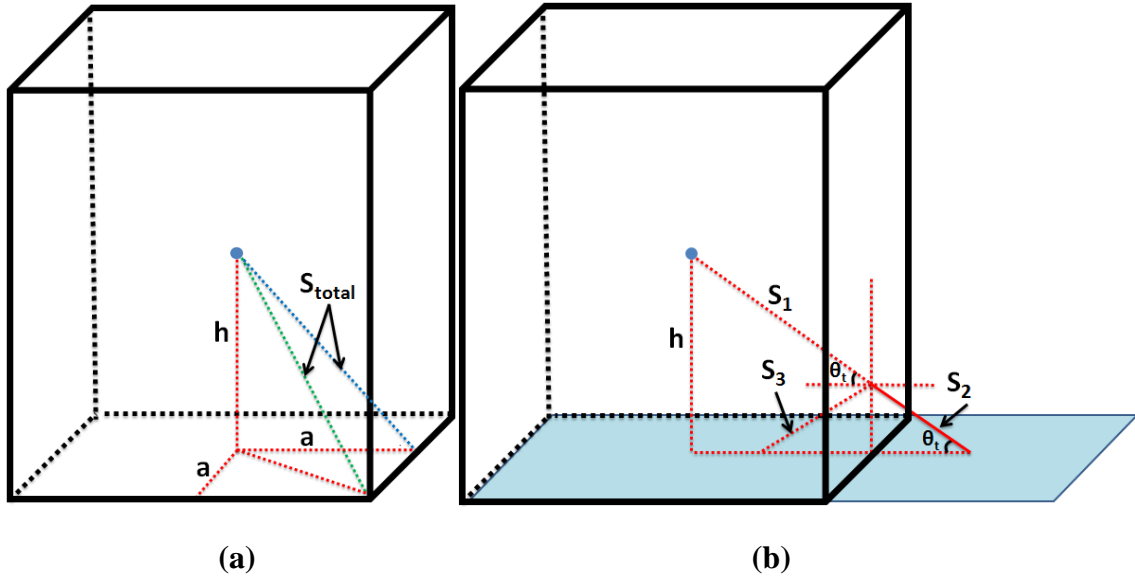


Figure 2.20: (a) Two boundary conditions of downward launched photons without interaction with any of the four side faces. The blue and green dashed lines represent the shorter and longer path lengths of these boundaries, respectively; (b) the boundary condition of total internal reflection on four side faces.

However, the type of reflections, i.e. either regular reflection (Fresnel's law) or total internal reflection, has to be determined first. In simulation, the index of refraction is 1.83 so that the critical angle, θ_t , is determined from $\sin\theta_t = \frac{n_{air}}{n_{crystal}} = \frac{1}{1.83}$, or $\theta_t = \arcsin\left(\frac{n_{air}}{n_{crystal}}\right) = \arcsin\left(\frac{1}{1.83}\right) = 33.12^\circ$. In Figure 2.20 (b), assuming a situation of total internal reflection occurs at $S_{total}=S_1+S_3$, due to the geometric symmetry property (i.e. the reflection face is analogue to a mirror), S_2 equals to S_3 so that $S_{total}=S_1+S_2$. Note that this symmetric property will be frequently used later. Last of all, S_{total} at total internal reflection is calculated as $S_{totaltir} = \frac{h}{\sin\theta_t} = 1.5 \times 1.83 = 2.745$ mm. Therefore, the type of reflection is total internal reflection as the incident angle gradually increases to critical angle, thereafter the type of reflection switches to regular reflection where Fresnel's theory is involved and the number of photons (or photon weight) will be dropped on the four side faces. Note that $S_{totaltir}$ is also larger than the predetermined two reflection boundary S_{total} (2.12 mm, and 2.598 mm) thus there is no reduction of photon owing to reflection in the range of S_{total} smaller than 2.745 mm. As discussed before, the number of photons (or photon weight) would drop if a reflection occurs since some of the incident photons would be transmitted through reflection faces (again, assuming no reflector was used). And if the incident angle becomes smaller than the critical angle, more reflections will occur while S_{total} keeps increasing. Thus, the total number of reflections is desired since it determines the remaining number of photons (or photon weight).

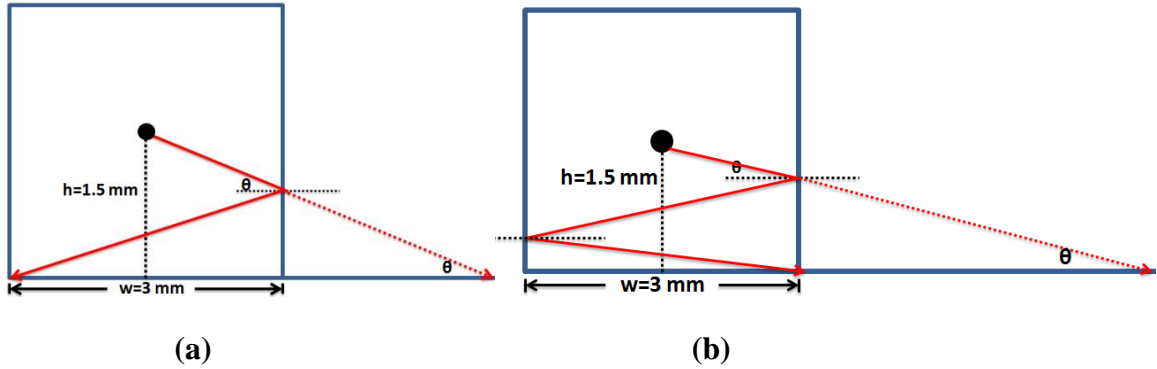


Figure 2.21: Two dimensional schemes of boundary conditions of (a) one reflection, and (b) two reflections on one of side faces.

Figure 2.21 demonstrates two examples of boundary conditions for different number of reflections. Figure 2.21 (a) represents the upper limit condition of S_{total} for only one reflection, and it can be simply determined from the following two equations from geometric analysis:

$$\begin{cases} S_{\text{totalmax1}} = \frac{w}{\cos \theta} \cdot \left(\frac{1}{2} + 1\right) \\ \sin \theta = \frac{h}{S_{\text{totalmax1}}} \end{cases} \quad (2.28)$$

Thus, $S_{\text{totalmax1}}$ is 4.743 mm. This means only one reflection would happen if S_{total} is less than 4.743 mm. And the upper limit condition of S_{total} for two reflections can be similarly determined as follows:

$$\begin{cases} S_{\text{totalmax2}} = \frac{w}{\cos \theta} \cdot \left(\frac{1}{2} + 2\right) \\ \sin \theta = \frac{h}{S_{\text{totalmax2}}} \end{cases} \quad (2.29)$$

So, $S_{\text{totalmax2}}$ is 7.648 mm. Following the same manner, for n number of reflections, the upper limit condition, i.e. $S_{\text{totalmaxn}}$ is calculated as:

$$\begin{cases} S_{\text{totalmax}n} = \frac{w}{\cos \theta} \cdot \left(\frac{1}{2} + n\right) \\ \sin \theta = \frac{h}{S_{\text{totalmax}n}} \end{cases} \quad (2.30)$$

which is the general equation of determining these boundary conditions. Therefore, for multiple reflections, the calculated limiting conditions on downward launched photons from a mid-point (or lower region of crystal) in a $3 \times 3 \times 3 \text{ mm}^3$ crystal are listed in Table 2.3.

Table 2.3: Boundary conditions of total path length for a number of reflections while photons are initially launched downward from a mid-point in a $3 \times 3 \times 3 \text{ mm}^3$ LYSO crystal.

No. of reflections	S_{totalmax} (mm)
1	4.743
2	7.648
3	10.606
4	13.583
5	16.568
6	19.557

A photon that was initially launched straight upward will hit the center point of top face and be reflected back at 180 degrees into the crystal with reduced weight based on Fresnel's law. Then it will propagate for a while and finally hit the center point of the bottom scoring face. The total propagation distance is $3h$, or 4.5 mm in this cubic case. This is the shortest distance of photons which are initially launched upward and are then detected.

The situations of boundary conditions for the upper part of crystal are relatively simpler than those for lower part. Since the top face corresponds to specular reflections, the critical angle of total internal reflection has to be considered. Figure 2.22 (a) shows the boundary condition of total internal reflection: regular reflections occur within the blue circle, whereas total internal reflections happen outside of this blue circle (i.e. the green region). For the case of total internal reflection on the top face, refer to Figure 2.22 (b), the reflection on side face is also total internal reflection since the incident angle on side face is $90-\theta$, where θ is always smaller than 45° which is the situation of an incident photon that moves toward the upper corners of a crystal cube. The expression of total

propagation distance at the starting point of total internal reflection in the upper part of the crystal is simply determined:

$$S_{\text{totalirstart}} = \frac{X + H}{\cos \theta} \quad (2.31)$$

While S_{total} keeps increasing, similar to that in lower part, the upward launched photons will first interact with side faces and reflect back toward top face and so on (Figure 2.22 (c)). This reflection status is still total internal reflection because the incident angle is larger than the critical angle until it meets another boundary condition, which is the end point of the total internal reflection situation.

$$S_{\text{totalirend}} = \frac{X + H}{\sin \theta} \quad (2.32)$$

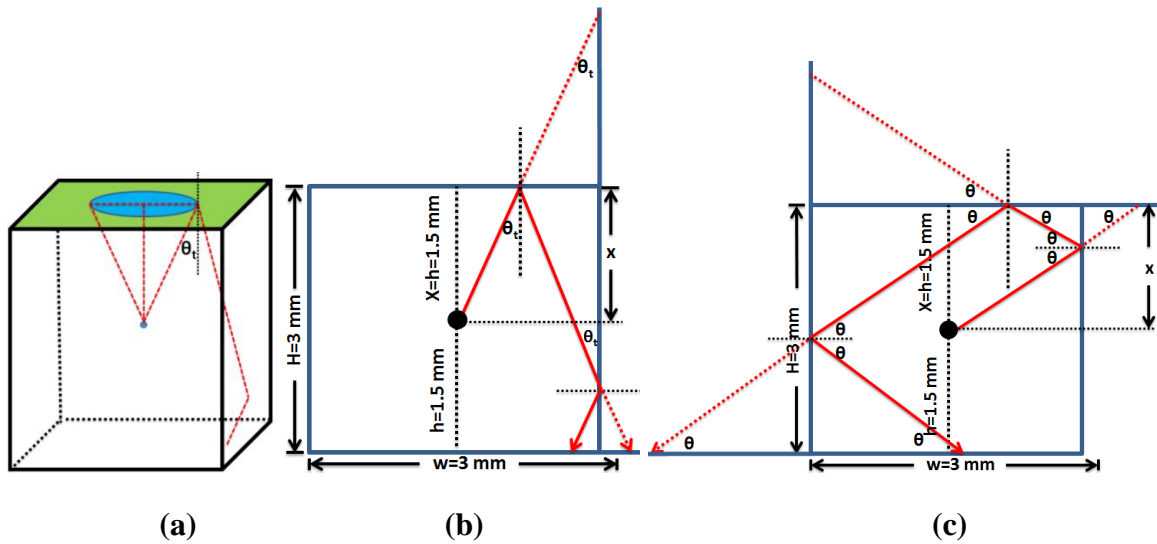


Figure 2.22: (a) The region of total internal reflection for initially upward launched photons (green area). All photons that interact within the blue circle area are Fresnel reflections rather than total internal reflections; (b) start of boundary conditions of total internal reflection on top face. It is associated with size of blue circle; (c) end of boundary conditions of total internal reflection on side faces for upward launched photons.

In this cubic case, $S_{\text{totalirstart}}$ is equal to 5.371 mm, and $S_{\text{totalirend}}$ is equal to 8.235 mm. This indicates that for those scored photons that have total propagation distance between 5.371 mm and 8.235 mm, part of them are from the total internal reflections in the upper part of the crystal, while the rest of them are from multiple regular reflections in the lower

part. Based on Table 2.3, 5.371 mm and 8.235 mm correspond to two and three reflections in the lower part, respectively.

Note that although the first interaction on the upper side face is not total internal reflection for region of S_{total} larger than 8.235 mm, the subsequent reflection on the top face (Figure 2.22 (c)) might be still total internal reflection since the incident angle is $90-\theta$, which could possibly be larger than the critical angle. Apparently, the next reflection (on the left side face in Figure 2.22 (c)) is not total internal reflection since the incident angle of this reflection is the same as that of the first reflection (on the right side face in Figure 2.22 (c)). Thus, only two regular reflections, rather than three, contribute to reduction of photon weights.

2.3.1.3 Taper analysis of fraction of total internal reflections on side faces

These boundary conditions of total internal reflections and of number of reflections are 2D estimations which describe the starting points (or ending points) of total internal reflections and the shortest path length for the next higher number of reflections. In reality, the predictions of total internal reflections have to be associated with a three-dimensional geometric analysis. For the purpose of this thesis these will be referred as *taper predictions*.

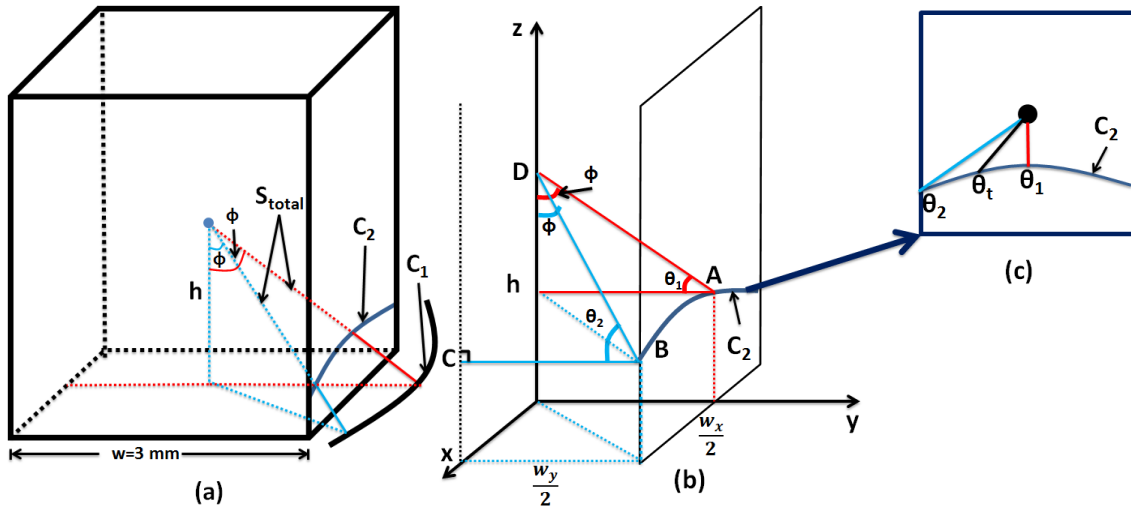


Figure 2.23: Schemes of 3D taper predictions of partial total internal reflections on side faces. The red lines are 2D total path lengths and correspond to boundary condition calculations in Figure 2.20 and Figure 2.21.

Two total path lengths, or S_{total} , with the same length are shown in Figure 2.23 (a). Note that the red S_{total} represents the two-dimensional condition of total internal reflection

(Figure 2.23 (b)) such that the solid line (S_2 in Figure 2.20 (b)) is the image of the real reflected path length (S_3 in Figure 2.20 (b)). Thus, one could imagine and draw a taper (or cone) with vertex at the launched point, height of h , and side length of S_{total} around the cubic crystal. C_1 in Figure 2.23 (a) is partial curve of a base circle of this taper. C_2 is projection of this taper on side face of crystal. Although all the paths that have the same S_{total} (or the same side length of cone) share the same polar angle, φ , the incident angles of these paths are different from one another. This is shown in Figure 2.23 (b). The blue path is defined as the S_{total} that is located at the intersection of C_2 and the edge of the side face, whereas the red path is defined as the S_{total} that is located at the midpoint of C_2 . Although the blue path has the same path length (or polar angle, φ which is the angle between the direction of S_{total} and Z-axis) as that of red path length, the incident angle of the blue path (θ_2) is different to, or more precisely larger than the incident angle of the red path (θ_1). Thus, even though the boundary condition of incident angle θ_1 is smaller than the critical angle, incident angles of other photons with the same S_{total} (or the same φ) are still larger than the critical angle leading to total internal reflections for these photons. As shown in Figure 2.23 (c), the reflections would be total internal reflections between θ_t and θ_2 , hence a fraction of total internal reflection for the same S_{total} is defined as follows:

$$\text{tirpercent} = \frac{\theta_2 - \theta_t}{\theta_2 - \theta_1} \quad (2.33)$$

Note that different reflection coefficients would be expected from θ_1 to θ_t due to the different incident angles. Instead, for the reason of simplicity, a condition of constant reflection coefficients between these two incident angles is presumed.

The sine function of an incident angle θ_1 has simply determined previously as $\sin\theta_1 = \frac{h}{S_{total}}$ so that $\theta_1 = \arcsin(\frac{h}{S_{total}})$. The critical angle θ_t was calculated to be 33.12° . For deriving the expression of θ_2 , coordinates of two points (A and D in Figure 2.23 (b)) are first determined:

$$\text{Point A} = \begin{cases} x_A = \frac{w_x}{2} \\ y_A = \frac{w_y}{2} \\ z_A = h - \frac{\sqrt{(\frac{w_x}{2})^2 + (\frac{w_y}{2})^2}}{\tan\varphi} \end{cases} = \begin{cases} x_A = 0 \\ y_A = 1.5 \\ z_A = 1.5 - \frac{\sqrt{(1.5)^2 + (1.5)^2}}{\tan\varphi} \end{cases} \quad (2.34)$$

$$\text{Point D} = \begin{cases} x_D = 0 \\ y_D = 0 \\ z_D = h = 1.5 \end{cases} \quad (2.35)$$

since w_x and w_y are 3 mm and h is 1.5 mm. Therefore the cosine function of an incident angle θ_2 is determined according to geometrical analysis based on the calculation of distance between two points:

$$\cos\theta_2 = \frac{|AC|}{|AD|} = \frac{\frac{w_y}{2}}{\sqrt{\left(\frac{w_x}{2}-0\right)^2 + \left(\frac{w_y}{2}-0\right)^2 + \left(h - \frac{\sqrt{\left(\frac{w_x}{2}\right)^2 + \left(\frac{w_y}{2}\right)^2}}{\tan\varphi} - h\right)^2}} = \frac{1}{\sqrt{\left(\frac{w_x}{w_y}\right)^2 + 1}} \sin\varphi \quad (2.36)$$

where $\cos\varphi = \frac{h}{S_{total}} (= \frac{1.5}{S_{total}})$, therefore $\cos\theta_2 = \frac{1}{\sqrt{\left(\frac{w_x}{w_y}\right)^2 + 1}} \sqrt{1 - \left(\frac{h}{S_{total}}\right)^2}$ so that

$$\theta_2 = \arccos\left(\frac{1}{\sqrt{\left(\frac{w_x}{w_y}\right)^2 + 1}} \sqrt{1 - \left(\frac{h}{S_{total}}\right)^2}\right). \quad (2.37)$$

Therefore, the fraction of total internal reflection is:

$$\text{tirpercent} = \frac{\theta_2 - \theta_t}{\theta_2 - \theta_1} = \frac{\arccos\left(\frac{1}{\sqrt{\left(\frac{w_x}{w_y}\right)^2 + 1}} \sqrt{1 - \left(\frac{h}{S_{total}}\right)^2}\right) - \arcsin\left(\frac{n_{air}}{n_{crystal}}\right)}{\arccos\left(\frac{1}{\sqrt{\left(\frac{w_x}{w_y}\right)^2 + 1}} \sqrt{1 - \left(\frac{h}{S_{total}}\right)^2}\right) - \arcsin\left(\frac{h}{S_{total}}\right)} \quad (2.38)$$

In conclusion, for different S_{total} regions relating to reflections on side faces, the weight of total internal reflection (i.e. ‘‘tirpercent’’) can be determined. The basic mathematical models of physics at different situations and boundary conditions have been studied in this section.

Again, Figure 2.17 (a) demonstrates the number of photons versus S_{total} instead of total propagation time for both simulation and analytical calculations based on the above derived equations at different regions by using $3 \times 3 \times 3 \text{ mm}^3$ cubic crystal as an example. The reduction of photons is only due to the probability distribution in the lower part of the crystal. The boundary limit of S_{total} between region I and region II is 2.745 mm, which is the point where reflections on the side faces for the lower part of the crystal (II in Figure 2.17 (b)) are total internal reflections. Recall that the boundary limits of straightly

launched downward photons without interacting with side faces (“I” in Figure 2.17 (b)) are 2.12 mm and 2.598 mm, which are all less than 2.745 mm. These two boundary limits could all be larger than that of total internal reflections for other dimensions of crystal or other launched points which leads to a reduction of number of photons due to reflections between the new boundary limits. Thus, the mathematical expression of describing number of photons in region I is:

$$\text{Number of Photons} = N_0 P_x \quad (2.39)$$

where N_0 is the total number of initial launched photons (two million in simulation), h is 1.5 mm again, and P_x is from Eq. 2.26. Hence, the number of photons is a function of S_{total} .

For S_{total} larger than 2.745 mm, the reflections on the side faces in the lower part of the crystal are a combination of regular reflections with reflection coefficients based on Fresnel’s law and partial total internal reflections according to the taper prediction rather than completely total internal reflections. This elucidates the greater drop of number of photons in region II. Thus, the mathematical expression describing the number of photons in region II is:

$$\text{Number of Photons} = N_0 P_x [\text{tirpercent} + (1 - \text{tirpercent})R] \quad (2.40)$$

where R are the reflection coefficients from Eq. (2.18), “tirpercent” is from Eq. 2.38 which also applies to the remaining “tirpercent” in the following equations. R is a function of incident angle, which is always related to S_{total} as: $\sin\theta_i = \frac{h}{S_{\text{total}}}$.

The region III starts at where S_{total} is equal to 4.5 mm, which is the shortest distance for photons which are initially launched upward and then detected. Therefore the total number of photons after 4.5 mm consists of detected photons from both the lower and upper part of crystal. This is the reason for the small bump in region III. The upward launched photons interact within the circle that represents the area of non-total internal reflection (Figure 2.22 (a)) on the top face. The mathematical expression of number of photons in region III is:

$$\begin{aligned} \text{Number of Photons} &= \text{Number of Photons (upper)} + \text{Number of Photons (lower)} \\ &= N_0 P'_x R' + N_0 P_x [\text{tirpercent} + (1 - \text{tirpercent})R] \end{aligned} \quad (2.41)$$

where R' are the reflection coefficients for photons from the upper part and is always determined from Eq. 2.31. Note that the number of reflections on the lower side face is two for S_{total} larger than 4.743 mm (Table 2.3), however, only one reflection is assumed

for the region III. One source of difference between simulation and analytical calculation is believed to be the inaccuracy using the mathematical estimation of taper prediction.

The end point of region III is where S_{total} is equal to 5.371 mm, which is the start point of total internal reflection on the top face (IV in Figure 2.17 (b)). Thus, there is no reduction of number of photons due to reflections on the top face. This explains the relatively larger bump in region IV than that in region III. The mathematical expression of number of photons in region IV is:

$$\begin{aligned} \text{Number of Photons} &= \text{Number of Photons (upper)} + \text{Number of Photons (lower)} \\ &= N_0 P'_x + N_0 P_x \left[\text{tirpercent} + (1 - \text{tirpercent}) R^2 \right] \end{aligned} \quad (2.42)$$

Refer to Table 2.3, from 5.371 mm to 7.648 mm, two reflections occur on the lower side faces, and this explains the square of reflection coefficients, R in the above equation. From 7.648 mm to 8.235 mm (V in Figure 2.17 (b)), this number of reflections increase to three, thus it would be a power of three of reflection coefficients, R , in the remaining part of region IV. The effect of the difference between two and three reflections is not significant as shown in the results (no obvious reduction of number of photons in Figure 2.17 (a)).

The point where S_{total} is equal to 8.235 mm is the start point of the last region (VI in Figure 2.17 (b)), in which reflections on the upper side faces are regular reflections as well as partial total internal reflections from taper prediction rather than complete total internal reflections. The mathematical expression for the number of photons in region VI is similar to that in region III. The number of powers of reflection coefficients, R , is different based on S_{totalmax} in Table 2.3. However, the effect of the difference due to higher numbers of reflections is not significant. The number of detected photons from the analytical calculation in this region is generally lower than those from simulation. One source of this difference is because of the exclusion of the taper prediction for partial total internal reflections on upper side faces.

The agreement between analytical calculations and simulation results for photons launched at the mid-point of a $3 \times 3 \times 3 \text{ mm}^3$ cubic crystal verify our preliminary simulation results. Two other launched points (heights of 0.5 mm and 2.5 mm from the bottom scoring face) for this $3 \times 3 \times 3 \text{ mm}^3$ crystal (Figure 2.24 (a) (c)), as well as launch points at the middle of other dimensions were also tested (Figure 2.24 (d)). In conclusion, all of the results between simulation and analytical calculations for different launched points and dimensions indicate the general structure (i.e. without scattering and more complicated reflections on reflection faces) of the simulation is functioning well.

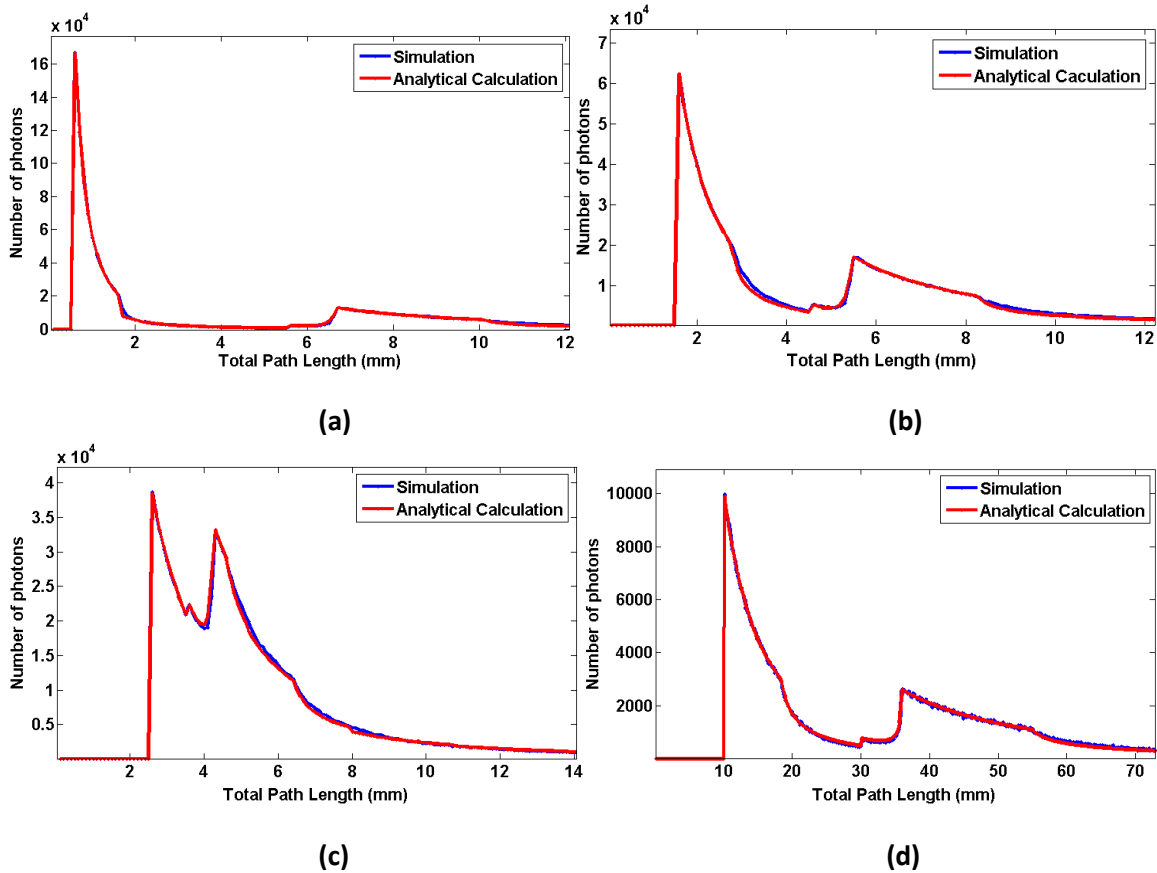


Figure 2.24: Simulation timing results vs. analytical calculations. The photons are launched at: (a) 0.5 mm (b) 1.5 mm (c) 2.5 mm from the bottom scoring face for the $3 \times 3 \times 3 \text{ mm}^3$ crystal; and (d) mid-point (10 mm) from the scoring face for the $3 \times 3 \times 20 \text{ mm}^3$ crystal.

2.3.2 Verification of Exponential Distribution of Attenuated 511 keV Photons

As 511 keV annihilation photons attenuate within LSO crystals following an exponential distribution, the light propagating as a function of various interaction heights was investigated. The single crystal ($3 \times 3 \times 20 \text{ mm}^3$) was virtually segmented into 20 cells (Figure 2.25).

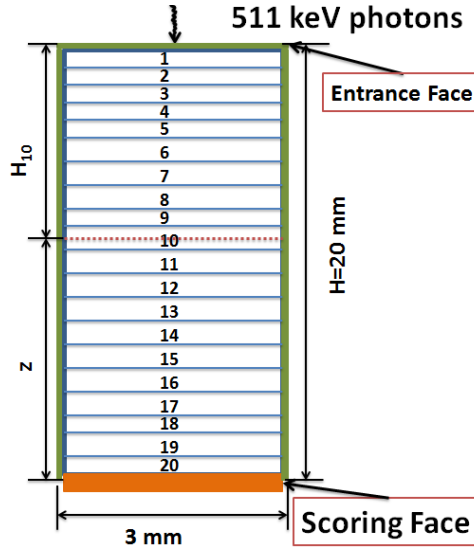


Figure 2.25: One single crystal was segmented into 20 cells along z-direction as defined in Figure 2.6 (a). z was the distance from the scoring face to i^{th} cell since our coordinate system originated at the scoring face.

Instead of throughout the entire crystal, two million optical photons were uniformly generated in each cell using the Polish-Metal combination (no scattering & absorption). Twenty final path length distributions for each cell were obtained. Each cell has its own propagation time distribution, or $D(H_i)$, where H_i is the height from the entrance face to the center of i^{th} cell so $H_i = H - z$ (e.g. H_{10} in Figure 2.25). Since the crystal was segmented equally and the attenuation of 511 keV follows an exponential distribution, the results from each cell were multiplied by position-weighted function $P(H_i)$, which gives the normalized exponential distribution of 511 keV photons in each cell:

$$P(H_i) = \frac{e^{-\mu_a(H_i-1)} - e^{-\mu_a H_i}}{1 - e^{-\mu_a H}} \quad (2.43)$$

where μ_a is the linear attenuation coefficient of a 511 keV annihilation photon in a scintillation crystal and H is the total length of crystal. $P(H_i)$ describes the fraction of the number of photons which were generated in that cell with respect to the total generated number of generated photons along the entire crystal. Therefore, the overall distribution is the sum of $P(H_i)D(H_i)$ (i.e. Green's function approach):

$$\text{overall} = \sum P(H_i)D(H_i) \quad (2.44)$$

For analytical validation, this global distribution has to be equivalent to the results of optical photons that are continuously exponential generated along the z-direction (uniformly in x-y direction). Refer to Figure 2.26, the Green's function approach method is consistent with original exponential results. Therefore, the optical photons are properly generated uniformly and exponentially generated in x-y and z direction, respectively.

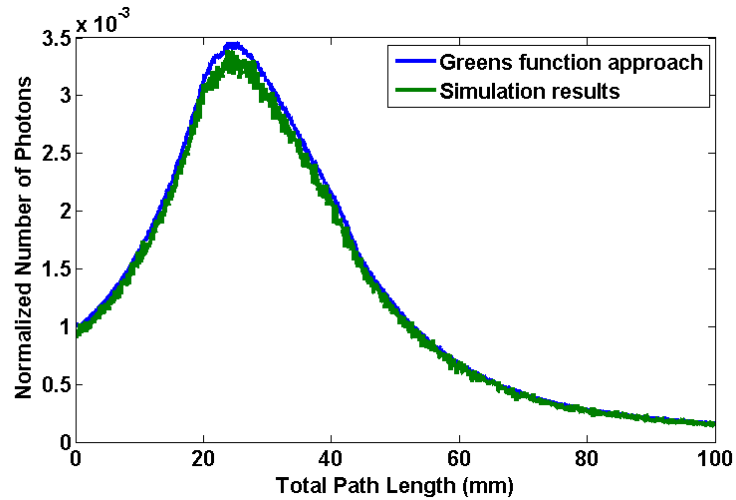


Figure 2.26: The simulation results of Green's function approach method and Beer-Lambert exponential for a $3 \times 3 \times 20 \text{ mm}^3$ crystal without intrinsic timing convolution and no scattering.

2.3.3 Simulation Validation Method

The goal of this work is to develop a simulation tool to model light propagation within crystals and optimize scintillation crystal designs (or detector module design) with improved energy and timing resolution for a TOF-PET system. Besides analytical verifications, our simulation results have to be validated thoroughly against experiments, in particular the modeling of timing behaviors and surface treatments. The performance of scintillation crystals depends on two major deterministic factors: light propagation output and temporal behavior of crystals. The former factor indirectly affects energy and timing resolutions, whereas the latter directly determines the crystal's capability for TOF-PET.

In simulations, the light propagation outputs are simply the integration of total output distribution results divided by the initial sampled optical photons (i.e. two million). To have high enough SNR information, usually the integration is taken up to three times of the decay constant (i.e. 40 ns) of scintillation light pulse, i.e. 120 ns. The rising edge of such output is linked to the time resolution of PET systems. For silicon detectors, the theoretical limit of the time resolution is determined by the ratio of noise to slope dV/dt of signal V (Figure 2.27) when its leading edge crosses the timing threshold [Spanoudaki et al. 2007]:

$$\Delta t (\text{FWHM}) = \frac{\sigma_{noise}}{dV/dt} \quad (2.45)$$

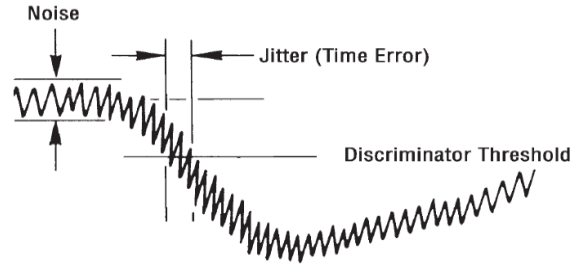


Figure 2.27: Jitter in leading-edge time derivation [ORTEC].

Therefore with the same noise level, the minimum timing resolution is obtained with larger slope value, and thus faster rising edge. In simulation, the slopes of rising edges of simulation results were used to investigate temporal behavior of light propagations as a function of crystal parameters. The validations here are preliminary steps such that experiment and simulation results are compared relatively among different situations. By doing this, no absolute simulation evaluation of various crystals will be provided. However we would at least have information about the relative performance among different crystals to guide our decisions and choices in detector design. It should be pointed out that the measured energy resolution in our work is the global energy resolution, whereas the light output in simulation only reflects the contribution of scintillation crystals. Such fact complexes the comparison we made here and needs further investigation. However it provides insightful information to make experiment results more understandable and helps guide experiment to the most promising configurations.

2.4 Simulation Results

2.4.1 Evaluation of simulation data fluctuation factors

2.4.1.1 Statistical variance

The statistical uncertainty of our simulation was investigated by sampling each configuration (i.e. surface-reflector combinations) ten times. Table 2.4 lists parameters used in simulation for $3 \times 3 \times 20 \text{ mm}^3$ LYSO crystal.

Table 2.4: Parameters of crystals and reflectors applied in simulations.

Linear Attenuation Coefficient (1/mm)	Index of refraction	Decay Time (ns)	Rise Time (ns)	Reflection Coefficient	
				ESR	Teflon Tape
0.086	1.81	41	0.5	0.985	0.985

The light output and rise-time slope results of all four configurations with the associated calculated standard deviation are listed in Table 2.5. The negligible standard deviations of light output and rise-time (except the light output result of the PolishMetal combination in which σ is ± 0.0021) imply that the simulation is reliable in its reproducibility.

Table 2.5: Statistical uncertainty evaluation results for all surface-reflector combinations.

	GroundMetal		GroundPaint		PolishMetal		PolishPaint	
	Light Output	Slope						
1	0.3733	0.0157	0.3860	0.0164	0.4745	0.0206	0.8027	0.0193
2	0.3729	0.0157	0.3858	0.0164	0.4743	0.0206	0.8026	0.0193
3	0.3729	0.0157	0.3855	0.0164	0.4748	0.0206	0.8025	0.0193
4	0.3734	0.0157	0.3859	0.0164	0.4746	0.0206	0.8026	0.0193
5	0.3732	0.0157	0.3859	0.0164	0.4749	0.0206	0.8026	0.0192
6	0.3726	0.0157	0.3862	0.0164	0.4743	0.0206	0.8027	0.0193
7	0.3727	0.0157	0.3858	0.0164	0.4745	0.0206	0.8028	0.0193
8	0.3727	0.0157	0.3866	0.0164	0.4746	0.0206	0.8027	0.0193
9	0.3731	0.0157	0.3858	0.0164	0.4743	0.0206	0.8026	0.0193
10	0.3733	0.0157	0.3858	0.0164	0.4752	0.0206	0.8025	0.0192
μ	0.3730	0.0157	0.3859	0.0164	0.4746	0.0206	0.8026	0.0193
σ	0.0003	0.0000	0.0003	0.0000	0.0003	0.0000	0.0001	0.0000

Note that the slope in Eq. 2.45 is determined depending on the value of the leading edge threshold. The threshold is set barely above the noise level so that the arrival time information is extracted without disturbance from noise. Similarly two points in the simulation results were used to calculate this slope (Figure 2.28).

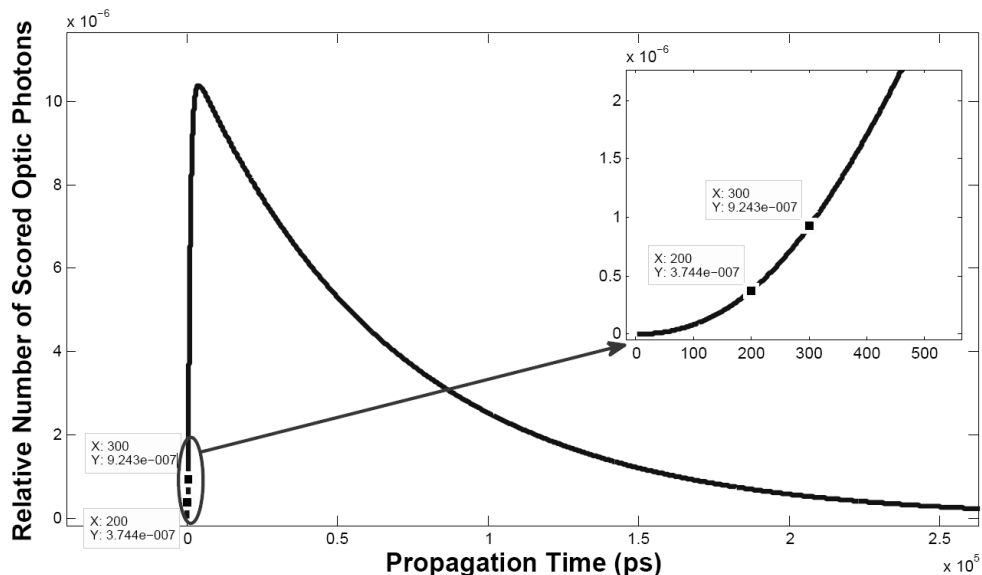


Figure 2.28: Typical simulation propagation time results with selection of two points for rise-time slope calculation. Other points were tested as well, and good consistency was observed.

2.4.2.2 Reflection coefficients of Teflon tape

As discussed previously, the reflection coefficients, R , of Teflon tape measured by different groups vary from 92% to 99%, which might lead to differences in the final results of light output and rise time slopes. Four typical reflection coefficients were sampled while other parameters were kept the same as shown in Table 2.4: 92%, 95%, 97%, and 98.5%.

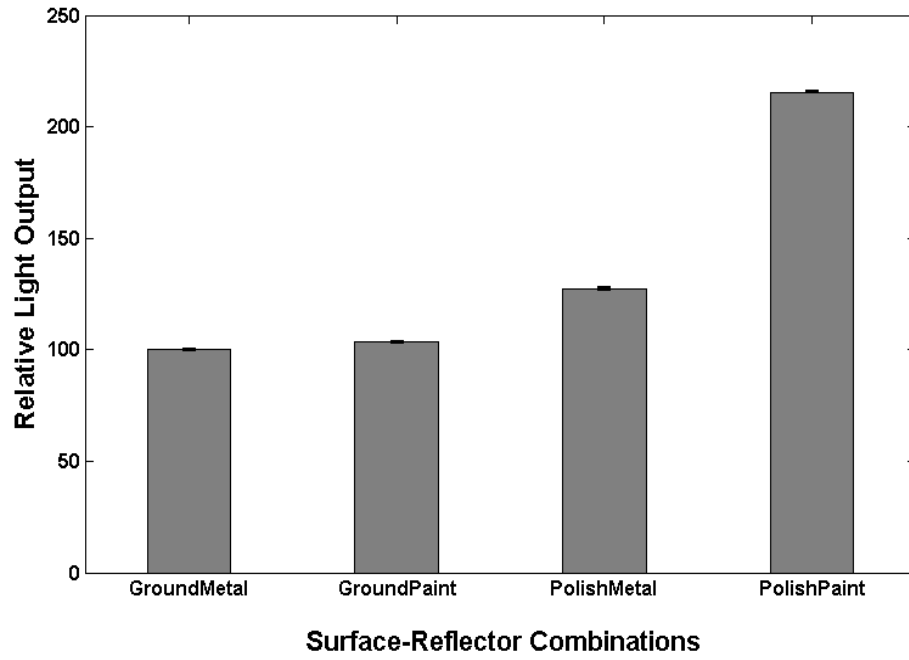
Table 2.6: Simulation results of light output and rise-time slopes for four typical reflection coefficients of Teflon tape. The standard deviations have been evaluated and are shown in Table 2.5.

R	GroundPaint		PolishPaint	
	Light Output	Slope	Light Output	Slope
92.0	0.3850	0.0164	0.8010	0.0192
95.0	0.3860	0.0164	0.8024	0.0193
97.0	0.3861	0.0165	0.8027	0.0193
98.5	0.3861	0.0164	0.8028	0.0193

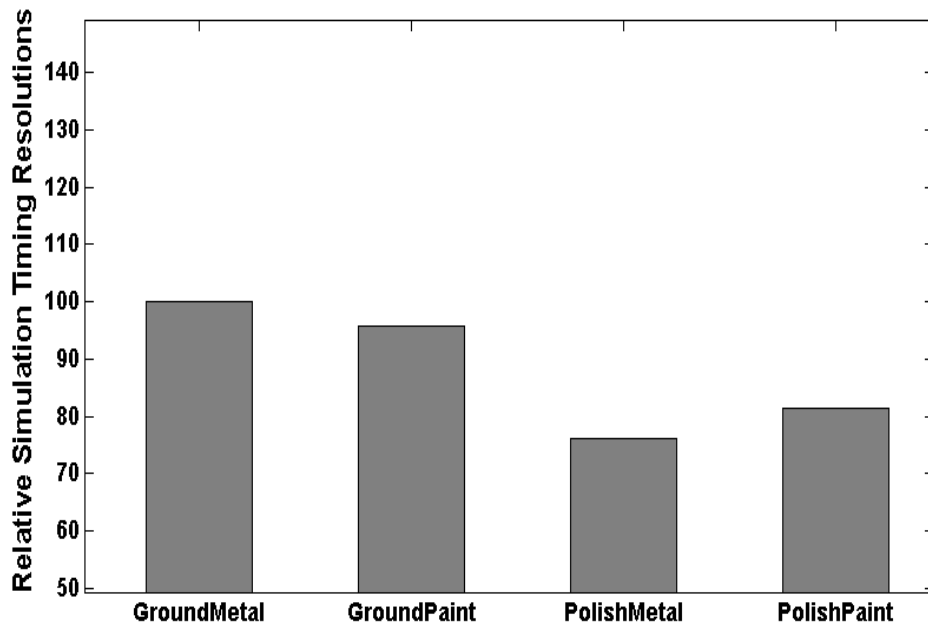
The above table implies that the simulation results of light output and rise-time slopes are not significantly influenced by different reflection coefficients (92% to 98.5%) for all four configurations. In order to thoroughly compare performances of four surface-reflector combinations, the reflection coefficient of Teflon tape used in simulation was assumed to be the same as that of ESR, 98.5%.

2.4.2 Results for validation

The GroundMetal configuration was used as the reference such that its results are set as 100 and the relative simulation results of light output and reciprocal of rise-time slopes of all other configurations are plotted in Figure 2.29.



(a)



(b)

Figure 2.29: Simulation results of relative light output and reciprocal of rise-time slopes for all four surface-reflector combinations. The error bars are too small to display due to negligible uncertainties (Table 2.5).

Chapter 3

Experimental Validation of Monte Carlo Simulation

This chapter aims to validate experimentally the simulations done in Chapter 2, with regard to the light output and temporal behavior of scintillation crystals. Energy resolution (i.e., inversely proportional to the light output) and time resolution for crystals with various surface treatment and reflector conditions were measured and compared to the simulation results.

3.1 Experiment Apparatus and Materials

To minimize background illumination, all measurements were performed in a self-designed light tight box (see Appendix C for details). Scintillation crystals convert energy deposited by 511 keV annihilation photons to optical photons, which are then detected by silicon photomultipliers (SiPMs). A sealed Na-22 source of 228.3 kBq activity was a positron source.

A glass holder made of Delrin was placed between the radioactive source and scintillation crystals to ensure the crystals are in close and stable contact with the SiPM by applying forces against crystal (see Appendix C). To provide mechanical support to crystals from the bottom crystals were oriented horizontally while the glass holder was moved vertically.

To maximize light collection at the photodetector's entry face, it is critical to guide these photons towards the photodetector by applying optical coatings (or reflectors) [Knoll *et al.* 1988, Janecek and Moses 2010]. In the simulation work done in Chapter 2, two types of reflectors were simulated: Metal and Paint. The former represents a specular reflector while the latter represents a Lambertian reflector. Accordingly, a high-performance enhanced Specular Reflectors (ESRs) and Teflon tapes were tested in our experiments. The ESRs provided by 3M Canada consist of multi-layer optical films with reflection coefficients above 98%. The Teflon tape used is ordinary polytetrafluoroethylene (PTFE) seal tape.

LYSO crystals were used in the experiments due to their excellent performance such as high light output, fast timing, and high stopping power. A summary of the parameters and configurations of the crystals tested is provided in Table 3.1

Table 3.1: The LYSO crystals used in experiments. All crystals are manufactured and assembled by Agile Technologies, Inc. For each surface-reflector scenario, we have evaluated 4 crystals and their codes (e.g. S/N 108333) are also included for future studies.

Surface-Reflector	Sample 1	Sample 2	Sample 3	Sample 4
3x3x20 mm³				
Polished-ESR	S/N 108333	S/N 108334	S/N 108335	N/A
Polished-Teflon	S/N 108337	S/N 108338	S/N 108339	S/N 108340
As Cut-ESR	S/N 108341	S/N 108342	S/N 108343	S/N 108344
As Cut-Teflon	S/N 108345	S/N 108346	S/N 108347	S/N 108348

Each surface-reflector combination had 3-4 samples allowing evaluation of performance fluctuations among different samples. The “As Cut” and “Polished” treatment represents Ground and Polish surface models in the simulation, respectively. For coincidence timing measurements, a 4x4x4 mm³ LYSO crystal wrapped with Teflon tape was coupled to a PMT, also provided by Agile Technologies, Inc.

In order to enhance coupling and match indices of refraction, the crystals were coupled to the SiPMs with silicone optical grease (BC-630, index of refraction: 1.465), obtained from Saint-Gobain Ceramics & Plastics, Inc.

For energy measurements, SiPMs and PMTs measure the signal caused by optical photons from scintillators and produce electrical pulses. The total number of visible photons (and photoelectrons) determines the amplitude of the pulses. For time measurements, two detectors were configured in a coincidence mode and the timing information of pulses from each detector was obtained. The PMT is R10560 provided by Hamamatsu Photonics K.K. It has a gain of 1×10^6 and is able to provide fast timing response for scintillation counting.

The SiPM devices (S10362-33-050C series) were provided by Hamamatsu Photonics. It has an effective active area of 3x3 mm² and a gain up to 7.5×10^5 . The output pulses from SiPM were processed through a current amplifier with a gain of 1000 ohms to form a pulse of high amplitude (~ from 0 to 1 V). An example of the waveform of a typical SiPM signal is shown in Figure 3.1.

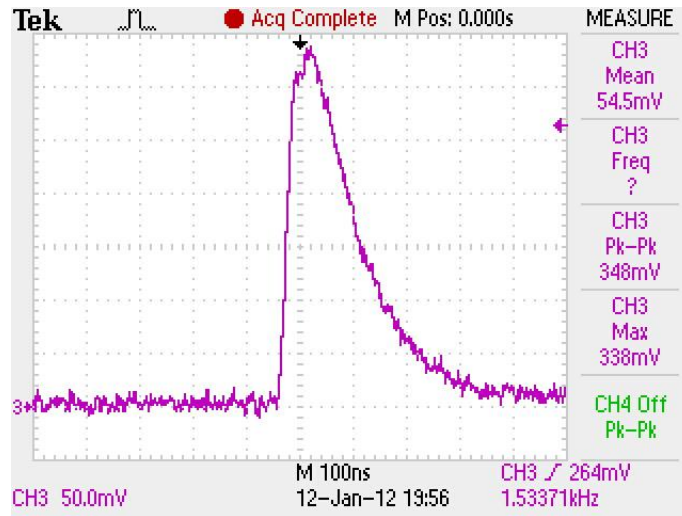


Figure 3.1: Typical raw waveform of a detected signal by the SiPM.

The pulses were sampled with a high performance analog-to-digital convertor (ADC) provided by CAEN, Italy. The CAEN V1721 is a free-running type ADC and consists of 8 channels operating at a 500 MS/s clock rate. Signals from the ADC were transmitted into a computer via VME-PCI optical bridge link (CAEN A2818). A typical raw SiPM signal pulse sampled by the ADC is shown in Figure 3.2.

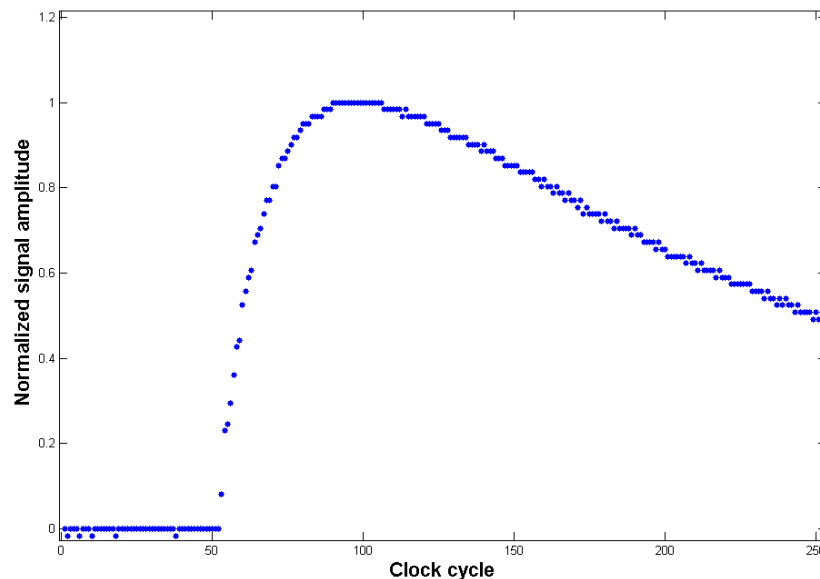


Figure 3.2: Raw waveform capture of detector signals with a free-running ADC. The maximum signal amplitude is normalized to be one. The digitized waveforms are to be used for further processing such as pulse shaping and time pickoff.

Finally, the digitized signals were viewed and recorded as text files in the computer with data acquisition software, CAENScope or Wavedump, provided by CAEN. The data analysis and signal processing for the measurements were performed in MATLAB.

3.2 Energy Resolution

3.2.1 Experiment Set-up and Methods

The experiment setup for measuring energy resolution is shown in Figure 3.3. The biased voltage of SiPM was set at 71.5 V, according to the specification provided by the vendor. The distance between the sealed source and the SiPM was ~ 5 cm.

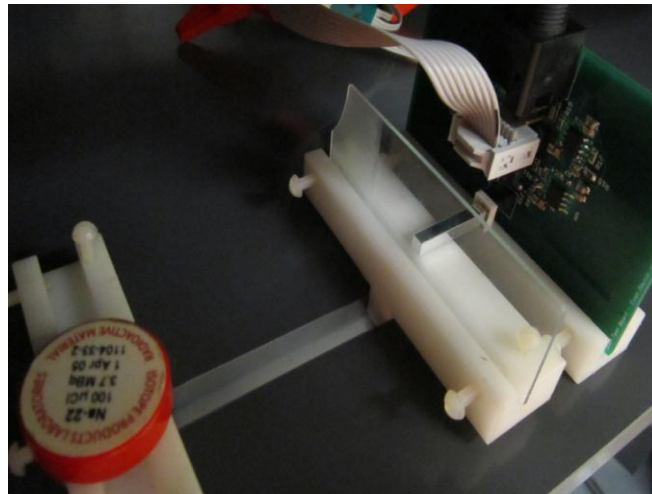


Figure 3.3: Illustration of experiment setup for energy resolution experiment.

To distinguish scintillation light based pulse events from low amplitude electrical noise, the trigger threshold was set to just above the noise and baseline levels. Energy spectra were required in order to find energy resolution of different crystals. As discussed before, the integrated charge from a scintillation event is proportional to deposited energy from incoming annihilation photons. Therefore, each signal pulse being continuously sampled by the CAEN ADC including multiple points, which need to be integrated to find the total amount of charge. *Triangular shaping* was used in this work [Peng et al. 2007], which is an optimum shaping method to provide the best signal-noise-ratio, in theory. It can be implemented by calculating the difference between two free running averages of length L separated by a gap G at the k^{th} sample [Peng et al. 2007]:

$$\mathbf{L} \cdot \mathbf{V}_{x,k} = - \sum_{i=k-2L-G}^{k-L-G} V_i + \sum_{i=k-L+1}^k V_i \quad (3.1)$$

where L and G were selected until optimum condition of energy resolution was achieved. Such output was derived for each 511 keV event and used to form an energy spectrum to be shown later. Note that in digital electronics such as Field Programmable Gate Arrays (FPGAs), the triangular shaping was easier to be implemented than Gaussian shaping.

The steps for analysing energy resolution are explained below. A curve fitting code was developed to fit the 511 keV photopeak showing on the energy spectrum to the function below, which consists of a linear background plus a Gaussian curve:

$$CFF = ax + b + \frac{1}{\sqrt{2\pi\sigma^2}} e^{-\frac{(x-\mu)^2}{2\sigma^2}} \quad (3.2)$$

where μ is peak position (i.e. E_0) and σ is standard deviation. The energy resolution, R , was then calculated according to Eq. 1.6.

To correct for potential non-linearity of the detector response (scintillator/SiPM) and zero-offset of the ADC, we calibrated the detection system with three energy peaks. Besides two energy peaks of the Na-22 source (511 and 1274 keV), a Co-57 source ($t_{1/2}=271.79$ days) with energy peak at 122 keV and activity of about 63.5 μCi (or 2.35 MBq) was used due to its availability.

3.2.2 Measurements of Energy Resolution

There are a number of factors affecting the accurate measurement of energy resolution, such as crystal placement, crystal sample (i.e., manufacture process), reflector wrappings, system stability, signal processing, as well as statistical variance. Multiple samples for each configuration allow us to evaluate uncertainties among crystal samples including differences in wrappings, plus uncertainties associated with crystal replacement (e.g., one needs to replace crystal samples after a single measurement). To ensure precise measurement of energy resolution, two other sources of variance in energy resolution measurements are discussed below:

3.2.2.1 Statistical variance

Sufficient counting statistics are required to accurately measure pulse amplitude and energy resolution, associated with the binning in forming a pulse height spectrum. There is a trade-off between collection time and required number of counts samples to minimize statistical variance. To investigate influences on energy resolution due to statistical variance, we studied the energy resolutions as a function of counts collected (to be discussed in 3.4.2). For each pre-set amount of counts, five measurements were repeated to find the uncertainty. The average uncertainty is obtained from these five data sets by the following equation:

$$\sigma_{\bar{x}} = \frac{1}{N} \sqrt{\sigma_{x_1}^2 + \sigma_{x_2}^2 + \cdots + \sigma_{x_N}^2} \quad (3.3)$$

where N is the number of sample sets (i.e. five).

3.2.2.2 Signal processing

Another two sources of uncertainty of energy resolution measurements are: 1) the signal processing procedure in terms of G and L parameters in the triangular shaping method (Eq. 3.1); 2) the number of bins in pulse height spectrum. Energy resolution as a function of both bin numbers and different values of G and L parameters was studied.

3.3 Coincidence Timing Resolution

In this subsection, the experimental setup and methods for measuring coincidence timing resolutions will be discussed.

3.3.1 Experiment Set-up

The experimental setup is shown in Figure 3.4. The SiPM was placed in a coincidence mode against a fast PMT. Two ADC channels were used. The supply voltage for the PMT was set at 1400V. The source-LYSO (SiPM) distance was about 3 cm, and the source-LYSO (PMT) distance was approximately 7cm.

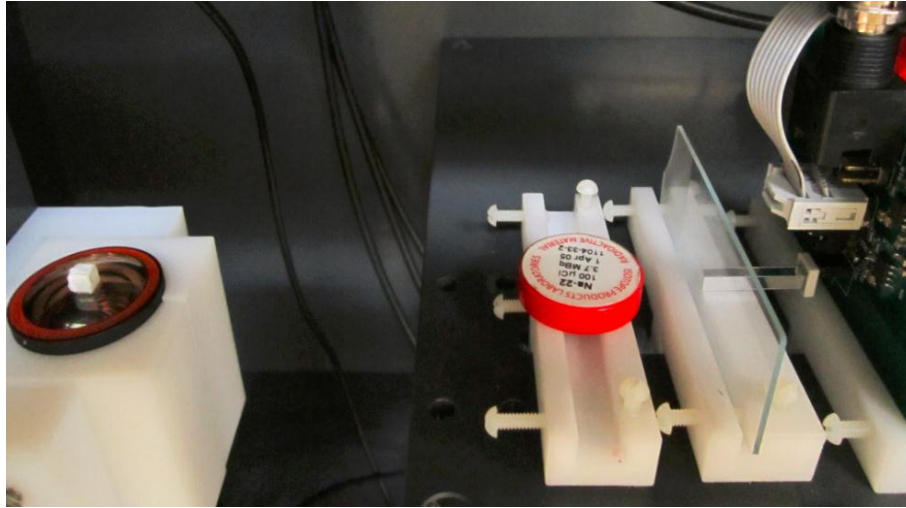


Figure 3.4: Illustration of experiment setup for coincidence timing resolution experiment.

3.3.2 Coincidence timing resolution measurements

3.3.2.1 Coincidence Events Selection Method

To reject those single and random events (i.e., non-coincidence mode), we used the following method, as explained in Figure 3.5. There are two pulses from channel 0 and 1, separately. Only the trigger signal from the channel 0 is activated and used to generate a time window of 100 ns which is approximately the width of the PMT pulse. When the pulse from the channel 1 falls within the time window, it will be recorded; otherwise it will be discarded for saving memory. It is also possible to generate a time window based on the triggers from both channels (i.e., time-to-amplitude converter), which would further the efficiency of data acquisition and storage. However, the CAEN system currently does not support that function. In the end, two set of data files from two ADC channels were processed in MATLAB to extract timing information.

In addition, the scatter events were also discarded by setting energy threshold (i.e. energy gated) around the 511keV energy peak. In our experiment, no trigger was applied to the SiPM signals since the count rate of PMT signals is much lower than that of the SiPM. For the proposed geometry, only approximately 3-5% of the total recorded events are coincidence events.

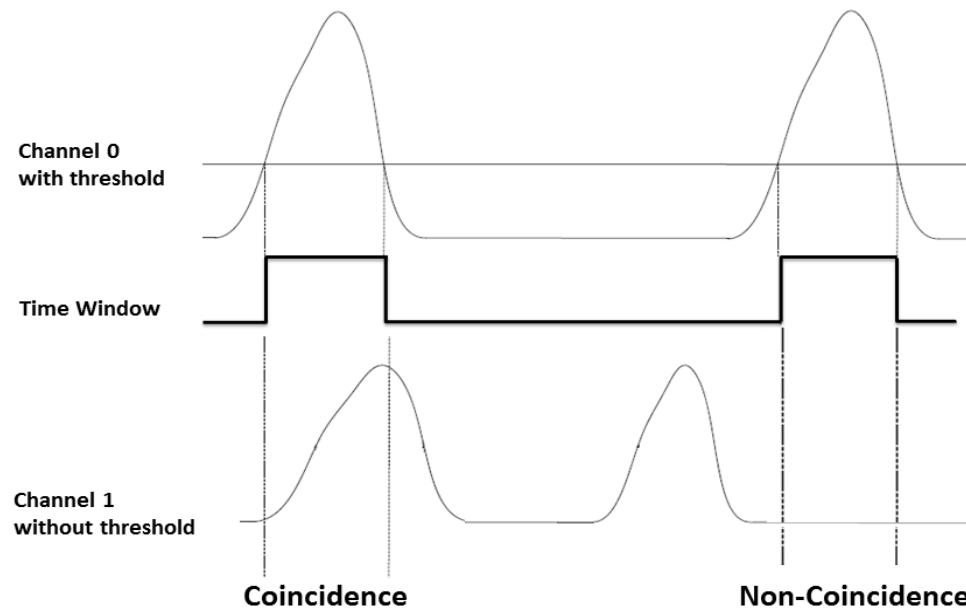
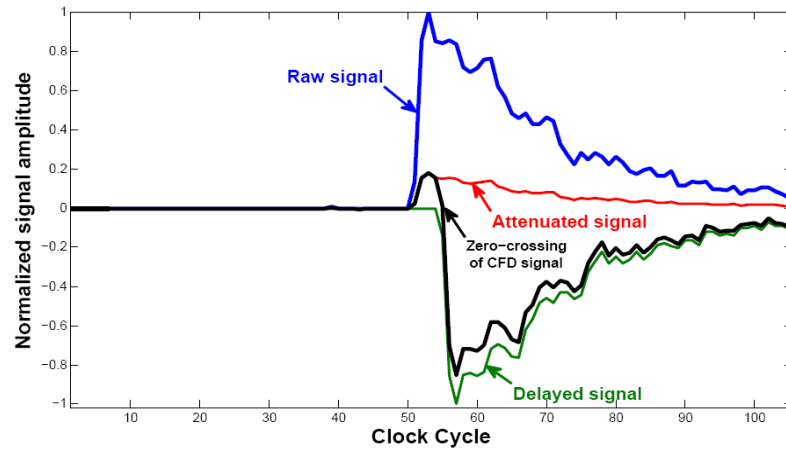


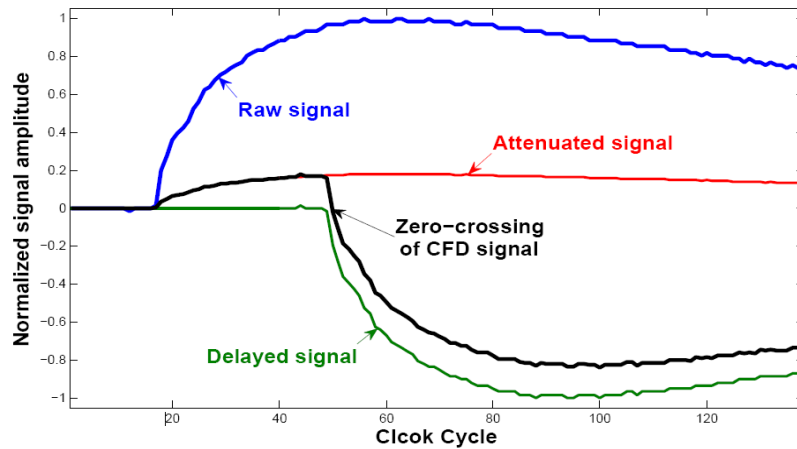
Figure 3.5: Illustration of selecting coincidence events between channel 0 & 1. Only those channel 1 signals within timing window of channel 0 signals are considered as coincidence events. This plot is modified based on [CAEN 2012].

3.3.2.2 Time Pick-off Methods

As mentioned earlier, coincidence timing resolution is one of the important factors for evaluating performance of a PET system. It is commonly defined as FWHM of coincidence time distribution (time spectrum), which is a histogram of the difference in arrival times of two coincident annihilation photons detected by two separate detectors. To extract the timing information from raw pulses, three time pick-off algorithms were used here: *constant fraction discrimination* method (CFD), *linear fitting* methods and *exponential fitting* methods. [Knoll 2000, Chapter 17]. The applicability, performance, and optimization of different methods for timing pick-off depends on properties of the signal and is currently being investigated by different groups [Hu W *et al.* 2010, Codino 2000, Nelson *et al.* 2003]. The CFD [Labruyere *et al.* 2007, Peng *et al.* 2007] was first used to extract timing information to avoid amplitude walk and to help minimize time-jitter due to random noise [Knoll 2000, Chapter 17]. The principle of CFD is similar to that of analog CFD, as explained in Figure 3.6. The original signal is attenuated by a factor of f and then added to an inverted signal of certain delay (D). The accuracy of this algorithm depends on the optimization of these two parameters. The result will be a bipolar signal. By finding the position of zero-crossing using interpolation, one is able to derive the time information more accurately than the leading-edge method.



(a)



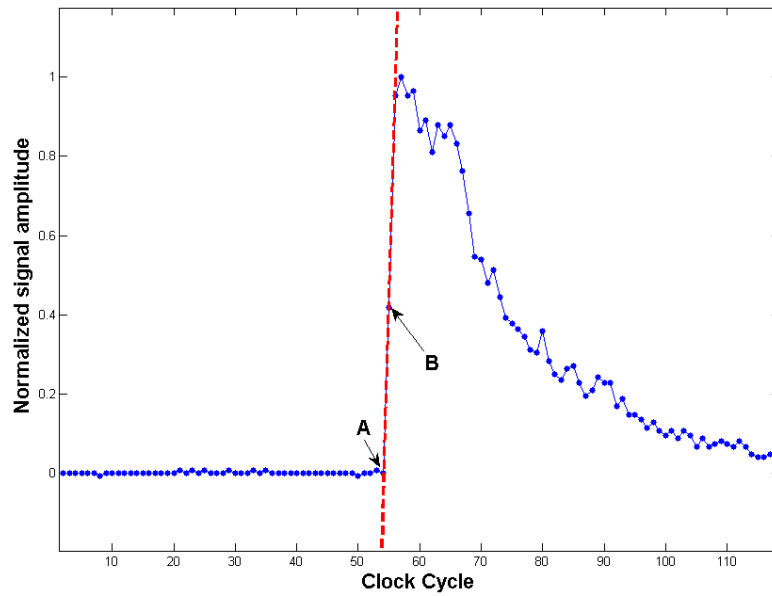
(b)

Figure 3.6: An example of components for CFD with (a) PMT and (b) SiPM signals.

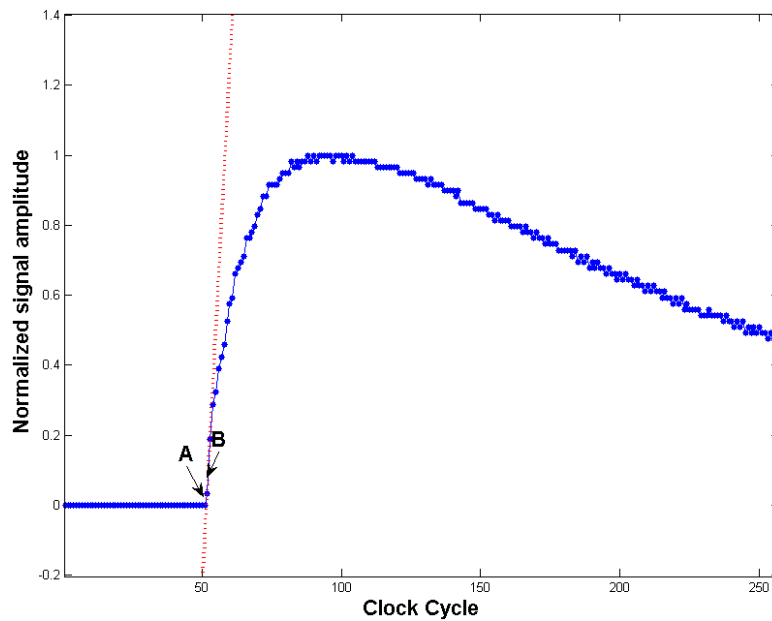
Besides CFD, linear and exponential rising-edge fitting methods were also tested for comparison and are shown in Figure 3.7. The clock rate of the ADC is not fast enough to provide sufficient sample dots for the fast PMT as shown in Figure 3.7 (a). Therefore for both PMT and SiPM signals, only two sample points on the rising edge were used to extract arrival time information by linearly or exponentially fitting method for consistency purpose although the SiPM signal has enough sample dots. The linear and exponential fitting equations are shown as follows:

$$\begin{cases} V_{LF}(k) = ak + b \\ V_{EXP}(k) = 1 - e^{-\frac{(k-k_0)}{\tau}} \end{cases} \quad (3.4)$$

The fitted parameters (a , b , k_0 , and τ) were substitute to the equations to find the k value that gives zero values of V_{LF} and V_{EXP} .



(a)



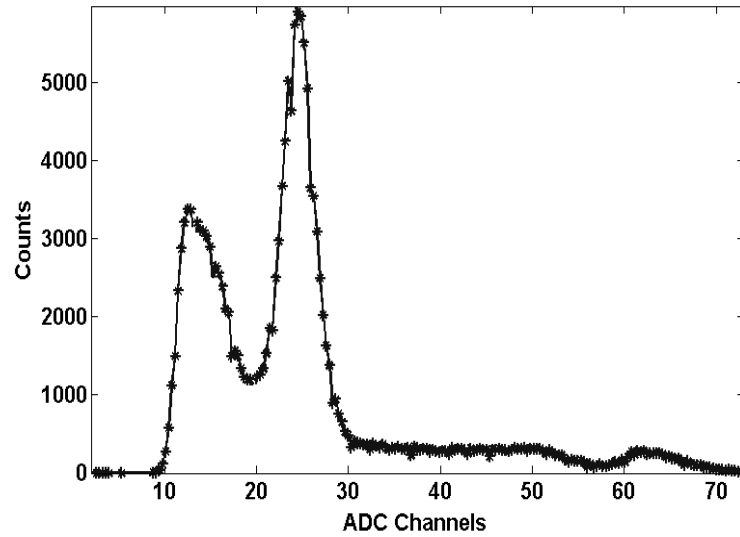
(b)

Figure 3.7: Illustration of linear (or exponential) rising edge fitting time pick-off method for (a) PMT, and (b) SiPM signals. Two points (A and B) on the rising edge were used for fittings. The baseline of each signal was removed for accuracy of time pick-off procedure.

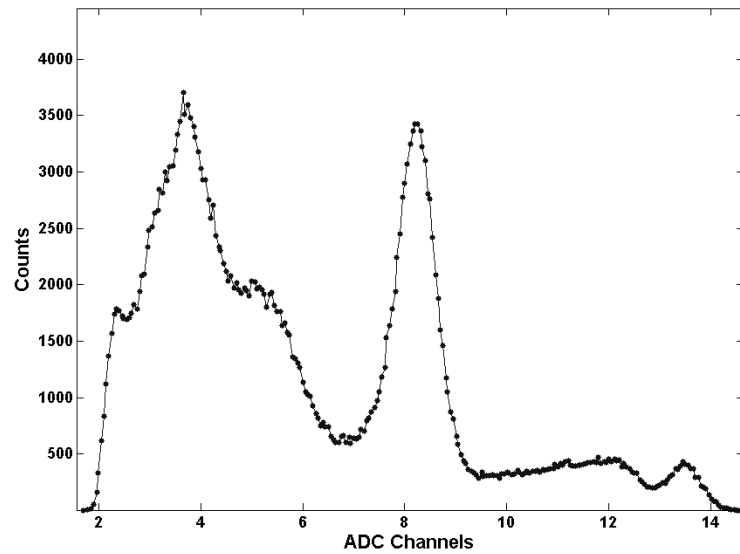
3.4 Experimental Results

3.4.1 Calibration for linearity

The energy spectra of Na-22 without calibration using the triangular shaping method (Eq. 3.1) are shown in Figure 3.8, for both PMT and SiPM.



(a)

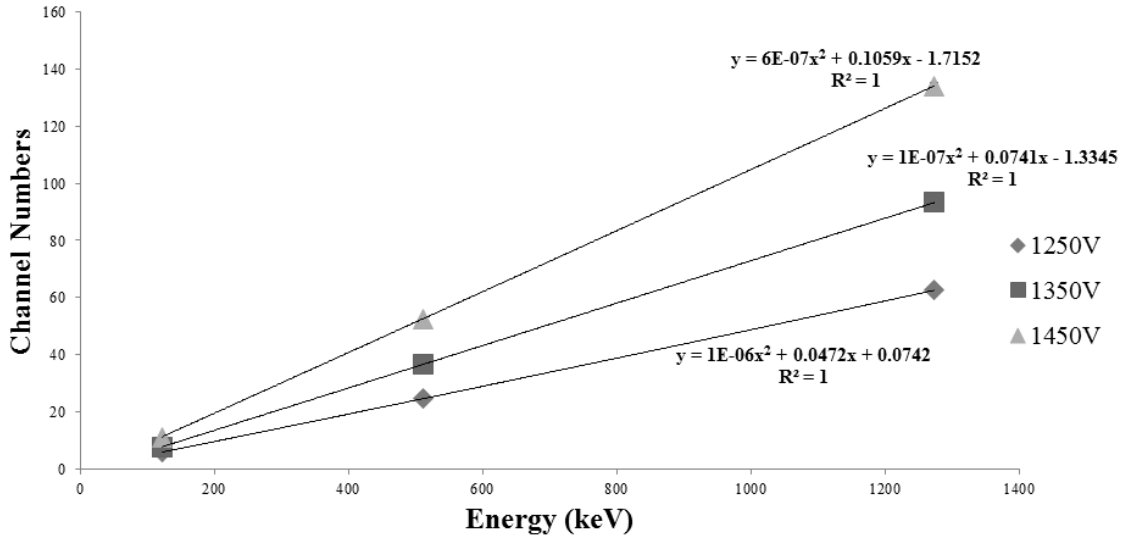


(b)

Figure 3.8: Na-22 energy spectra with Compton continuum for (a) PMT with 1250V and (b) SiPM with 71.5 V bias voltage before calibration. The testing crystal was S/N 108333.

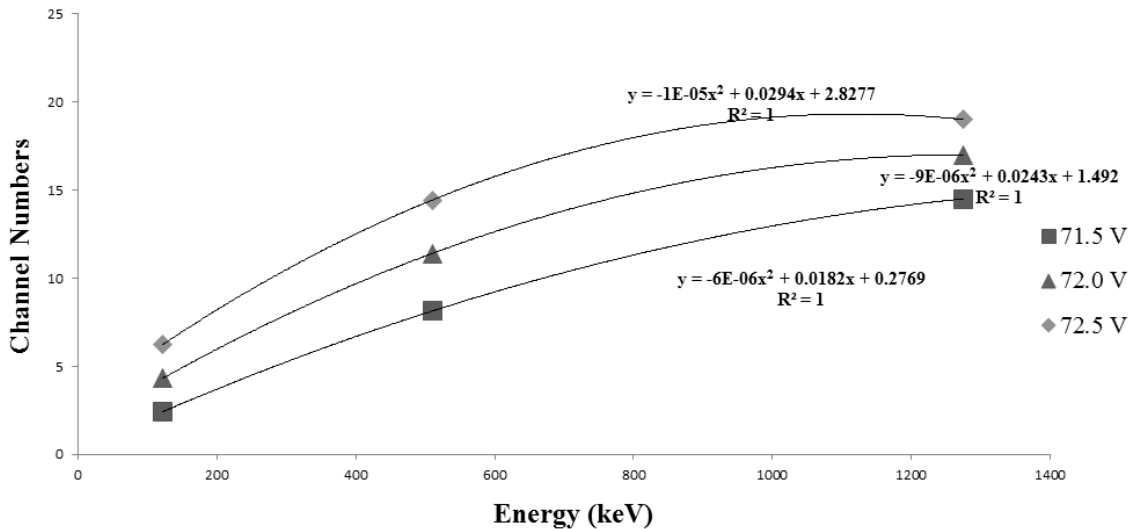
For PMT, the ratio between the measured amplitudes of 1274 keV and 511 keV peaks is 2.547, in good agreement with the expected value of (1274/511=2.490). While for SiPM, the ratio from the measurement is 1.999, which implies a non-linear detector/system response to be corrected. The calibration with three energy peaks is plotted in Figure 3.9.

Energy Peak Positions v.s. Ch # for PMT with Different Applied Voltage



(a)

Energy Peak Positions v.s. Ch # for SiPM with Different Bias Voltage

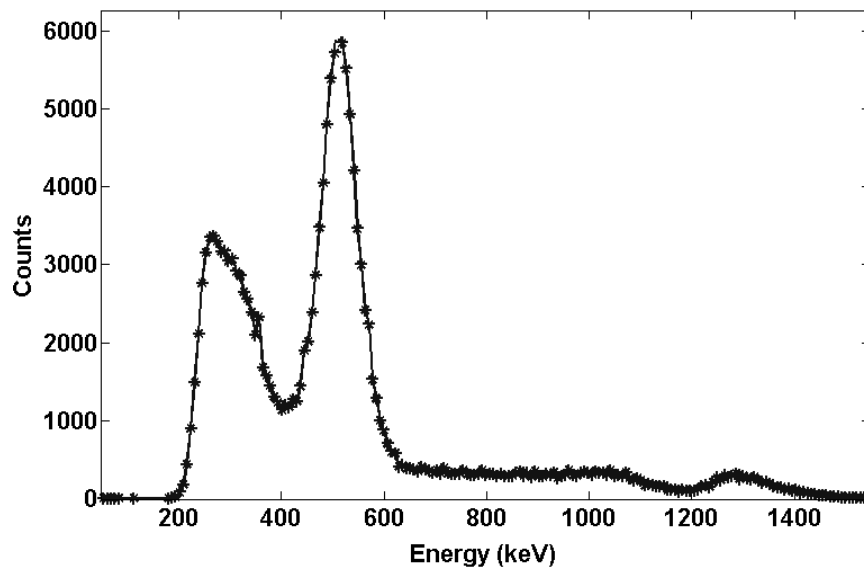


(b)

Figure 3.9: Calibration of channel numbers of ADC and energies with three energy peaks for both (a) PMT and (b) SiPM. The energy peaks are associated with a polynomial model.

The results of the PMT show better linearity than that of the SiPM, over the range between 1200-1400 keV. In addition, the results of SiPM appears more linear with lower bias voltage (e.g. 71.5 V) than higher ones (72 V and 72.5 V), which is in good agreement with published literature [Dolgoshein 2004].

One explanation for the non-linearity for SiPM is due to the saturation of avalanche photodiodes (i.e., microcells), the number of which determines the dynamic range. The SiPM used in this work has ~3600 APD micro cells, whereas a LYSO crystal hit by 511 keV high energy photons emits approximately 4600 primary photons to irradiate all microcells. More discussion about this saturation can be found in [Seifert et al. 2009, van Dam et al. 2009]. Figure 3.10 shows calibrated Na-22 energy spectrum with energies instead of ADC channel numbers as shown in Figure 3.8. In the following studies, 71.5 V bias voltage was used due to its good linearity.



(a)

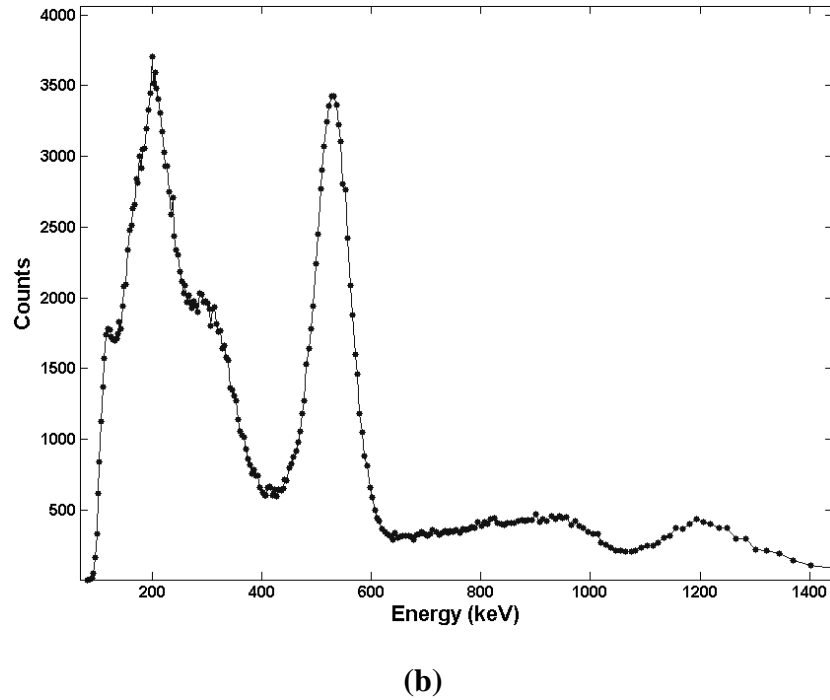


Figure 3.10: Calibrated Na-22 energy spectrum for (a) PMT and (b) SiPM with the “S/N 108333” crystal.

3.4.2 Evaluation of Experimental Data Fluctuation Factors

3.4.2.1 Energy resolution

The results of energy resolutions measurements as a function of total counts, bin numbers, and signal processing are shown in this section. An example of a calibrated Na-22 energy spectrum with the Gaussian curve fitting as discussed in the section 3.2.1 is shown in Figure 3.11.

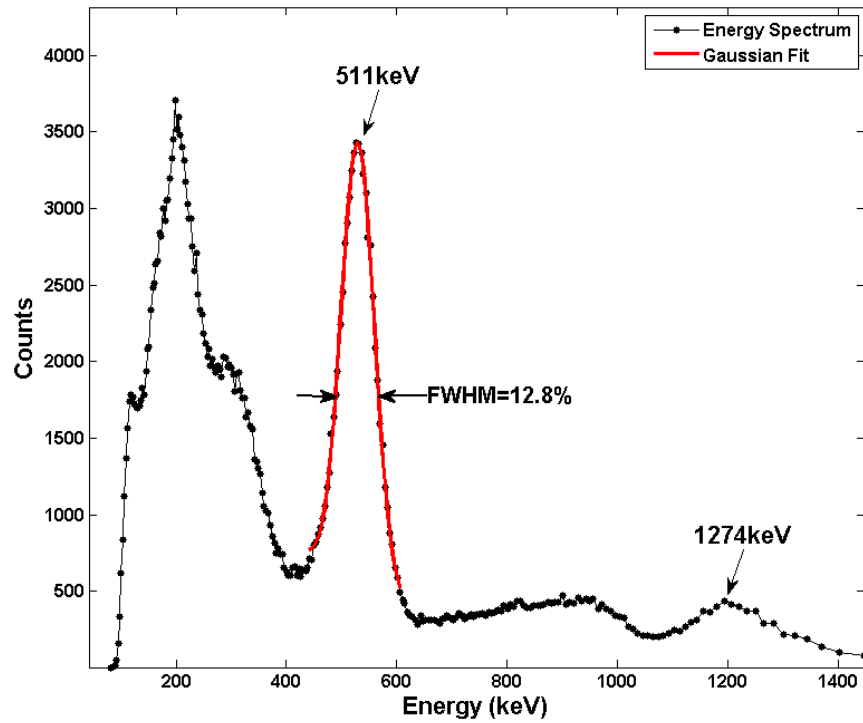


Figure 3.11: A example of a calibrated Na-22 energy spectrum using triangular shaping method with Gaussian curve fitting method. The triangular shaping methods and Gaussian curve fitting method are discussed in the section 3.2.1.

- **Statistical Variance**

Figure 3.12 shows a plot of energy resolution as a function of the total measured number of annihilation photons.

The plot implies that the required counts for measuring energy resolution with good stability (small error bars) is 200,000, which has been used to guide the experimental design in the subsequent sections.

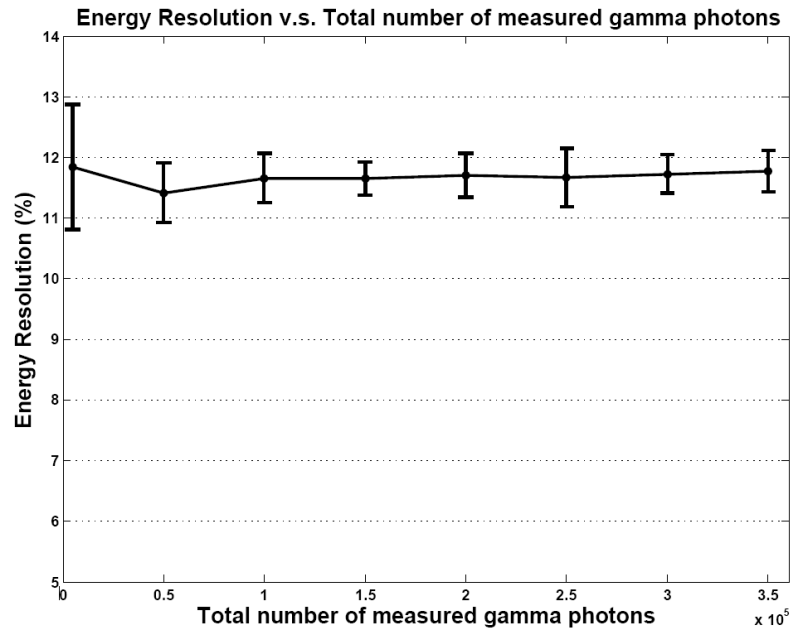


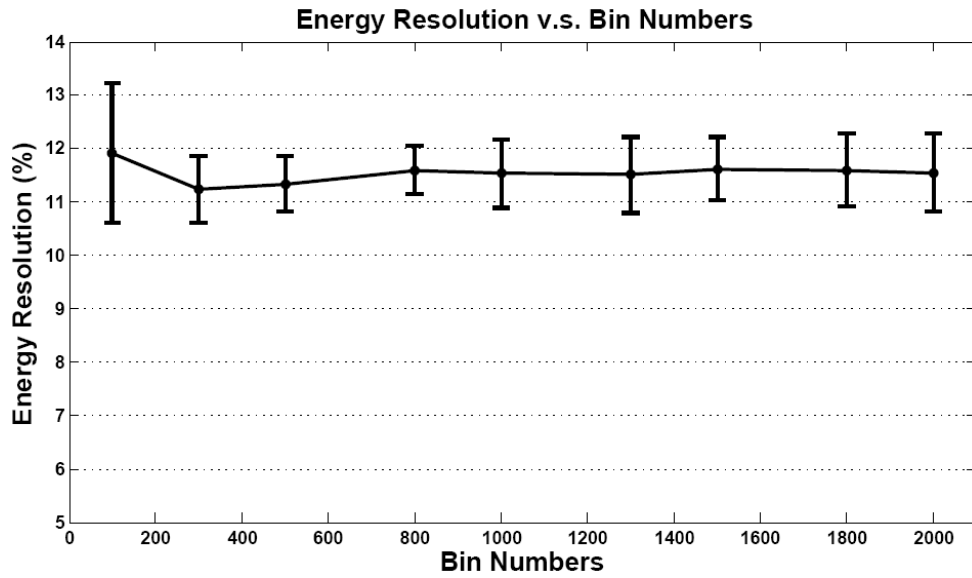
Figure 3.12: Energy resolution versus number of measured annihilation photons. The energy resolution does not vary with number of measured annihilation photons above a certain amount. The error bars are uncertainties from curve fitting process.

- **Signal Processing**

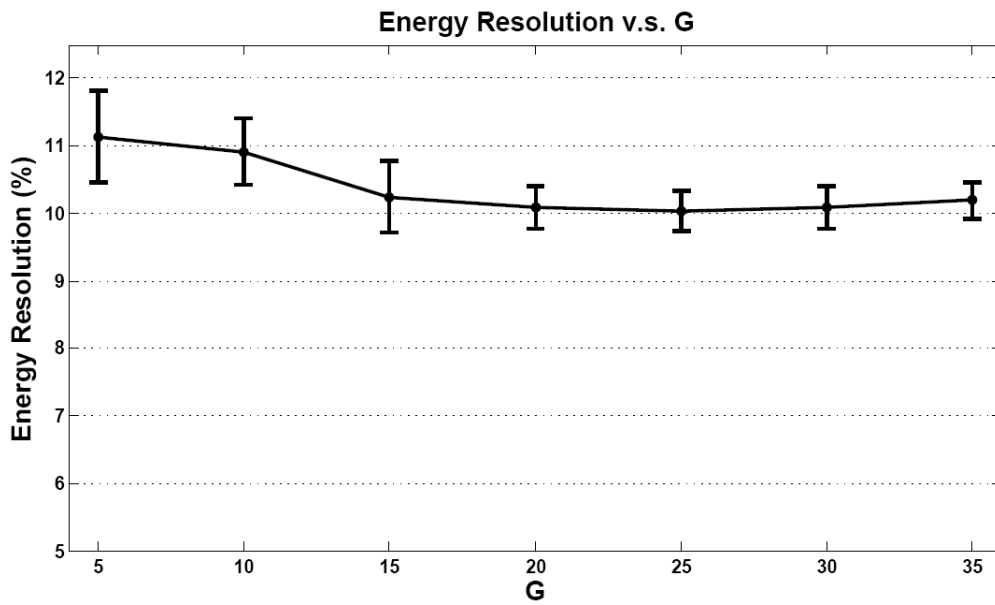
The measured energy resolution as a function of bin numbers and signal processing parameters (G and L) are plotted in Figure 3.13. The number of bins is calculated as the difference between the maximum and minimum values of the integrated charges from the triangular shaping methods divided by a certain bin width. Refer to Figure 3.13 (a), the energy resolution at 100 bin numbers is $11.9 \pm 1.3\%$, and it decreases to approximately 11.6% and appears to be stable for bin numbers higher than 800 at which the energy resolution is $11.6 \pm 0.4\%$. In addition to the stabled energy resolution, the 800 of bin number for energy spectrum is used due to its lowest uncertainty among the tested bin numbers.

As shown in Figure 3.13 (b) & (c), for sufficiently large number of bins (i.e. 800), the energy resolution is no longer influenced by G & L. Likewise, for large enough G and L used during the triangular shaping method, the energy resolution appears to be stable. For the smallest G number, i.e. G is equal to 5, the energy resolution is $11.1 \pm 0.7\%$. The relatively higher energy resolution implies that higher G number is preferred to have a stabled energy resolution. Therefore the number of 20 is used for G value where the

energy resolution is $10.1 \pm 0.03\%$. With the same idea, due to the relatively stabled energy resolution and its lower uncertainty, the number of 20 is used for L value at which the energy resolution is $10.1 \pm 0.3\%$.



(a)



(b)

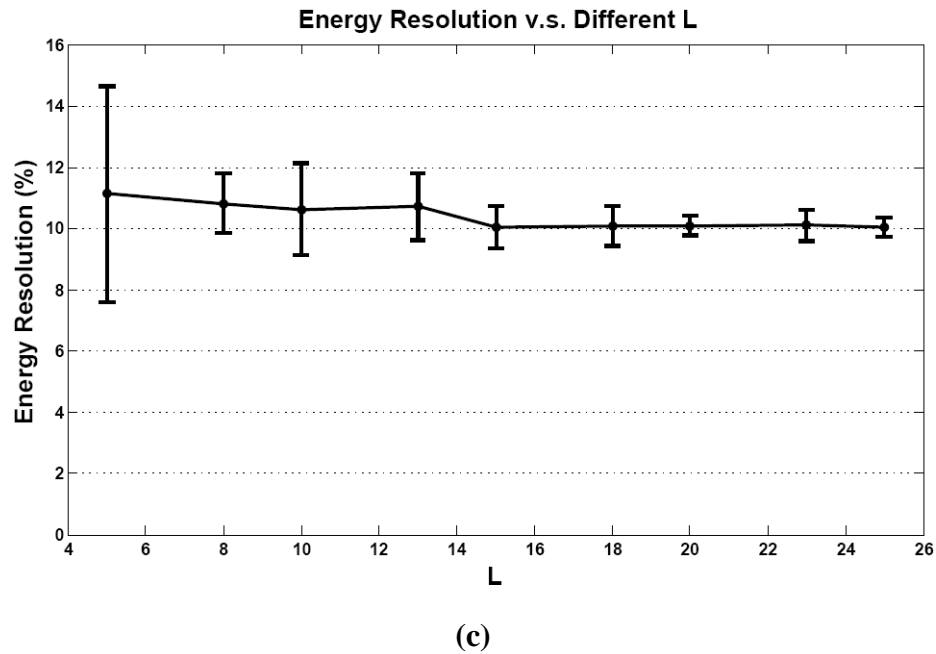


Figure 3.13: Energy resolution as a function of: (a) bin numbers used in curve fitting and of triangular shaping parameters; (b) G; and (b) L with 200,000 annihilation photons. The error bars are uncertainties from curve fitting process.

3.4.2.2 Timing resolution

An example of coincidence time spectrum of difference of the arrival times between two detectors with Gaussian curve fitting is shown in Figure 3.14.

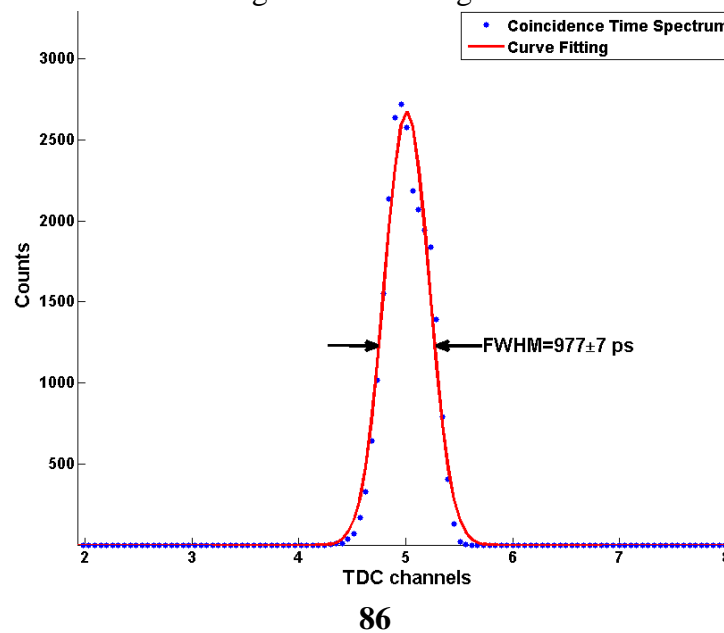


Figure 3.14: Example of a coincidence time spectrum using the CFD time pick-off method. The spectrum was fitted with Gaussian function. The attenuated factor, f , was set as 0.18, the delayed time settings of PMT (D_p) and SiPM (D_s) were 4 and 32, respectively. The crystal was the “S/N 108341”. The ADC has 500MS/s sampling rate so that the time difference between two ADC sample dots are 2 ns. The display on horizontal axis of time spectrum was transferred from ADC channels to difference in arrival time by multiplying each ADC channels by 2.

- **Statistical Variance**

The dependency of coincidence timing resolution on the statistical variance is plotted in Figure 3.15. The timing resolution at lower numbers of detected coincidence events is higher than that at higher numbers (e.g. the timing resolution for 1000 and 20,000 coincidence events is 0.987 ± 0.031 ns and 0.934 ± 0.007 ns). To produce stable measurements results of time resolution, we found that 20,000 coincidence events are necessary. Since only 3% to 5% of total recorded events are in coincidence, a larger amount of counts is required (i.e., 600,000 for both PMT and SiPM).

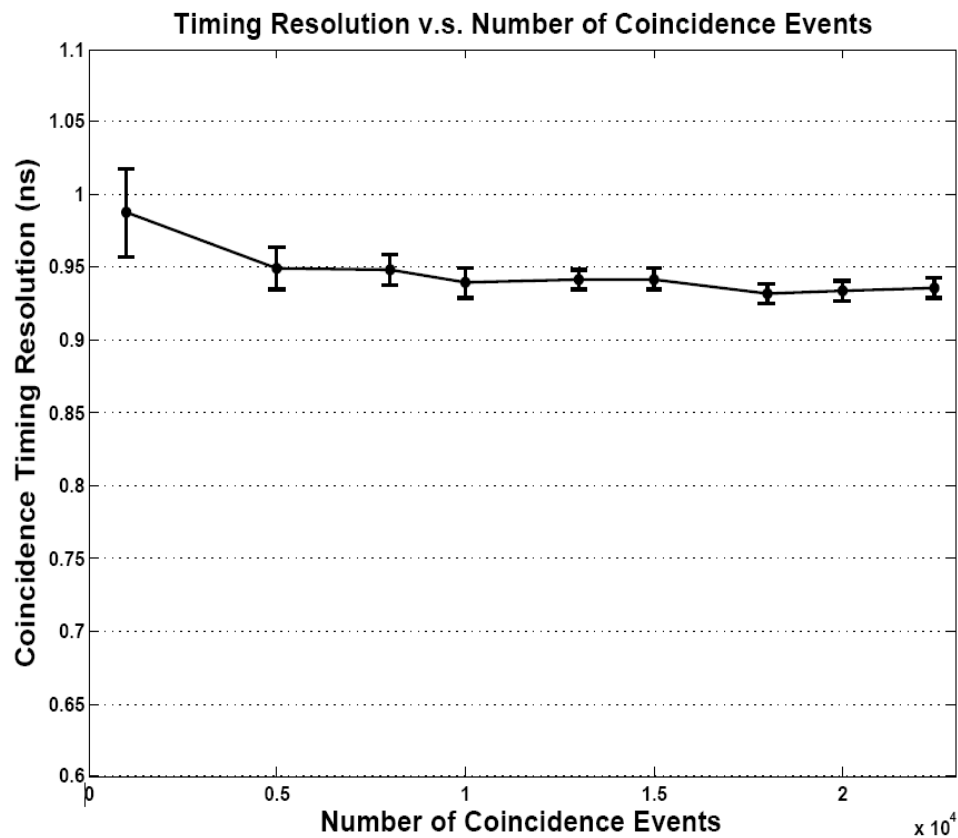


Figure 3.15: Coincidence timing resolution as a function of the total number of coincidence events. The error bars are uncertainties from curve fitting process

- **Signal Processing**

The dependency of coincidence timing resolution on the bin numbers is plotted in Figure 3.16. The timing resolution at 100 bin numbers is 1.026 ± 0.023 ns, and it decreases to approximately 0.936 ns and appears to be stable for bin numbers higher than 800. The selection of 2000 bin numbers is able to produce stable measurements results of time resolution, which is equal to 0.936 ± 0.007 ns. In addition to the stabled energy resolution, the bin number at 2000 for timing spectrum is used due to its relatively lower uncertainty among the tested bin numbers. Note that the clock sampling of the CAEN ADC system is 500 MHz (2 ns sampling interval), the bin size corresponding to a total of 2000 bins is ~ 110 ps since the difference between the maximum and the minimum arrival times of the timing spectrum is ~ 220 ns.

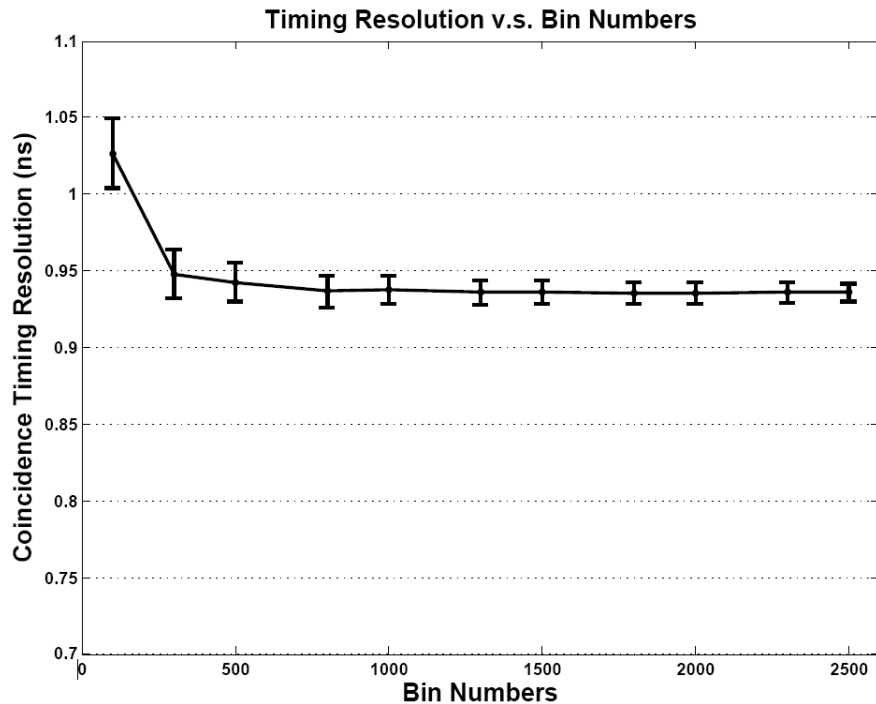


Figure 3.16: Coincidence timing resolution as a function of the bin numbers used in curve fitting. The error bars are uncertainties from curve fitting process.

Note that for the CFD method, both the timing resolution and time spectrum is not significantly dependent on attenuation factor, f , but strongly imposed by delay time settings. Therefore, these CFD parameters were optimized until good timing spectra were obtained. Figure 3.17 demonstrates four example timing spectra with four CFD parameter settings. Although better timing resolutions are achieved such as 475 ± 8 ps and 566 ± 5 ps (Figure 3.17 (a) & (b)), the curve fittings of time spectra are not satisfactory in terms of

how well the fitting curves approximate to real time spectra. After optimization of CFD parameters, the 0.18 was chosen for attenuation factor, f and delayed time constant for PMT (DP) and SiPM (DS) were determined as 4 and 32, respectively for all CFD time pick-off methods since relative results of energy and timing resolutions among surface-reflector combinations are used for validation.

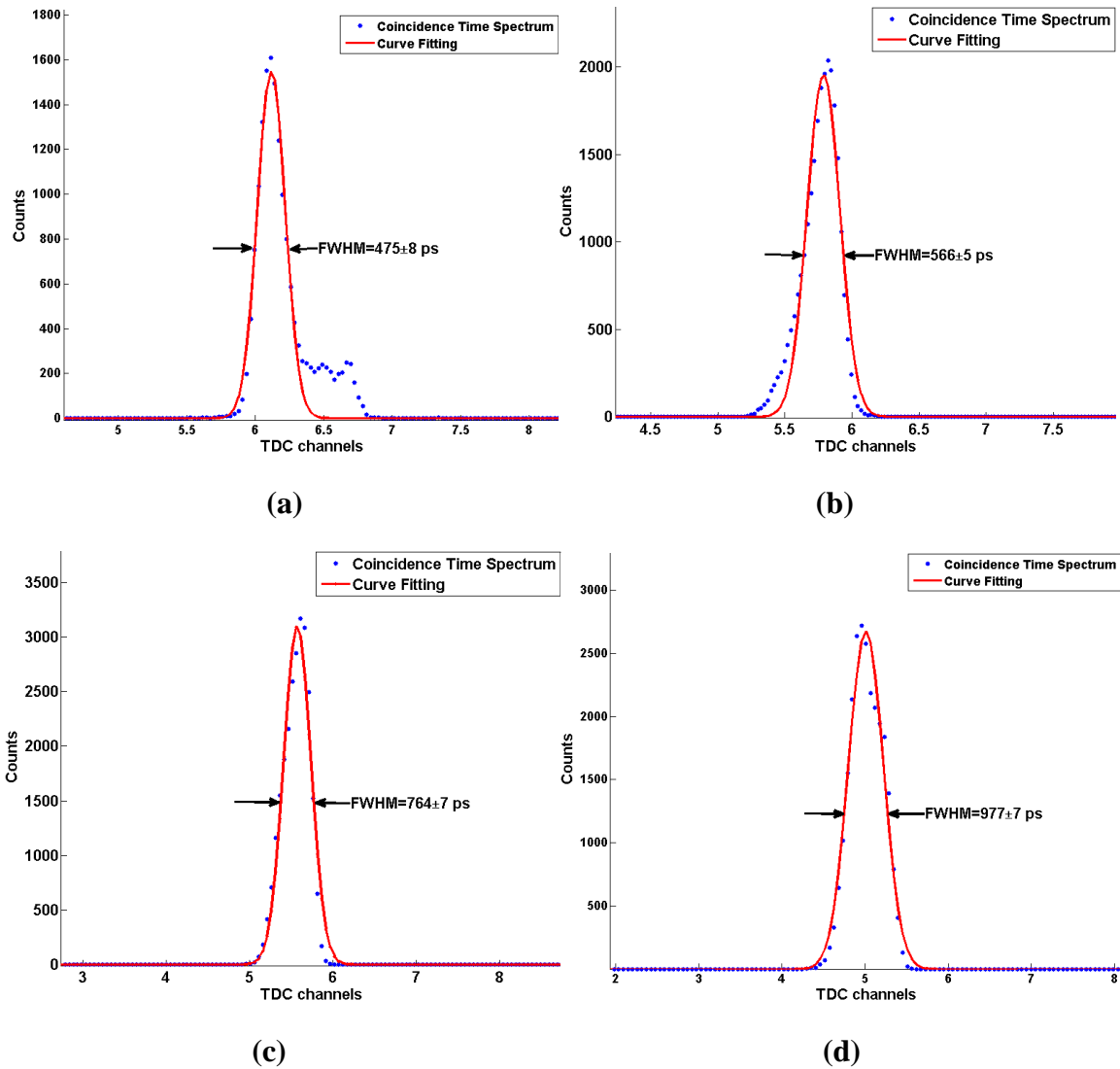


Figure 3.17: Coincidence timing spectra of the “S/N 108341” crystal by CFD method for different D_s settings: (a)1; (b)4; (c)7; and (d) 32. The attenuation factor, f , and DP were set as 0.18 and 4, respectively.

3.4.3 Results of crystals with different surface-reflector conditions

3.4.3.1 Energy Resolution

All 3x3x20mm³ LYSO crystals (Table 3.1) were tested, and measured energy resolutions are listed and summarized in Table 3.2. For energy resolution measurements, each crystal was removed, replaced and measured three times for replacement consideration, and the average energy resolution of these three measurements was obtained. The global energy resolution of each surface-reflector combination was obtained by averaging all energy resolutions of crystals having the same configurations. The variations between each individual crystal involve uncertainties of replacement and variations between crystal samples.

Table 3.2: Measured energy resolutions of 3x3x20 mm³ LYSO crystals with different surface-reflector combinations. To evaluate the error bars and eliminate human factors, each crystal was measured three times with repeated replacement. The average energy resolution of each surface-reflector combination was the mean value of individual crystal samples, and the uncertainty in average energy resolution was standard deviation of all corresponded samples.

PolishESR		PolishTeflon	
Samples	Energy Resolution (%)	Samples	Energy Resolution (%)
S/N 108333	10.4±0.3	S/N 108337	11.2±0.5
S/N 108334	10.5±0.4	S/N 108338	9.3±0.4
S/N 108335	11.0±0.2	S/N 108339	10.9±0.2
S/N 108336	N/A	S/N 108340	9.5±0.6
Average	10.6±0.4	Average	10.2±0.9
AsCutESR		AsCutTeflon	
Samples	Energy Resolution (%)	Samples	Energy Resolution (%)
S/N 108341	11.1±0.4	S/N 108345	16.0±0.6
S/N 108342	11.3±2.9	S/N 108346	N/A
S/N 108343	N/A	S/N 108347	15.1±0.5
S/N 108344	12.5±0.1	S/N 108348	14.4±0.1
Average	11.6±0.7	Average	15.2±0.8

3.4.3.2 Coincidence Timing Resolution

An example of time spectra using CFD (refer to Figure 3.6), linear & exponential rise-time fitting (refer to Figure 3.7) methods are shown in Figure 3.18. The coincidence timing resolutions are associated with the FWHMs of such spectra.

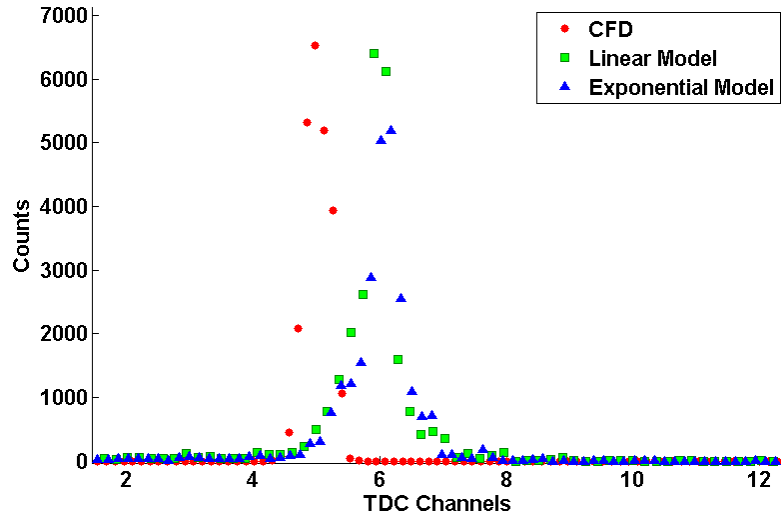


Figure 3.18: The time spectra for CFD, linear & exponential methods. The peak offset between CFD and other methods arises from delay in CFD algorithm with $f=0.18$, $D_p=4$, and $D_s=32$.

Table 3.3 lists the energy gated coincidence timing resolutions of $3 \times 3 \times 20$ mm³ LYSO crystals with four surface-reflector combinations by CFD, linear and exponential rising edge fitting time pick-off methods, respectively.

The timing resolution results as a function of different surface-reflector combinations as listed in Table 3.3 are plotted and summarized in Figure 3.19. The CFD method is significantly superior than the linear and exponential fitting methods in terms of smaller error bars, better absolute coincidence timing resolutions and faster processing time. For example the mean timing resolution of the AsCutTeflon configuration is 1.242 ± 0.104 ns for the CFD method, whereas larger values of the timing resolutions results are obtained: 1.776 ± 0.397 ns and 2.033 ± 0.141 ns for linear and exponential fitting methods, respectively. The step of finding the fitting point (“A” and “B” in Figure 3.7) of each signal pulse for the linear & exponential fitting methods makes the time required for these fitting time pick-off methods were 80 to 100 times longer than the CFD method. Moreover, the coincidence timing resolutions are significantly affected by accuracy of selecting such fitting points, which results in relatively large error bars as shown in Figure 3.19.

Table 3.3: Coincidence timing resolution results for 3x3x20 mm³ LYSO crystals by CFD, linear and exponential rising edge fitting time pick-off methods. The uncertainty of each crystal arises from fitting process. The average timing resolution of each surface-reflector combination was the mean value of individual crystal samples, and the uncertainty in average timing resolution was standard deviation of all corresponded samples.

PolishESR	Coincidence Timing Resolution (ns)		
	CFD	Linear	Exponential
S/N108333	0.989±0.007	0.996±0.036	1.479±0.056
S/N108334	0.988±0.007	1.234±0.045	1.208±0.049
S/N108335	0.902±0.006	0.993±0.034	1.168±0.042
S/N108336	N/A		
Average	0.960±0.050	1.074±0.138	1.285±0.169
PolishTeflon	Coincidence Timing Resolution (ns)		
	CFD	Linear	Exponential
S/N108337	1.027±0.007	1.3264±0.0508	1.6438±0.0498
S/N108338	1.105±0.022	1.1046±0.0216	1.2552±0.0326
S/N108339	0.983±0.006	1.1648±0.0528	1.1014±0.0262
S/N108340	0.956±0.007	2.4822±0.0272	2.1639±0.0153
Average	1.018±0.065	1.5195±0.6486	1.5411±0.4738
AsCutESR	Coincidence Timing Resolution (ns)		
	CFD	Linear	Exponential
S/N108341	0.977±0.007	1.527±0.048	1.324±0.048
S/N108342	1.007±0.006	1.432±0.070	1.452±0.056
S/N108343	1.068±0.007	2.032±0.014	2.058±0.029
S/N108344	1.009±0.006	1.735±0.020	2.206±0.516
Average	1.016±0.038	1.682±0.266	1.760±0.437
AsCutTeflon	Coincidence Timing Resolution (ns)		
	CFD	Linear	Exponential
S/N108345	1.280±0.008	1.792±0.073	2.032±0.092
S/N108346	1.226±0.008	1.271±0.053	1.964±0.073
S/N108347	1.355±0.009	1.797±0.072	1.906±0.071
S/N108348	1.107±0.007	2.242±0.021	2.229±0.020
Average	1.242±0.104	1.776±0.397	2.033±0.141

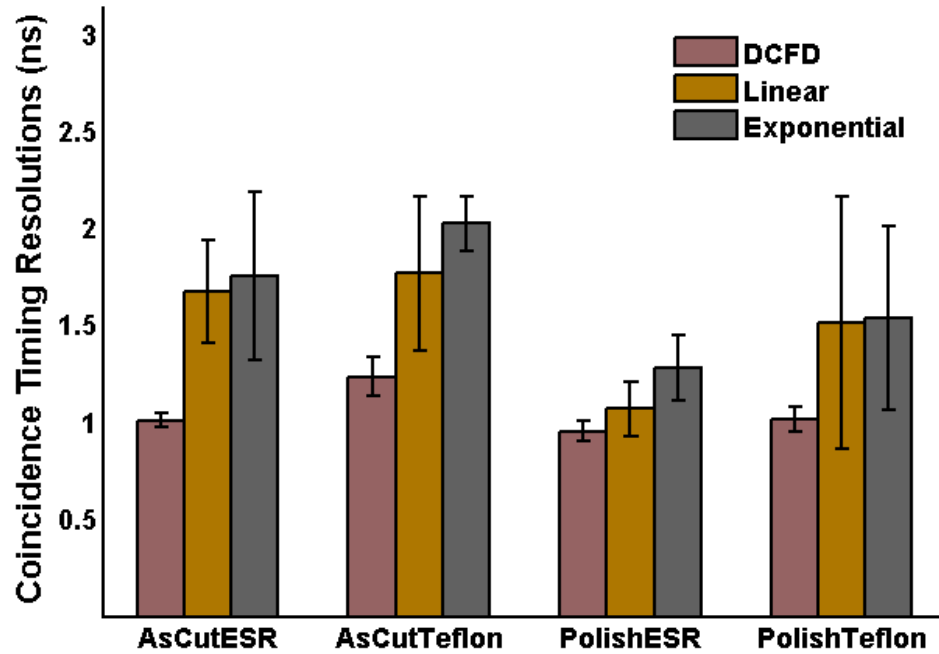


Figure 3.19: Coincidence timing resolutions as a function of various surface-reflector combinations for three time pick-off methods. The error bars are standard deviations of average coincidence timing resolutions in Table 3.3.

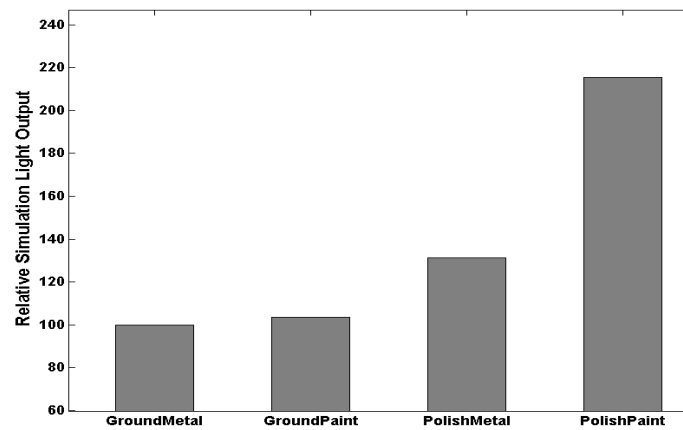
Chapter 4

Discussion and Conclusion

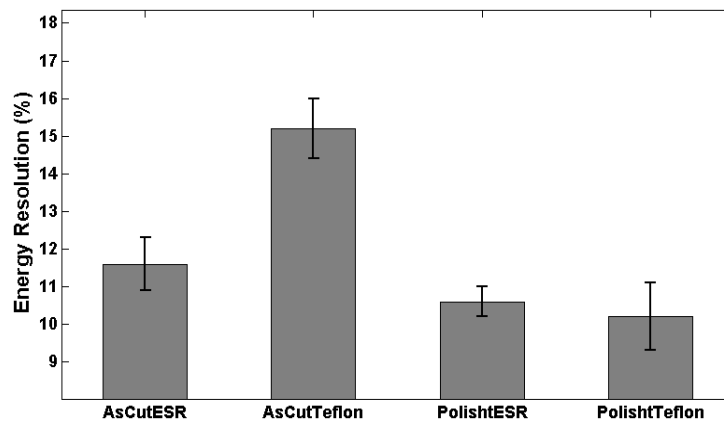
In this chapter, the comparison is made between the simulation results in chapter 2 and experimental results in chapter 3, including two parameters: energy resolution and time resolution. This would guide us to select the optimum crystal surface treatment and reflector configuration for PET detector design. The outlook of future works are summarized and discussed.

4.1 Energy Resolution

The simulation light output results and measured energy resolutions are summarized in Figure 4.1. The defined terminologies used in simulation and experiment for describing the surface treatment combinations are listed in Table 4.1.



(a)



(b)

Figure 4.1: Simulation light output (a) and measured energy resolutions (b) of four different surface-reflector combinations for $3 \times 3 \times 20 \text{ mm}^3$ LYSO scintillation crystals. For simulation, the results of all surface treatments are relative to that of AsCutESR. The error bars in (b) are standard deviations of average energy resolutions in Table 3.2. To show difference among data sets, the vertical axes of both (a) and (b) start at non-zero points.

Table 4.1: The terminologies of surface treatment combinations used in experiment and simulation. The definition of surface-reflector combinations for simulation is defined in Table 2.2.

Case	Simulation	Experiment	Crystal surface treatment	Reflector
1	GroundMetal	AsCutESR	Lambertian	Specular
2	GroundPaint	AsCutTeflon	Lambertian	Lambertian
3	PolishMetal	PolishESR	Specular	Specular
4	PolishPaint	PolishTeflon	Specular	Lambertian

For all four cases, the measured energy resolutions are in the range of $\sim 10\%$ to $\sim 15\%$, which are in good agreement with published literatures [Ludziejewski *et al* 1995, Melcher and Schweitzer 1992, Pepin *et al* 2004, Peng *et al* 2011, Surti and Karp 2007]. Though of LSO crystals, $\sim 7\text{-}8\%$ of energy resolutions are claimed by some groups [Kapusta *et al* 2000]), this might be due to a Cs-137 source where the energy peak is at 662 keV was used. The case of AsCutTeflon (GroundPaint) exhibits the worst energy resolution of $\sim 15\%$ energy resolutions. Note that these results are comparable to those results obtained with PMTs [Ludziejewski *et al* 1995, Melcher and Schweitzer 1992] due to several advantages of SiPM such as high gain. Moreover, higher SiPM bias voltage will give rise to higher gain on the SiPM and would thus result in better energy resolutions according to (Eq. 1.9) [Pichler *et al* 1999].

As discussed in chapter 2, the light output is inversely proportional to energy resolutions, following Poisson statistics. For instance, a larger light out would result in a better energy resolution. Since measuring absolute light output is a challenging task which would require calibration of peak positions with single photoelectron peak [Huber *et al* 1999, Kuntner *et al* 2002], only the relative light output is studied in our study. The case of PolishPaint (PolishTeflon) achieves largest light output in the simulation (215.51) and the best energy resolution in experiments ($10.2 \pm 0.9\%$). This is in consistence with previous findings that the polish surface is able to provide more light photons to be detected by photodetectors [Heinrichs *et al* 2002]. The standard deviations between crystal samples arise from random and systematic errors such as difference among individual crystals due to different growth processes, and/or human factors in experiment measurements including positional inaccuracies when placing crystals on the detector. Better design of experiment apparatus, methods and stabilization of experiment platform

are required to reduce the influence of standard deviation on validation comparison. During the data collection, the crystal might shift and be tilted off of the initial position due to gravity, unstable SiPM settings and amount of optical grease. The dimension of cross-section area of testing crystals were $3 \times 3 \text{ mm}^2$ which was exactly the same size as the active area of SiPM, therefore part of crystals could be easily shifted out to the SiPM's active area leading to inaccuracy measurements of energy resolutions.

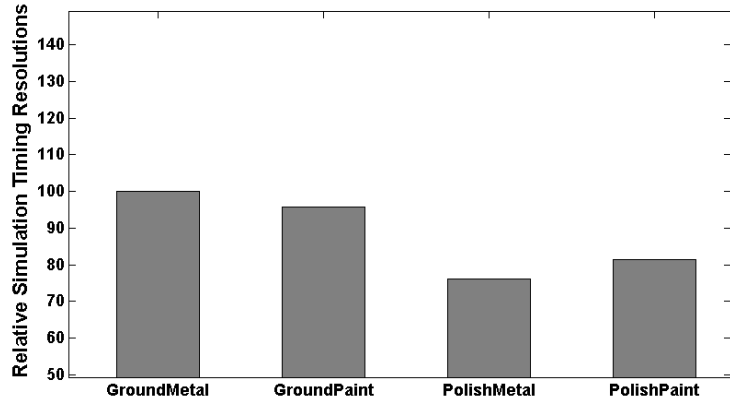
On the other hand, it is found that the two cases for rough surfaces (AsCutESR and AsCutTeflon) have worse energy resolution and lower light output. Due to the reflective properties of rough surfaces, the directions of reflected light photons are isotropic. As a result, when those photons travelling downward towards the photodetector hit a rough surface, they are likely to be reflected upward towards the top face of the crystal, leading to longer propagation time and more light absorption. The difference between two cases of polish surfaces (PolishTeflon and PolishESR) in Figure 4.1 (b) is not statistically significant as predicted in simulation ($10.6 \pm 0.4\%$ vs. $10.2 \pm 0.9\%$), implying that reflector selection might play a negligible role on light collection for polish surface treatments. Regarding why the PolishTeflon case has higher light output than the PolishESR case, we think it might due to the following reason. In our simulation, the optical photons will be scored once they hit the scoring face at the front face of a photodetector, where a certain amount of optic photons might be trapped due to the total internal reflection (i.e., mismatches of index of refraction), particularly at the crystal-detector interface. Such process has been described in Figure 2.22(a). The deployment of Teflon tape in this situation could improve the light output by breaking the total internal reflection simply due to the random direction angles taken by reflected light photons. Cherry *et al* 1995 has also claimed that the light output by using a crystal which has polish sides, ground top and is covered by a diffuse reflector is approximately twice higher than that by using a normal crystal which has polish sides and is covered a diffuse reflector. However, this improvement is not significant in their experiment results by comparing energy peak positions due to the imperfect polished crystal surface in practice. One explanation is that the rough surface in simulation was modeled as Lambertian reflection, where the directions of the reflected photons are most likely normal to the surface. For example in the side Lambertian reflection faces, most of the directions of reflected photons are normal to these surfaces, i.e. parallel to the bottom or top faces. Since the attenuation of high energy photons is characterized by the Beer's law, most of the optical photons are generated close to the top faces. Such optical photons might incident on the top face and penetrate to the diffuse reflector, where most likely these photons are downward reflected toward the bottom scoring face due to the characteristics of Lambertian reflection. However, in practice, the surface roughness is not completely following Lambertian

distribution. Therefore the difference between two types of reflectors in experiment is much smaller than that in simulation.

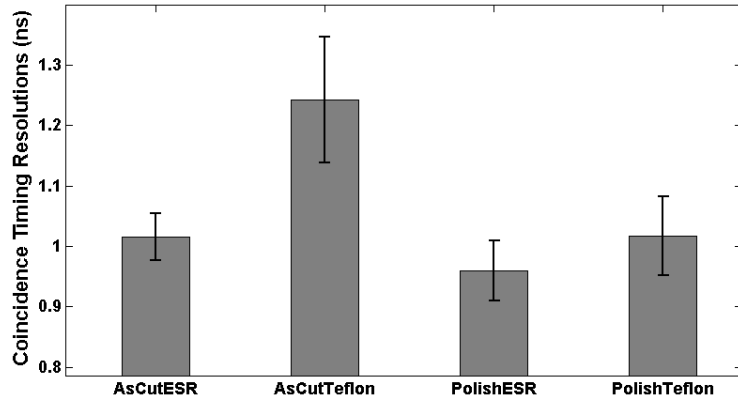
Note that, in simulation, the difference between case 1 (GroundMetal) and case 2 (GroundPaint) is not as great as that between case 3 (PolishMetal) and case 4 (PolishPaint). One explanation is that unlike the polished surface, the Ground crystal surface treatment itself breaks the total internal reflection and guides the reflected photons downward on the top surface regardless of the reflectors. In addition, the simulation testing result shows that there are only ~21% of the photons that incident on the top surface in Ground surface are refracted to the reflectors in comparison to the polished crystal surface treatment where this number is ~41%. Therefore the contribution of reflectors in Ground surface is much less than that in polished surface. A major discrepancy we found is between two cases with Ground surfaces (AsCut ESR and AsCutTeflon). Though no significant difference is found in simulation (100 vs 103.4), the measured energy resolution results are $11.6 \pm 0.7\%$ and $15.2 \pm 0.8\%$, respectively. One explanation is that the reflection coefficient of Teflon tape is much smaller than that of ESR in practice or less than the testing range (92% to 98.5%). Because the integration of calculating light output in simulation results was taken up to ~120 ns, the extremely longer path length information is not considered in simulation. For example most of the photons that are reflected by Teflon tape on side faces are most likely parallel to the scoring face results in longer propagation distance, or might be terminated if the path length is too long. In addition, if most of the light photons are reflected on crystal surfaces instead of refracting to reflectors (e.g. only ~21% of the photons that incident on the top surface in Ground surface are refracted to the reflectors as discussed before), the effect of reduction of photons by Teflon tape is not significant after multiple times of reflections. The discrepancy between rough surfaces (case 1 and 2) in experiment needs further investigation.

4.2 Coincidence Timing Resolution

The results of temporal response studies are summarized in Figure 4.2. In the simulation, we use the reciprocal of rise-time slopes as an indicator; while in the experiments, we measured energy gated coincidence timing resolutions against a fast PMT. Among three different timing pickoff methods, only the CFD method is selected for comparison as it obtains improved timing resolutions over the other two methods. For all the experimental results reported here, the parameters such as f , D_P and D_S used in the signal processing can be found in Chapter 3.4.3.2.



(a)



(b)

Figure 4.2: Coincidence timing resolutions of four different surface-reflector combinations for $3 \times 3 \times 20 \text{ mm}^3$ LYSO scintillation crystals for (a) simulation and (b) experiment with CFD time pick-off method. For simulation, the results of all surface treatments are relative to that of AsCutESR. The error bars in (b) are standard deviations of average coincidence resolutions in Table 3.3. To show difference among data sets, the vertical axes of both (a) and (b) start at non-zero points.

The measured coincidence timing resolutions among all four cases are in the range of 900ps to 1.3 ns. Superior coincidence timing resolution as lower than 400 ps for a $3 \times 3 \times 15 \text{ mm}^3$ coupled with a SiPM and a $2 \times 2 \times 10 \text{ mm}^3$ LSO crystal coupled with a PMT is available [Jarron et al. 2009]. Approximately 585 ps timing resolutions are achievable for the entire TOF-PET system provided by Gemini TF which consists of $4 \times 4 \times 22 \text{ mm}^3$ LYSO crystals with PMTs [Surti and Karp 2007]. A coincidence timing resolution of 886 ps (and 12% energy resolution) was reported for a $2 \times 2 \times 30 \text{ mm}^3$ LSO crystal using a CFD time pick-off method in a digital processing system using a pair of fast PMT at 1700 V rather than SiPM by [Labruyere *et al* 2007].

Refer to Figure 4.2, it is noticed that case 3 (PolishMetal) has the fastest rising edge (76.21) and case 1 (GroundMetal) has the slowest rising edge (100.0). In experimental results, the PolishESR obtains the best timing resolution (0.96 ± 0.05 ns) among all four cases as predicted in simulation. The simulation shows that Ground surface (case 1 and 2) results inferior timing resolution than Polish surface (case 3 and 4). Such pattern is also in good agreement with experiment results. One possible explanation is that when rough surfaces exist, light photons have a longer propagation time (due to Lambertian reflection) due to multiple reflections inside scintillation crystals.

Taking the case 3 (PolishESR) as an example, the light photons generated by a 511 keV annihilation ray emit isotropically and some of them are guided towards the detector's face due to the Specular reflections on side faces. In case 4 (PolishTeflon), though some photons are reflected on side faces and move towards the detector's face in the same way, a large portion of them will be refracted to the diffusion reflector, and then reflected back. Such process leads to a longer propagation time. In addition, the better timing resolution of the case 1 (AsCutESR) with respect to case 4 (AsCutTeflon) surface treatments is possibly because of its relatively higher light output (i.e. lower energy resolution Figure 4.1 (b)), i.e. lower contribution due to Poisson statistics.

Higher PMT operation voltage would provide better timing resolutions due to higher gain and faster electrons propagation speed, or shorter transit time in PMT (t_{CTT} in Eq. 1.14). Superior timing performance of PMT and SiPM with low TTS (in the order of 100 ps for typical SiPMs) is required to obtain high coincidence timing resolution [Jarron et al 2009]. The TTS of the PMT used in our experiment measurements is 270 ps. Hamamatsu reports that the achievable TTS of micro-channel photomultiplier, which is the new generation of PMT family, could be as low as 25 ps. To obtain good coincidence timing resolutions, faster ADC sampling rates are required as well. Better than 200 ps of coincidence timing resolution has been reported by using a pair of SiPMs, $3 \times 3 \times 5$ mm³ LYSO crystals and a 8GS/s ADC [Seifert *et al* 2009].

The coincidence timing resolution measurements rely on the detection system and experimental method, such as the instance time pick-off method. An ideal TOF-PET system is characterized by having high detection efficiency of 511 keV annihilation photons in the scintillation crystal and of optic photons in the photodetector (i.e. high quantum efficiency), instantaneous rise and decay times of intrinsic photon emission in scintillation processes and low TTS, and low aspect ratio that minimize path length of optical photons [Spanoudaki and Levin 2010]. Ideally, the first pair of arrival photoelectrons provides the best coincidence timing resolution so that the trigger levels have to be set as low as possible in order to avoid degrading timing performance by

mistakenly selecting the subsequent photoelectrons. Because of this, very precise timing pick-off methods and signal acquisition electronics are required to reduce the effect of noise and facilitate this narrow timing window. Traditionally, timing resolution has been measured using analogue data acquisition systems due to the associated theoretically infinite resolution, which is a large advantage over the discrete resolution of digital systems like the one used in this work.

4.3 Conclusion and Future Work

In conclusion, in this work, a Monte-Carlo simulation tool was developed to model light propagation inside scintillation crystals. Various configurations such as surface treatments and reflectors have been characterized in order to optimize energy and coincidence timing resolutions, two critical parameters of a PET detector. Based on the simulation and experimental results, the polished surface treatment, used together with an external specular reflector, is able to provide the best energy resolution and timing resolution for a LYSO ($3 \times 3 \times 20 \text{ mm}^3$) and SiPM assembly we tested. The AsCut surface with external diffusion reflector is not desired due to its inferior energy and timing resolutions. Despite good agreement found between simulation and experiments for three cases, a major discrepancy is found for the case 2 (AsCut surface with external diffusion reflector) and will be further examined. In addition, improvements need to be made regarding surface models, wavelength dependency, timing pickoff.

4.3.1 Outlook for Simulation

In order to improve the accurate of simulation, a set of optical properties for scintillator materials will be determined and added in the simulation. One critical issue is how to obtain more accurate values for interaction (i.e., attenuation), scattering and absorption lengths (i.e., mean free path) by experiment, which is a very challenging task. The interaction length in our study was assumed to be 138mm, equal to the scattering length of 138mm published in [Moisan *et al* 1996, van der Laan *et al* 2010]. To date, different values have been used in different literatures, for example, [Ros *et al* 2008] uses 1000 mm as scattering length, and [Rothfuss *et al* 2004] uses 256 mm as the scattering length. A very recent study focused on measuring these parameters based on the direct measurement of the scattered power [Steinbach *et al* 2011]. Additionally, the type of scattering of optical photons within the scintillation crystal has to be determined. In comparison to the presumed isotropic direction of scattered photons, other types of

scattering are also available in other simulation studies such as Rayleigh scattering [Bonifacio *et al* 2010].

It is important to realize that the emission of scintillation light photons in crystals is wavelength dependent (~ 380 nm to 650 nm for LYSO, peak at 420 nm). This would further complex the modeling process by taking into account of several wavelength-dependent processes, such as reflection and transmission on crystal surfaces in terms of index of refraction [Bonifacio *et al* 2010, Motta and Schönert 2005], quantum efficiency of photodetectors, the generation of optical photons due to luminescence, linear attenuation coefficients of incoming 511 keV annihilation rays, and re-emitting of absorbed optical photons with longer wavelength.

Another improvement to be made is to introduce more advanced mathematical model for surface roughness. In our simulation, the surfaces are grouped into two groups: Polish and Ground, which are covered with specular and Lambertian reflections, respectively. However, the type of reflections on a random roughness surface can be treated as a combination of specular reflections and Lambertian reflections (Figure 2.8(a)). The challenge exists that what weight needs to be assign to specular and Lambertian, respectively. In addition, [Janecek and Moses 2008] studied intensity as a function of angular distribution of reflected light photons for a Lambertian surface. The results show that the Lambertian reflection model failed to predict the direction of reflected lights when the incident angle was less than 50° . DETECT2000 addressed this problem by introducing a surface model “unified”, as a combination of specular and Lambertian reflection and adjustable weight [Moisan *et al* 1996, Moisan *et al* 1997, van der Laan *et al* 2010]. However, more unknown parameters are introduced such as constants that control the relative weights of specular diffusion and backscatter reflections such that more experimental measurements and assumptions are desired to determine these input parameters [Moisan *et al* 1996, Moisan *et al* 1997, van der Laan *et al* 2010]. Another solution to improve accuracy of predicting reflections in the simulation on random roughness surfaces is to incorporate a Look-Up Table, which contains mathematical corrected angular distribution of reflected light by experiment measurement [Janecek and Moses 2010].

Minor updates can be added to our simulation such as: modifying the simulation code to have the option of generating the spatial distribution of detected optical photons on the scoring face which would help for investigating the spatial distribution of block detector design [Vandenbroucke and Levin 2008], and extending the light transportation simulation code to a more general PET dedicated toolkit. This could be done by integrating our simulation with simulation software that examines annihilation ray

interactions in detector such as the GATE in order to further simulate electronics processes in the photodetector [Liu et al 2009, Moses and Ullisch 2006]. Moreover, our simulation toolkit is able to incorporate to DOI investigation since the optical photons can be generated in different desired crystal layers.

4.3.2 Outlook for Experiment

The simulation model would be further validated with additional geometries, for instance trapezoidal geometry is one such of design of a PET scintillation crystal [Chung *et al* 2011]. Energy resolutions and timing resolutions as a function of dimensions for various surface-reflector combinations can be measured and investigated, for instance instead of all five reflection surfaces, the surface treatment and/or type of reflector of one reflection surface could be different to the remaining surfaces, which might lead to different energy and timing results.

In addition, [Spanoudaki and Levin 2011] shows interesting results that a polished surface has higher light output and better timing resolution than AsCut surfaces for longer crystals, but has lower light output and worse timing resolution than AsCut for shorter crystal. [Barton *et al* 2007, Huber *et al* 1999] concludes that light output decreases with longer crystals hence it will be useful to work on crystal dimension validations of our simulation. At the time of writing, $1 \times 1 \times 15 \text{ mm}^3$ crystal samples are available in the lab and are ready to be tested. Quantization of absolute values of light output of scintillation crystals is another interesting potential future work. This would allow direct comparison of light output among different surface treatments rather than indirectly comparing energy resolutions [Huber *et al* 1999].

Recently, novel designs of crystal blocks of DOI capability are actively being studied by many research groups [Eriksson *et al* 2010, Saoudi *et al* 1999, Saoudi *et al* 2000]. Our group aims to investigate DOI effects in scintillation crystals by utilizing light propagation information. Our light tight box and collimator (please see Appendix D for details) was designed with DOI experiment capability in mind and is able to change the crystal position with sub-millimeter resolution. Furthermore, it would also be interesting to test different crystal materials such as LaBr_3 , which has excellent energy resolution, light output, and fast timing performance [Witherspoon *et al* 2008, Witherspoon *et al* 2010]. However, the downside of its low density and especially its hygroscopic property makes LaBr_3 technically challenging to work with. At the time of writing, LaBr_3 crystals are being investigated in our group.

Appendix A

Investigation of SNR benefit for a time-of-flight (TOF) PET

The goal of this work is to study the benefit of a TOF PET, which will help us optimize detector design and surface treatment as described in section 1.4.2.

In conventional PET image reconstruction, the annihilation position is based on a line-of-response (LOR) while the exact location along the line is unknown. For a projection, image pixels along a LOR are assigned an equal intensity given which results in noise propagation from all pixels. For a TOF PET (due to the superior time resolution as discussed in 1.4.2), the annihilation position can be confined to a smaller region along the LOR, instead of the full line. Such process is illustrated in Figure. Although such confinement is not sufficient to improve spatial resolution, it is able to improve image SNR. For this work, a simplified simulation was performed to study the SNR improvement and some preliminary results are reported.

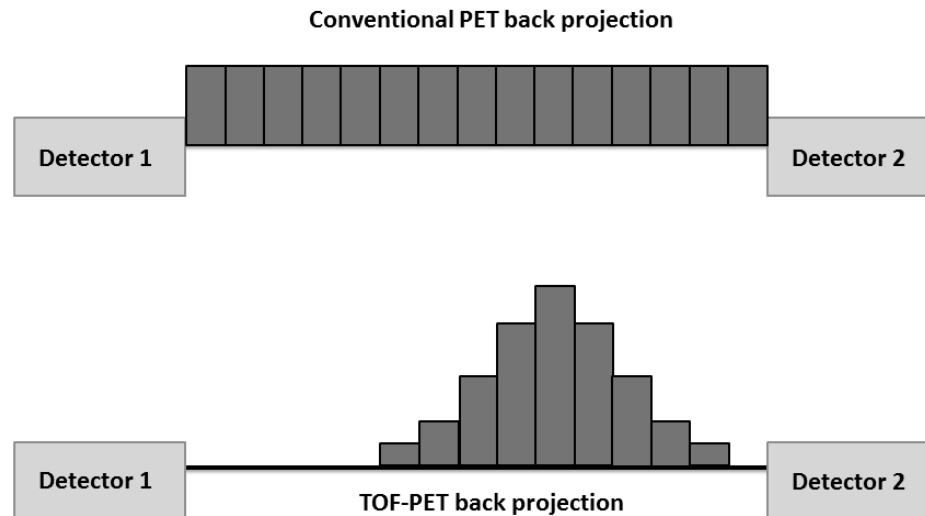


Figure A.1: Reconstruction methods for conventional (top) and TOF (bottom) PET. No information about the location of the annihilation event along the LOR is provided for conventional method. The probability distribution of annihilation position is calculated by difference in measured arrival times for TOF-PET.

A.1 Methods

The simulation was implemented in MATLAB. A Shepp-Logan phantom [Bones *et al.* 2007] with size of 80 x 80 pixels was simulated and used for both reconstruction methods

(Figure A.2). Rectangular ROIs were chosen for both lesion (region “B”, within range of Shepp-Logan phantom) and background noise (region “A”). The contrast ratio of the ROI “A” to the ROI “B” was set as 5:1. For each pixel the noise, which is the square root of the count of that pixel, was artificially introduced. The SNRs were calculated based on the mean of ROI “B” and standard deviation of “A”.

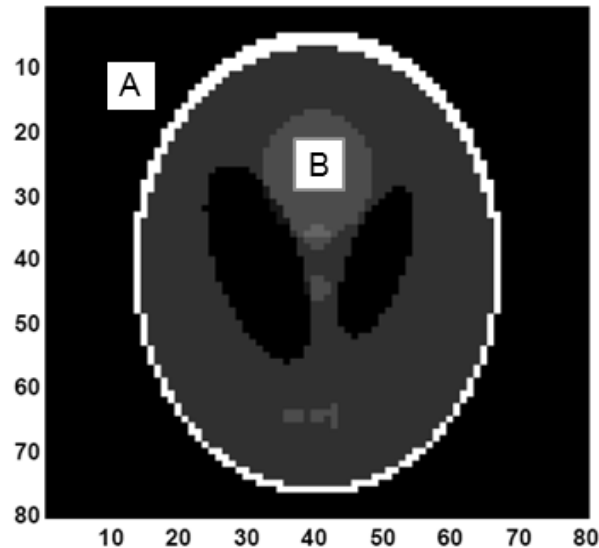


Figure A.2: Simulated Shepp-Logan phantom in MATLAB with definition of ROIs of background (A) and lesion (B)

A.1.1 Conventional PET

Back-projection can be explained as follows: as shown in Figure A.3 (a), for the first projection angle all of the counts from each pixel was added together and saved as a 1D profile, which is subsequently uniformly back projected onto all the pixels (Figure A.3 (b)); the above procedures were repeated for a new projection angle and eventually the image of original object will be obtained (Figure A.3 (c)-(g)). Note that instead of the above procedures, one could also simply use “radon” (forward projection) and “iradon” (back-projection) commands in MATLAB to reconstruct the image.

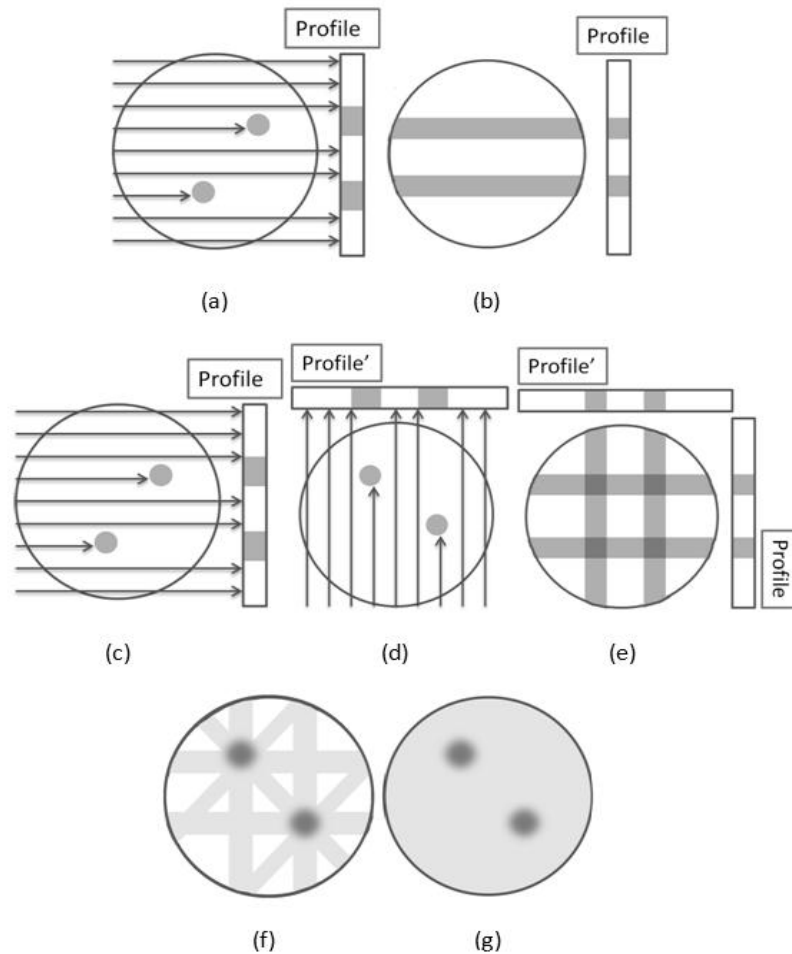


Figure A.3: The principle of back-projection. The reconstructed image for the back-projection method is blurred by $1/r$ blurring effect which could be solved by applying a high-pass filter to suppress low spatial frequencies and increase sharpness. The figure is reproduced based on [Pogue 2012].

A.1.2 TOF PET

The annihilation position can be estimated based on the TOF-PET equation Eq. (1.21) so that only the statistical fluctuations from those pixels which are close to the event position are introduced. In comparison to the methods in conventional PET mentioned above, for TOF PET, a different image reconstruction method was used. For the first projection angle the intensity (or counts) from one pixel (“center” pixel in Figure A.4) was extracted and redistributed to the “center” pixel and adjacent “kernel” pixels (those pixels equally locate at both sides of the “center” pixel, “offset” in Figure A.4) according to size and shape of the kernel, which are to be discussed later. Such a procedure was repeated for the next projection angle until the full 360 degrees had been processed. In the

last step, the above procedures were repeated to the next “center” pixel until all the image pixels were treated.

Size of Kernel

The size of the kernel is related to the position uncertainty, Δx . The size of phantom is 80x80 pixels since the diameter of the detector ring of a typical whole body PET is about 80 cm, hence we assumed one pixel is approximately 1 cm. Therefore the number of pixels directly reveals the size of the kernel which simulates the position uncertainty. Since in reality the Δx is determined by coincidence timing resolution, here we just calculate the corresponding timing resolution based on Eq. (1.21) with known Δx (i.e. size of kernel). For instance with the speed of light (2.25×10^8 m/s in water), if the size of kernel, n , has a value of 5 (i.e. two “kernel” pixels plus one “center” pixel) the Δx will be 5 cm and the calculated Δt will be 222 ps. The coincidence timing window is able to be set to a few nanoseconds (typical conventional PET) to hundreds of picoseconds (TOF-PET) so that four Δx were tested (Table A.1).

Table A.1: Size of kernels in terms of pixel numbers and calculated timing resolutions.

n	3	5	7	9
Δt (ps)	133	222	311	400

Shape of Kernel

Two kernel shapes, which determine how those intensities from “center” pixels would be redistributed, were applied: rectangular and Gaussian. The rectangular shape (Figure A.4 (a)) is simply the intensity divided by kernel size, whereas the redistribution of intensity for Gaussian shape (Figure A.4 (b)) is based on Gaussian function.

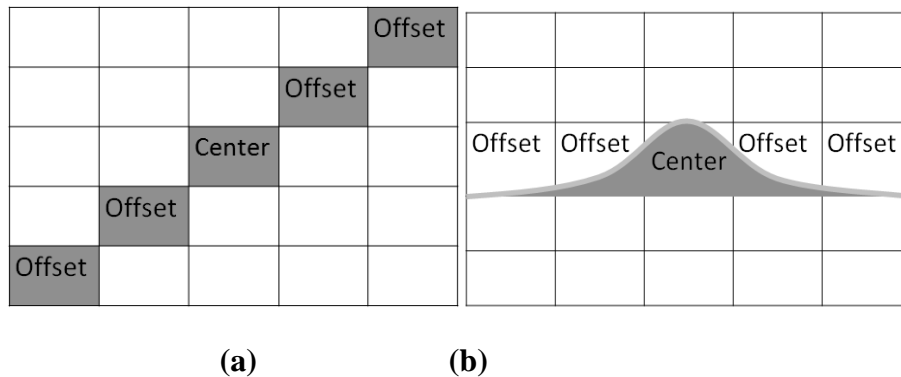


Figure A.4: Examples of TOF-PET image reconstruction method for kernel size of $n=5$ and kernel shape of (a) rectangular and (b) Gaussian.

A.2 Results and discussions

Figure A.5 shows the reconstructed images using the TOF PET with different kernel sizes, which indicate that TOF-PET helps improve image quality.

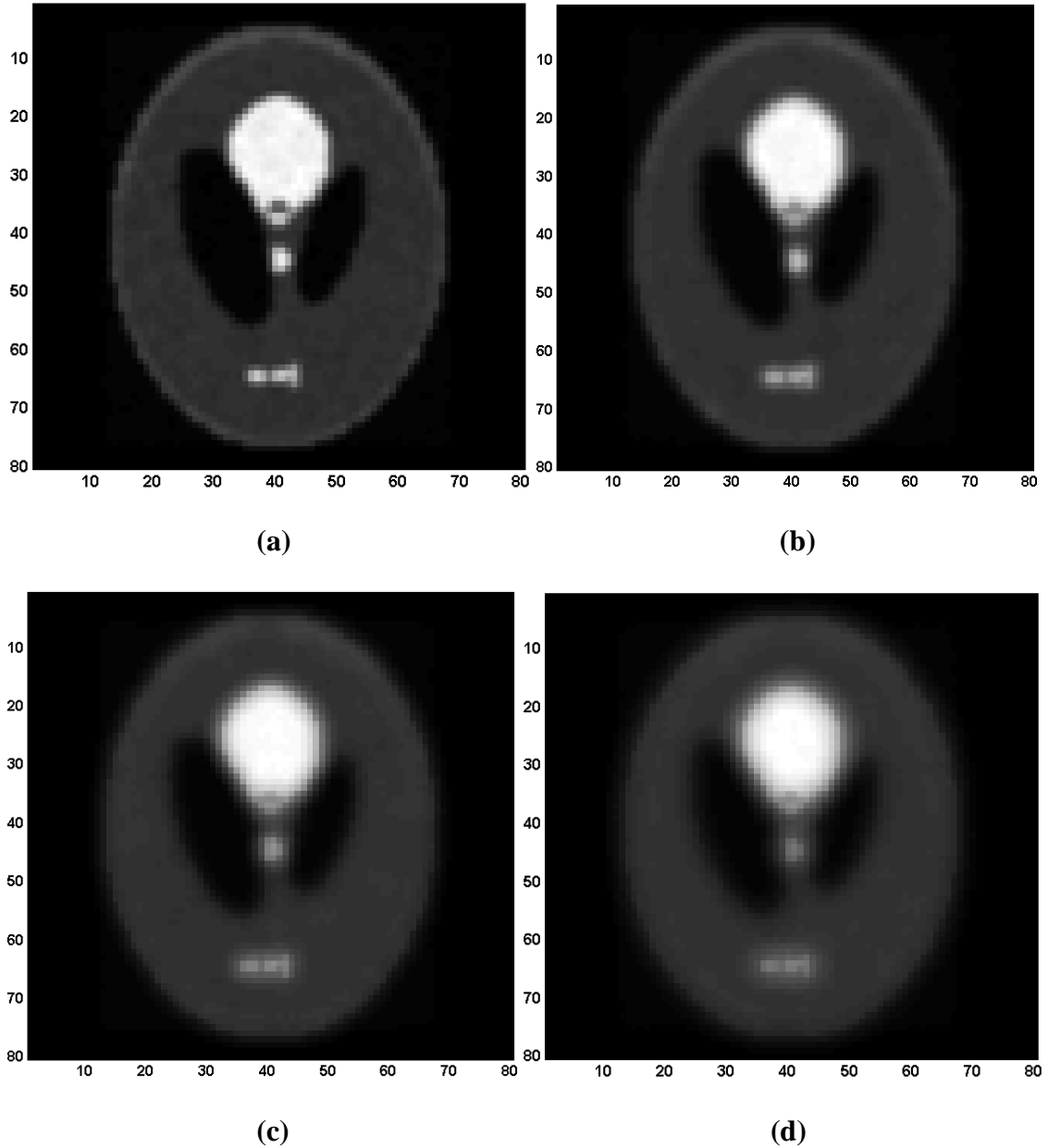


Figure A.5: The reconstructed images by TOF-PET reconstruction method with rectangular kernel shape and kernel sizes of (a) 133ps (b) 222ps (c) 311ps (d) 400ps. Only the images with rectangular kernel shape are shown here since they are similar to the reconstructed images with Gaussian kernel shape by direct view.

The calculated SNR results are listed in Table A.2, which corresponds to the ratio of SNR between a TOF PET and a conventional PET. As predicted by the analytical framework in Eq. (1.22), the SNR improvement is inversely proportional to the time kernel (i.e., better time resolution from detectors). In addition, Gaussian kernels consistently achieve a higher extent of improvement over the rectangular kernels.

Table A.2: Comparison between theoretical SNR gain and simulated relative SNR results by TOF-PET image reconstruction method. The theoretical SNR gain is calculated by Eq. (1.22).

Δt (ps)	Theoretical Gain	TOF Gaussian Gain	TOF Rectangular Gain
133	5.16	21.63	13.11
222	4.00	9.17	9.00
311	3.38	3.36	3.83
400	2.98	2.51	2.63

Good agreement is observed between the simulated results and those from the analytical method for 400 ps and 311 ps, which correspond to the current time resolution limit achievable with a LSO and SiPM used in the thesis work. However, no agreement is found for the cases of 222 ps and 133 ps. Despite the simulation being performed using a simplified phantom and a “virtual” back-projection method, we would like to point out that the analytical framework is also associated with two limitations, such as homogeneous tissue and missing image reconstruction step. In the future, a more complicated simulation based on a realistic whole body phantom and a full image reconstruction needs to be conducted to study such discrepancy.

Appendix B

Probability density functions for different sampled variables

Sampling isotropic direction

The PDF of an isotropic distribution is invariant under rotations in a coordinate system. In the spherical coordinate system, the differential solid angle is expressed as follows:

$$d\Omega = \sin\theta d\theta d\varphi \quad (\text{B.1})$$

From the above expression we notice that φ is uniformly distributed, but θ is not. The PDF of θ and φ are sampled separately. The PDF of θ and φ after normalization is:

$$\begin{cases} \text{pdf}(\theta) = \frac{\sin\theta}{2} \\ \text{pdf}(\varphi) = \frac{1}{2\pi} \end{cases} \quad (\text{B.2})$$

And according to Eq. (2.5), the CDF of θ is associated with a random number, xr as follows:

$$\text{cdf}(\theta) = \int_0^\theta \frac{\sin\theta}{2} d\theta = -\frac{1}{2}(\cos\theta - 1) = xr \quad (\text{B.3})$$

thus,

$$\cos\theta = 1 - 2xr = 2xr - 1 \quad (\text{B.4})$$

Now $\sin\theta$, $\cos\theta$ are linked with random numbers. With the same manner the CDF of φ is associated with a different random number, xr' as follows:

$$\varphi = 2\pi \cdot xr' \quad (\text{B.5})$$

Sampling photon initial launch positions

Again, the initial position of an initialized optical photon is expressed in X, Y, Z components. The X and Y components are relatively more easily sampled due to their uniform distribution in the x and y directions:

$$\begin{cases} X = (xr - 0.5) \cdot W_x \\ Y = (xr - 0.5) \cdot W_y \end{cases} \quad (\text{B.6})$$

However, positions of generated optical photons along the z-direction follow an exponential distribution due to the attenuation of annihilation photons which is mathematically expressed by the Beer-Lambert law (Eq. 1.2). Therefore the PDF of z after normalization according to Figure 2.6 (a) is:

$$\text{pdf}(z) = \frac{\mu}{1 - e^{-\mu L}} e^{-\mu(L-z)} \quad (\text{B.7})$$

And the CDF of z is associated with a random number, xr as follows:

$$Z = \frac{\ln[1 + (e^{\mu h} - 1) \cdot xr]}{\mu} \quad (\text{B.8})$$

Sampling Lambertian distribution

In a spherical coordinate system, the PDF of a Lambertian cosine distribution incorporates an isotropic distribution which gives a modified differential solid angle from:

$$d\Omega' = \sin\theta \cos\theta d\theta d\varphi \quad (\text{B.9})$$

And after normalization, the PDF of θ is:

$$\text{pdf}(\theta) = 2\sin\theta \cos\theta = \sin 2\theta \quad (\text{B.10})$$

Note that the PDF of φ is also $\frac{1}{2\pi}$. The conventional way [Shirazi *et al.* 1998] to express sampling variable θ as a function of random number, xr, by the inverse distribution method is to obtain the CDF by integrating PDF:

$$\text{cdf}(\theta) = \int_0^\theta \sin 2\theta d\theta = -\frac{1}{2}(\cos 2\theta - 1) = xr \quad (\text{B.11})$$

Where θ is $[0, \frac{\pi}{2}]$ since 2θ is $[0, \pi]$. Thus, rearranging the above equation:

$$\cos \theta = \cos \left[\frac{1}{2} \cos^{-1}(1 - 2 \cdot xr) \right] \quad (\text{B.12})$$

The above expression for a Lambertian distribution is more complex than that of an isotropic distribution. As mentioned before, Pascal does not include inverse trigonometric functions. Alternatively a method of integration to obtain the CDF is used by assuming a new variable, x which is equal to $\cos\theta$ and is in range of 0 to 1. Thus:

$$xdx = -\sin\theta\cos\theta d\theta \quad (\text{B.13})$$

So, after normalization, the PDF of x is $2x$, and the CDF of x is associated with a random number, xr as follows:

$$\text{cdf}(x) = \text{cdf}(\cos\theta) = \int_0^{\cos\theta} 2xdx = xr \quad (\text{B.14})$$

Finally, the Lambertian cosine distribution is associated with a random number as:

$$\cos\theta = \sqrt{xr} \quad (\text{B.15})$$

The above expression is much simpler than the equation from [Shirazi *et al.* 1998] and is implementable in Pascal since no inverse trigonometric function appears.

However, as mentioned, the rejection method was used to sample Lambertian distribution rather than the above two inverse distribution methods although these two methods are used to verify our rejection method. Figure B.2 shows that all these three methods follow cosine distribution and are consistent with each other. Note that due to lack of inverse trigonometric function in Free Pascal library, the inverse cosine function was expressed and calculated in forms of Taylor infinite series expansions.

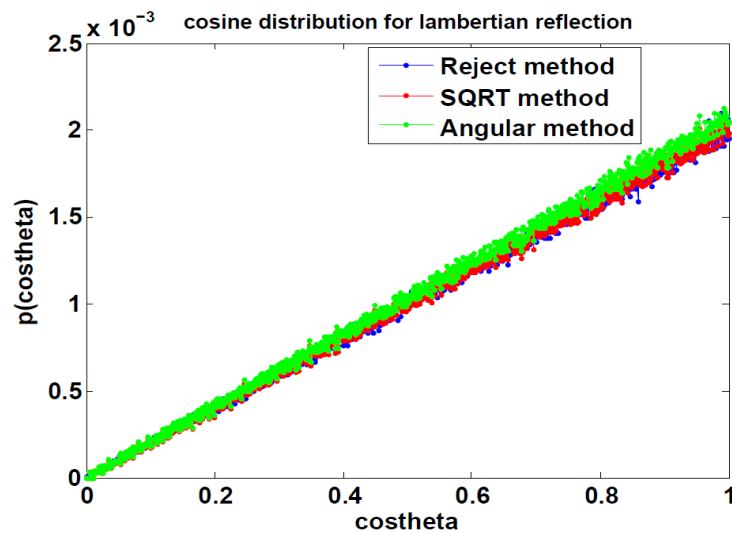


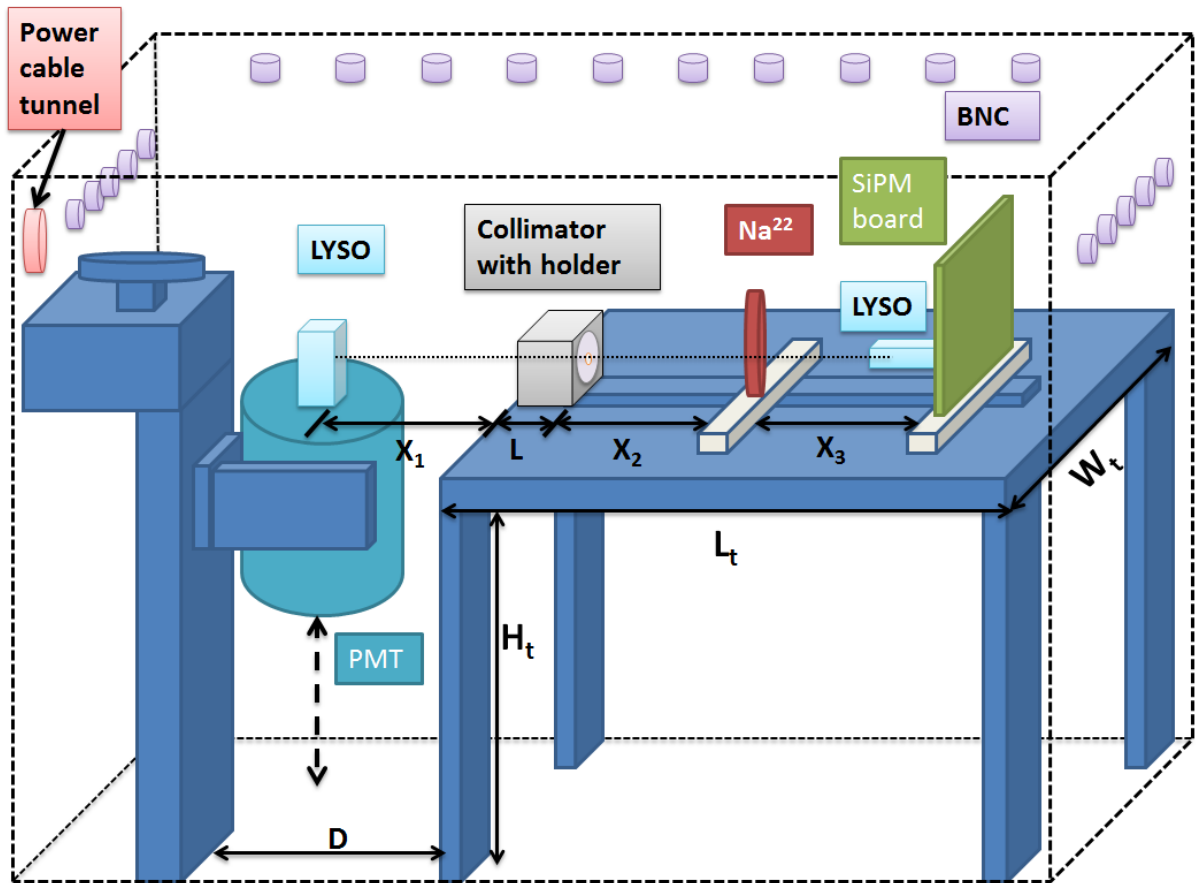
Figure B.1: Simulation verification results for comparing three Lambertian distribution sampling methods.

Appendix C

Design of light tight box and collimator

C.1 Light tight box

To perform the experiments outlined in Chapter 3, a light tight box is designed and developed, as shown in Figure C.1. It enables us to measure energy resolution, coincidence timing resolution, and DOI resolution. The box was constructed in the McMaster Machine Shop and is shown in Figure C.2.



(a)

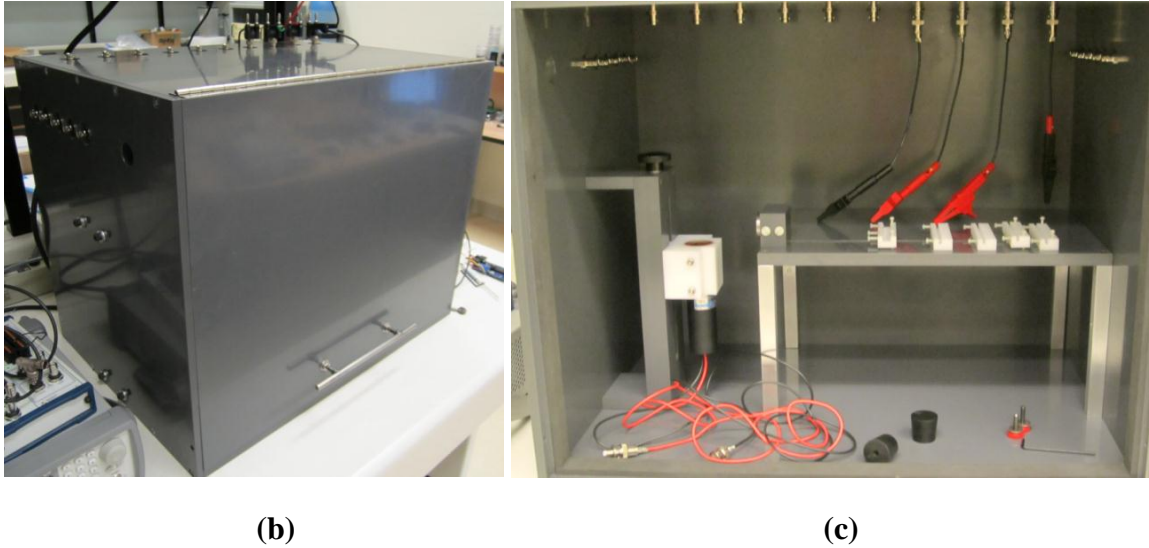


Figure C.1: The self-designed light tight box as the experiment platform. (a) Construction and components of designing the light tight box. Note that no collimator is required for coincidence timing measurements with non-monolithic crystals or for other non-coincidence experiments. (b) External view of the light tight box. The box can be opened at the front side; (c) internal components of light tight box with white Delrin holders and PMT in position. Note: 1. the PMT-collimator distance can be shortened by adding blocks on the back of the PMT apparatus bulk if necessary; 2. a tunnel was drilled for the high voltage power SHV cable of the PMT; 3. the collimator holder is removable for doing non-DOI coincidence experiments.

The box is made from polyvinyl chloride (PVC) and has a dimension of 235x354x166 in mm. Several holders made of Delrin were designed to hold circuit boards and radioactive sources, either horizontally or vertically. The distance between the source and the detector is adjustable. One critical feature of the design is that two of these holders are able to move vertically in order to accurately support scintillation crystals which are placed horizontally, which allows us to conduct energy and timing experiments. On the other hand, for DOI experiments to be done in the future, the PMT's holder (and collimator) is able to be vertically moved within an uncertainty less than 1 mm.

C.2 Collimator

Though no DOI measurement has been performed yet, a collimator has been successfully designed and made to allow future work. DOI experiment requires a collimated 511 keV beam from a sealed radioactive source to irradiate a crystal at different positions. In this section, a mathematical model was developed to optimize the collimator design, with regard to several parameters such as material, thickness, diameter, pin-hole and build-up factor.

C.2.1 Attenuation within collimators

As shown in Figure C.2, the collimator is located between a scintillation crystal and the point source. Inside the collimator, a pin-hole tunnel is the channel allowing annihilation photons pass through without attenuation.

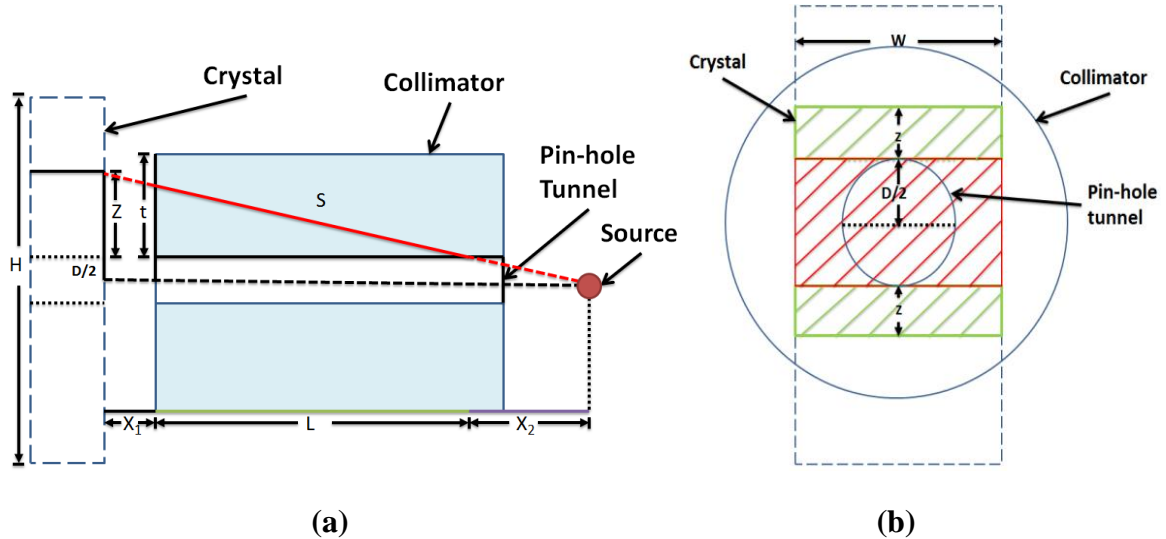


Figure C.2: (a) Configuration of collimator-crystal-source set; X_1 is the distance between the crystal and the existence edge of the collimator; and X_2 is the distance between the radioactive source and the entrance edge of the collimator; H , L and t are the height, length and thickness of crystal, respectively (b) cross-sectional view of crystal (rectangle) and collimator (circle). The red area is the region on crystal corresponding to size of pin-hole. The size of green region depends on scale of Z .

Ideally, only those annihilation photons within the tunnel will pass through the collimator, while those outside of the tunnel will be attenuated by the lead collimator. In practice, however, a portion of those annihilation photons emitted isotropically from the point source, would not interact with the collimator material but somewhere within tunnel. Note that the Z region includes an upper and a lower part such that if Z is equal to 0.5 mm, the effective undesired layers' height is 1 mm. Due to the symmetry of the configuration studied, only the upper part is shown and used to find the mathematical expression since both parts are symmetric.

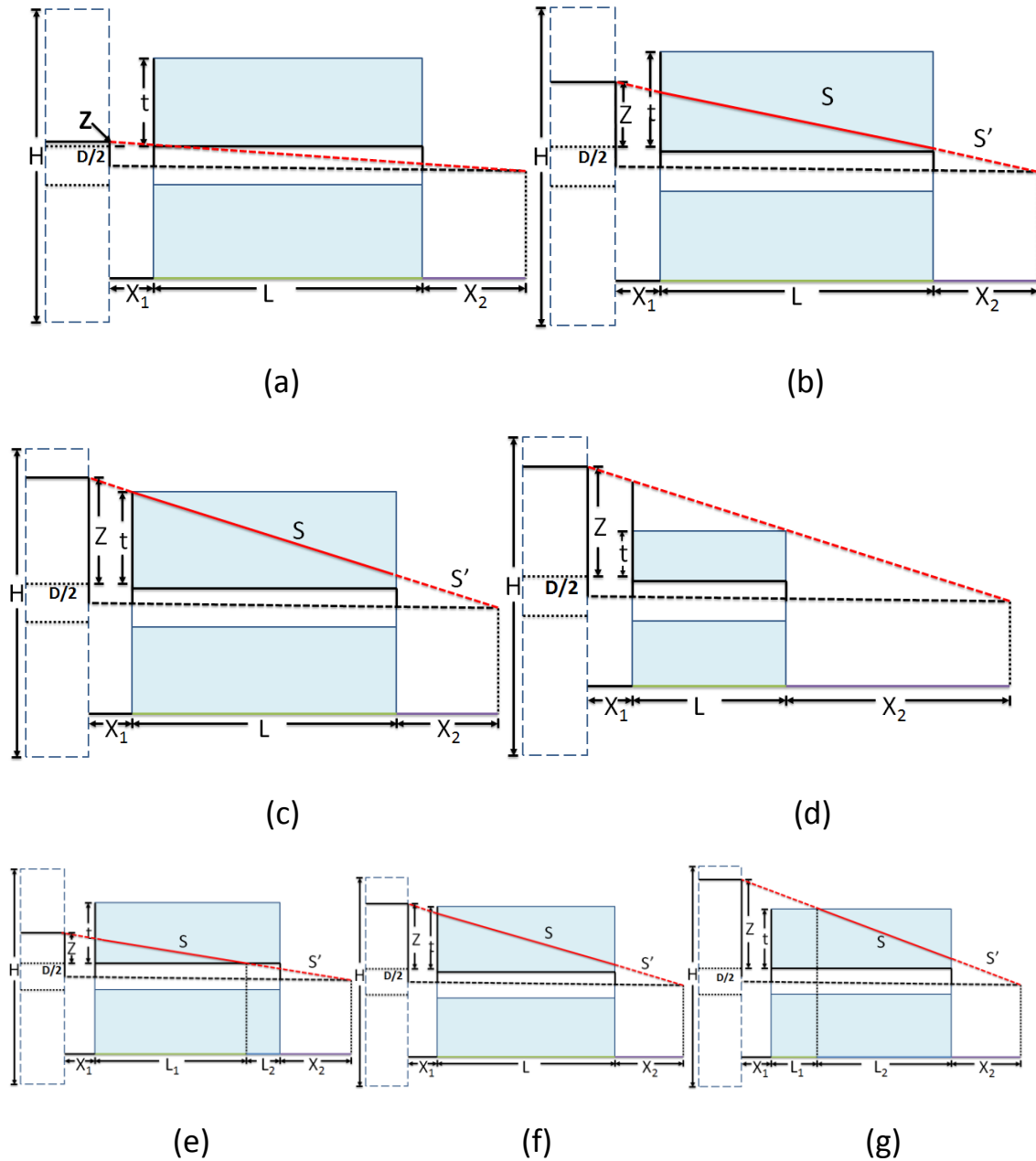


Figure C.3: Demonstration of different situations and orientations of annihilation photons entrance to collimator. (a) the limit of Z when annihilation photons from the source go through the pin-hole tunnel without entering collimator; (b) the limit of Z when annihilation photons directly go through collimator material without entering the pin-hole area; (c) after this limit of Z , the attenuated length, S (the solid red lines) starts to decrease with increasing Z ; (d) while Z increases, annihilation photons might eventually shoot into crystal without being attenuated by collimator if the crystal is tall enough (or the collimator is not thick enough); (e) (f) (g) are situations of incoming annihilation photons among limit conditions of (a)-(b), (b)-(c), (c)-(d), respectively.

As demonstrated in Figure C.3, as the distance Z increases, the attenuation length of annihilation photons within collimator, or S , increases from zero to a maximum value (Figure C.3 (c)) and then decreases back to zero (Figure C.3 (d)). For a point source and constant values for X_1 , X_2 , D and L , the limit value of Z which corresponds to the case of incidence rays entering the tunnel prior to interacting with collimator materials (Figure C.3 (a)) is:

$$Z_{\text{limit}1} = \frac{D}{2} \cdot \frac{X_1}{L + X_2} \quad (\text{C.1})$$

Note that for region of $0 < Z < Z_{\text{limit}1}$, all annihilation photons directly shoot to crystal through tunnel without interacting with collimator materials.

here is a second limit value of Z (Figure C.3 (b)) representing the lower bound of those annihilation photons that directly enter collimator material zone, as shown below:

$$Z_{\text{limit}2} = \frac{D}{2} \cdot \frac{X_1 + L}{X_2} \quad (\text{C.2})$$

For the next region as shown in Figure D.3 (c), the attenuation length keeps on increasing along with Z until it reaches another limit, $Z_{\text{limit}3}$:

$$Z_{\text{limit}3} = \left(t + \frac{D}{2} \right) \cdot \frac{X_1 + X_2 + L}{X_2 + L} - \frac{D}{2} \quad (\text{C.3})$$

Once beyond $Z_{\text{limit}3}$, the attenuation length S continuously decreases to zero with increasing Z and reaches the final bound, $Z_{\text{limit}4}$ (Figure C.3 (d)):

$$Z_{\text{limit}4} = \left(t + \frac{D}{2} \right) \cdot \frac{X_1 + X_2 + L}{X_2} - \frac{D}{2} \quad (\text{C.4})$$

For those layers of Z greater than $Z_{\text{limit}4}$, no annihilation photon is to be attenuated by collimator and these layers are thus exposed to the source directly.

Eventually, the attenuation lengths for those individual regions between each boundary are calculated based on the previously defined limiting boundaries of Z :

- 1) For the region of $Z_{\text{limit}1} \leq Z < Z_{\text{limit}2}$ (Figure C.3 (e)),

$$S = \frac{X_2 + L}{\sqrt{1 - \left(\frac{Z + \frac{D}{2}}{r} \right)^2}} - \frac{D}{2Z + D} \cdot r \quad (\text{C.5})$$

2) For the region of $Z_{\text{limit}2} \leq Z < Z_{\text{limit}3}$ (Figure C.3 (f)),

$$S = \frac{L}{\sqrt{1 - \left(\frac{Z + \frac{D}{2}}{r} \right)^2}} \quad (\text{C.6})$$

3) For the region of $Z_{\text{limit}3} \leq Z < Z_{\text{limit}4}$ (Figure C.3 (g)),

$$S = \frac{r}{X_1 + X_2 + L} \cdot \left[\frac{\left(t + \frac{D}{2} \right) (X_1 + X_2 + L)}{Z + \frac{D}{2}} - X_2 \right] \quad (\text{C.7})$$

where r is the total distance from the source to the point of incidence of annihilation photons (“ Z ” from tunnel) in the crystal (the total length of the dashed and solid red line in Figure C.3) and is always equal to:

$$r = \sqrt{(X_1 + X_2 + L)^2 + \left(Z + \frac{D}{2} \right)^2} \quad (\text{C.8})$$

According to the Beer’s law, the remaining of intensity of annihilation photons due to attenuation only follows an exponential manner (Eq. 1.2).

C.2.2 Build-up factor

Another factor being taken into account is the “built-up factor”, which is associated with the contribution of scattered annihilation photons inside the collimator [Cherry et al. 2003]. It is also called “B-factor” and depends on annihilation photon energy, shield material, and thickness. The build-up factors for lead material at various energies are reported in literatures [Cherry et al. 2003, Schleien *et al.* 1992] and those values are interpolated to derive the value for the energy of 511 keV.

$$B = 1.0924e^{0.1323\mu S} \quad (\text{C.9})$$

where S is to be calculated for various situations outlined in formulae Eq. C.5, Eq. C.6, and Eq. C.7.

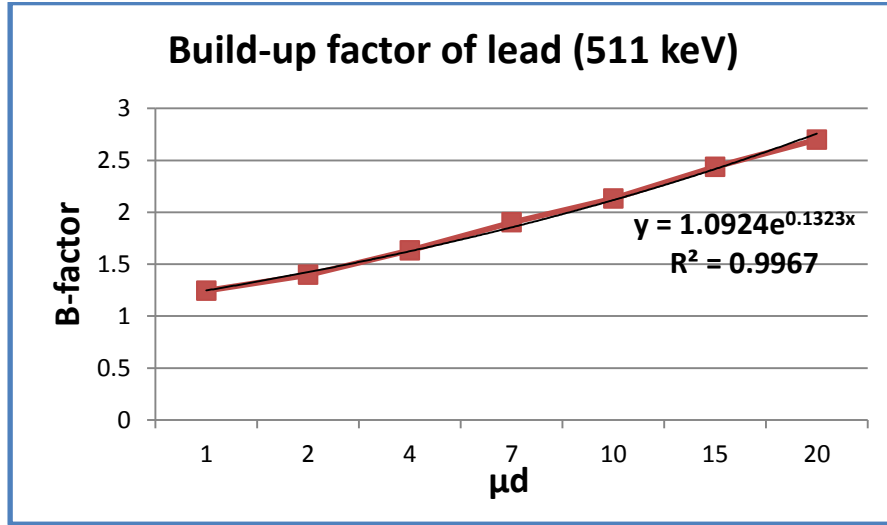


Figure C.4: The plot and best-fitted equation of build-up factors.

Therefore, the overall residual intensity of a beam of annihilation photons after propagating through a collimator at a specific scenario is the combination of the attenuation and the build-up effect:

$$I_t = B \cdot I = I_0 B e^{-\mu S} = 1.0924 I_0 e^{(0.1323-1)\mu S} \quad (\text{C.10})$$

It should be pointed out that even though the contribution from the build-up factor (i.e., scattered annihilation photons with reduced energy) may be removed by applying an energy gating, the calculation here gives us a conservative estimation. I_t/I_0 is the chance of survival for one annihilation photon after traveling along this path, “ S ”. Hence, Eq. C.10 is a quantitative way to investigate the survival probability of a annihilation photon.

C.2.3 Inverse-square-law

In addition to attenuation effects by collimators, the intensity of annihilation photons is also naturally reduced along the path of propagation by the inverse-square law shown in Figure C.5. For instance, the intensity of annihilation photons that only go through tunnel is also reduced even if there is no collimator presents. Note that all the developed equations of attenuation S have an intrinsic inverse-square term (i.e. “ r ”). So I_t is the combination of I_c and I_i :

$$I_t = I_c \cdot I_i \quad (\text{C.11})$$

where I_c and I_i are the contributions of reduction of intensity from collimator and inverse-square-law, respectively. Therefore the I_i term is separated from I_t in order to study the relative contribution of reduction of intensity only due to the collimator.

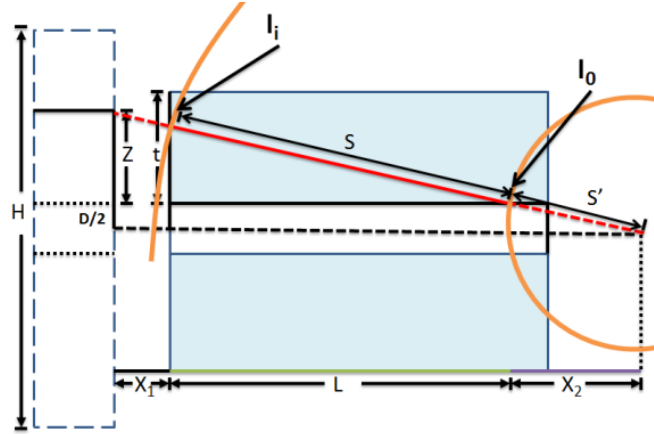


Figure C.5: Scheme of inverse-square law contribution to reduction of intensity. The orange curves represents solid-angle spheres with two radii (S and $S+S'$).

The ratio of the intensities at r equates to S and $S+S'$ is:

$$\frac{I_i}{I_0} = \frac{S'^2}{(S+S')^2} \quad (\text{C.12})$$

So similar to calculations of S (Eq. C.5, Eq. C.6, and Eq. C.7) for different boundary regions, values of S' at those situations have to be determined and their equations are shown as follows:

- 1) For the region of $Z_{\text{limit1}} \leq Z < Z_{\text{limit2}}$ (Figure C.3 (e)),

$$S' = \frac{D}{2Z + D} \cdot r \quad (\text{C.13})$$

- 2) For the regions of $Z_{\text{limit2}} \leq Z < Z_{\text{limit3}}$ (Figure C.3 (f)) and of $Z_{\text{limit3}} \leq Z < Z_{\text{limit4}}$ (Figure C.3 (g)),

$$S' = \frac{X_2}{X_1 + X_2 + L} \cdot r \quad (\text{C.14})$$

Finally, the entire lead collimator is designed as a combination of two lead disc pieces (due to shape and size of the mounting device on the drilling machine) together so that the size of tunnel is as fine as possible without compromising the length of the collimator too much (Figure C.6).

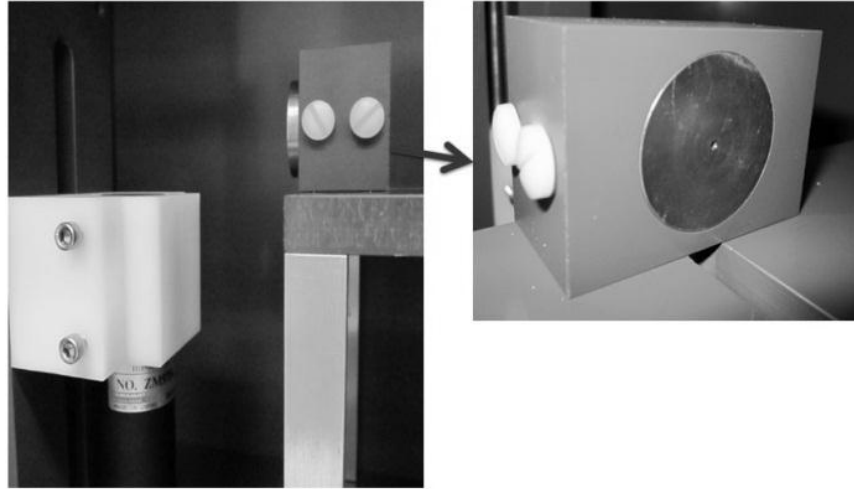


Figure C.6: The final design of the collimator and its removable holder. After balancing the trade-off between size of drill head and length of drill (due to constraint of drill), the 1mm diameter of drill head with a length of 5/8 inch is selected, and this leads to total length of 5/4 inch (or 3.175 cm). The “thickness” t is then defined as the difference between outer diameter of collimator and diameter of the tunnel divided by 2, i.e. $\frac{OD-D}{2} = \frac{28.575\text{mm} - 1\text{mm}}{2} = 1.37875\text{cm}$.

Table C.1 lists length and thickness of the designed collimator, as well as different limitations of Z assuming the X_1 and X_2 are both equal to 5 cm.

Table C.1: Parameters of collimator and limitations of Z of the four boundary conditions for $X_1=X_2=5\text{cm}$.

L (cm)	t (cm)	Z_{limit1} (cm)	Z_{limit2} (cm)	Z_{limit3} (cm)	Z_{limit4} (cm)
3.1750	1.3788	0.0306	0.0818	2.2526	3.7148

Based on the parameters listed in the above table, the results of the total reduction of intensity (I_t/I_0), as well as the reduction of intensity only due to the collimator (I_C/I_0) and the inverse square law (I_i/I_0) are plotted in Figure C.7.

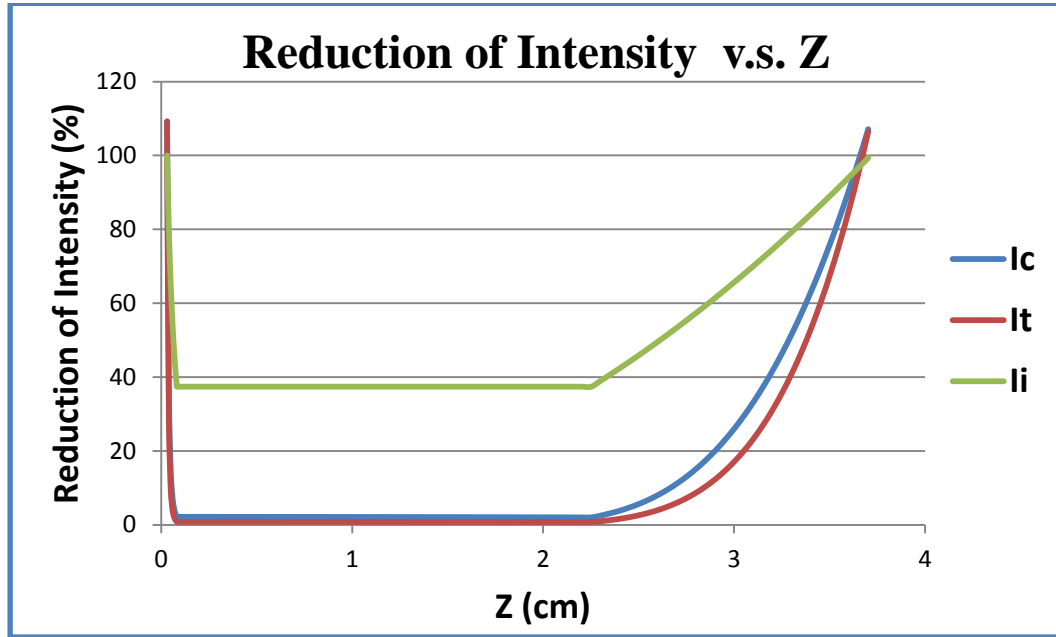


Figure C.7: The plot of I_i/I_0 , I_c/I_0 and I_t/I_0 versus different Z for $X_1=X_2=5$ cm. At boundary $Z_{\text{limit}1}$ (or 0.0306 cm) the ratio of total residual intensity after propagating through the collimator before entering the collimator is 109%. It is because the attenuation length is zero and the scattered photons play a role. The intensity eventually increases back to 109% which is the situation where S is equal to zero. The collimator has less power to stop annihilation photons entering to higher undesired layers, although in reality such long scintillation crystal is rarely being used (usually no more than 30 mm).

As shown in Figure D.7, the collimator plays an important role to attenuate intensity of annihilation photons. The intensity of remaining penetrated annihilation photons is relatively significant at the two opposing edges of collimators (i.e. when Z is around $Z_{\text{limit}1}$ and $Z_{\text{limit}4}$). The total residual intensity (I_t) is reduced to be less than 1% of the initial intensity with Z equates to 0.08cm results in a 0.16cm of undesired layer due to the symmetric property. For example, if the annihilation photons are expected to be collimated and directed to the bottom layer of a crystal having a height of 20 mm (Figure C.8), the selected layers for DOI experiments (or DOI resolution) are recommended to be greater than 2.6 mm since the tunnel has an outer diameter of 1mm. In this case, the residual intensity in the remaining part of this 20 cm long crystal (i.e. 1.74 cm) is negligible according to Figure C.7.

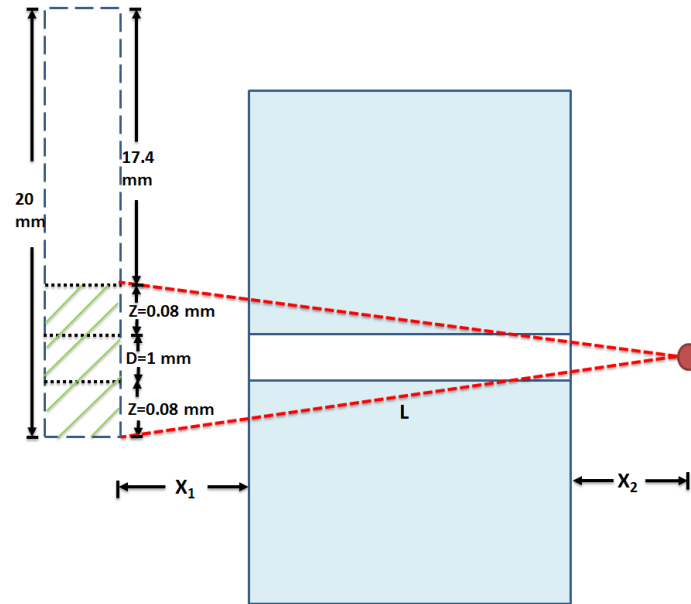


Figure C.8: Example of recommended DOI resolutions (the green region) for DOI experiment when annihilation photons are required to enter only the bottom layer of a 20 mm height crystal for $X_1=X_2=5$ cm.

In conclusion, an analytical model was developed to assist the design of a collimator to be used for future DOI studies. With the optimized conjugation, the regions of the scintillation crystal outside of the central region covered by the pin-hole will have a small amount of irradiation (less than 1%). Consequently, this would help us investigate the DOI resolution of ~ 5 mm or less, and answer the question how the time resolution depends on the interaction position within the crystal as discussed in section 1.2.3.3 [Spanoudaki and Levin 2011].

Bibliography

1. Allemand R, Gresset C, Vacher J. "Potential Advantages of a Cesium Fluoride Scintillator for a Time-of-Flight Positron Camera", *J Nucl Med*, Vol. 2, No. 2: p. 153-155, 1980
2. Allison J, Amako K, Apostolakis J, Araujo H, Arce Dubois P, Asai M, Barrand G, Capra R, Chauvie S, Chytracsek R, Cirrone GAP, Cooperman G, Cosmo G, Cuttone G, Daquino GG, Donszelmann M, Dressel M, Folger G, Foppiano F, Generowicz J, Grichine V, Guatelli S, Gumplinger P, Heikkinen A, Hrivnacova I, Howard A, Incerti S, Ivanchenko V, Johnson T, Jones F, Koi T, Kokoulin R, Kossov M, Kurashige H, Lara V, Larsson S, Lei F, Link O, Longo F, Maire M, Mantero A, Mascialino B, McLaren I, Mendez Lorenzo P, Minamimoto K, Murakami K, Nieminen P, Pandola L, Parlati S, Peralta L, Perl J, Pfeiffer A, Pia MG, Ribon A, Rodrigues P, Russo G, Sadilov S, Santin G, Sasaki T, Smith D, Starkov N, Tanaka S, Tcherniaev E, Tome B, Trindade A, Truscott P, Urban L, Verderi M, Walkden A, Wellisch JP, Williams DC, Wright D, Yoshida H, "Geant4 developments and applications", *IEEE Trans Nucl Sci* Vol. 53(1), p. 270-278, 2006
3. Aykac M, Bauer F, Williams C W, Loope M, and Schmand M, "Timing Performance of Hi-Rez Detector for Time-of-Flight (TOF) PET", *IEEE Trans. Nucl. Sci*, Vol. 53, No. 3, June 2006
4. Bailey D. L., Townsend D. W., Valk P. E and Maisey M. N., "Positron Emission Tomography Basic Sciences", Springer Verlag Berlin London Limited, 2005
5. Bauer F, Corbeil J, Schmand M, and Henseler D, "Measurements and Ray-Tracing Simulations of Light Spread in LSO Crystals", *IEEE Trans Nucl. Sci*, Vol. 56, NO. 5, October 2009
6. Beyer T., Kinahan, P. E., Townsend, D. W., and Sashin, D., "The use of X-ray CT for attenuation correction of PET data", *IEEE Trans. Nucl. Sci.*, Vol. 42, p. 1573–1577, 1995
7. Bielajew A F, Hirayama H, Nelson W R, and Rogers D W O, "History, overview and recent improvements of EGS4", Conference on Radiation Transport Calculations Using the EGS4, June 1994
8. Binkley D M, "Optimization of Scintillation-Detector Timing Systems Using Monte Carlo Analysis", *IEEE Trans. Nucl. Sci*. Vol. 41 p.386-393, 1994
9. Bones P J and Maclaren J R, "A physical Shepp-Logan head phantom for MRI", Proceedings of Image and Vision Computing, New Zealand, December 2007
10. Bonifacio D A B, Belcari N, Moehrs S, Moralles M, Rosso V, Vecchio S, and Del Guerra A, "A Time Efficient Optical Model for GATE Simulation of a LYSO Scintillation Matrix Used in PET Applications", *IEEE Trans. Nucl. Sci*. Vol. 57, No. 5, October 2010
11. Briesmeister JF (ed) "MCNP A General Monte Carlo N Particle Transport Code", Version 4C., Los Alamos National Laboratory, 2000
12. Budinger T. F., "Time-of-Flight Positron Emission Tomography: Status Relative to Conventional PET", *J Nucl Med*. Vol 24, No. 1, p. 73-78, June 7-10, 1983
13. CAEN, "MOD. V1721-V1731 Technical Information Manual", Revision n.21, pp.33, 06 February 2012, CAEN
14. Carrier C, Martel C, Schmitt C, Lecomte R., "Design of a high-resolution positron emission tomograph using solid scintillation detectors", *IEEE Trans Nucl Sci*, Vol. 35, No. 1, p. 685-690, 1988
15. Cayouette F, Laurendeau D and Moisan C, "DETECT2000: An Improved Monte-Carlo Simulator for the Computer Aided Design of Photon Sensing Devices", Proc. SPIE Photonic North, June 2002
16. Cherry S R and Dahlbom M, "PET: Physics, Instrumentation, and Scanners", Springer Science Business Media, 2006
17. Cherry S R, Shao Y, Tornai M P, Siegel S, Ricci A R, Phelps M E, "Collection of Scintillation Light from Small BGO Crystals", *IEEE Trans. Nucl. Sci.*, vol. 42, No.4, pp. 1058-1063, August 1995

18. Cherry S. R., Sorenson J. A., and Phelps M.E., "Physics in Nuclear Medicine", 3rd ed. Saunders, 2003
19. Chung Y H, Hwang J Y, Baek C H, An S J, Kim H I, Kim K H, "TraPET: High performance small animal PET with trapezoidal phoswich detector", Nucl. Instr. Methods Phys. Res. A 652, p.802-805, 2011
20. Clinthorne N H, Petrick N A, Rogers W L, and Hero A O, "A Fundamental Limit on Timing Performance with Scintillation Detectors", IEEE Trans. Nucl. Sci. 73 p.658-63, 1990
21. Codino A, "The pulse digitization for measuring the time of flight of ionizing particles", Nucl. Instrum. Methods Phys. Res. A, 440 pp. 191-201, 2000
22. Degenhardt C, Prescher G, Frach T, Thon A, de Gruyter R, Schmitz A, and Ballizany R, "The digital silicon photomultiplier - a novel sensor for the detection of scintillation light," in 2009 IEEE Nucl. Sci. Symp. Conf. Record, pp. 2383 –2386, 2009
23. Derenzo S E, Weber M J, Courchesne E B, Klintonberg M K, "The quest for the ideal inorganic scintillator", Nucl Instr. Meth. Phys Res A. 505, p.111-117, 2003
24. Dolgoshein B, "SILICON PHOTOMULTIPLIERS IN PARTICLE PHYSICS: POSSIBILITIES AND LIMITATIONS", World Scientific Publishing Co. Pte. Ltd., pp. 442-456, 2004
25. Dorenbos P, "Light output and energy resolution of Ce³⁺-doped scintillators", Nucl. Instrum. Methods Phys. Res. A 486 p. 208-213, 2002
26. Dorenbos P, de Haas J T M, van Eijk C W E, "Nonproportionality in the Scintillation Response and the Energy Resolution Obtainable with Scintillation Crystals", IEEE Trans. Nucl. Sci. Vol 42, No. 6, p. 2190-2202, December 1995
27. Du H, Yang Y, Glodo J, Wu Y, Shah K and Cherry S R, "Continuous depth-of-interaction encoding using phosphor-coated scintillators", Phys. Med. Biol., Vol. 54, p. 1757–1777, 2009
28. Eriksson L, Melcher C L, Zhuravleva M, Eriksson M, Rothfuss H, Conti M, "Phoswich solutions for the PETDOI problem", Nucl. Instr. and Meth. A Vol. 648, S1, p. S288-S292, 2010
29. Frach T, Prescher G, Degenhardt C, de Gruyter R, Schmitz A, and Ballizany R, "The digital silicon photomultiplier - principle of operation and intrinsic detector performance," in 2009 IEEE Nucl. Sci. Symp. Conf. Record, pp. 1959 –1965, 2009
30. Heinrichs U, Blume A, Bumann N, Engels R, Kemmerling G, Weber S, and Ziemons K, "Statistical studies on the light output and energy resolution of small LSO single crystals with different surface treatments combined with various reflector materials," Nucl. Instrum. Methods Phys. Res. A, vol. A486, pp. 60–66, 2002
31. Heiss W-D, Habedank B, Klein J C, Herholz K, Wienhard K, Lenox M and Nutt R, "Metabolic rates in small brain nuclei determined by high-resolution PET", *J. Nucl. Med.* 45 p. 1811–1815, 2004
32. Hu W, Choi Y, Hong K J, Kang J, Jung J H, Huh Y S, Lim H K, Kim S S, Min B J, Kim B T, "A simple and improved digital timing method for positron", Nucl. Instrum. Methods Phys. Res. A, 622 pp. 219-224, 2010
33. Huber J S, Moses W W, Andreaco M S, Loope M, Melcher C L, Nutt R, "Geometry and surface treatment dependence of the light collection from LSO crystals", Nucl. Instr. Methods Phys. Res. A 437, p.374-380, 1999
34. Humm J, Rosenfeld A, and Del Guerra A, "From PET detectors to PET scanners", *Eur. J. Nucl. Med. Mol. Imaging*, Vol. 30, No. 11, p. 1574-1597, 2003
35. Ito M, Lee J S, Park M-J, Sim K-S and Hong S J, "Design and simulation of a novel method for determining depth-of-interaction in a PET scintillation crystal array using a single-ended readout by a multi-anode PMT", *Phys. Med. Biol.*, Vol. 55, p. 3827–3841, 2010

36. James S S, Yang Y, Wu Y, Farrell R, Dokhale P, Shah K S, Cherry S R, “Experimental characterization and system simulations of depth of interaction PET detectors using 0.5 mm and 0.7 mm LSO arrays”, *Phys. Med. Biol.*, Vol. 54, p. 4605-4615, 2009
37. Janecek M, and Moses W W, “Optical Reflectance Measurements for Commonly Used Reflectors”, *IEEE Trans Nucl. Sci.*, Vol. 55, No. 4, August 2008
38. Janecek M and Moses W W, “Simulating Scintillator Light Collection Using Measured Optical Reflectance”, *IEEE Trans. Nucl. Sci.*, 57, 3, 964 - 970, June 2010
39. Jarron P, Auffray E, Brunner S E, Despeisse M, Garutti E, Goettlich M, Hillemanns H, Lecoq P, Meyer T, Powolny F, Shen W, Coulon H C S, Williams C, “Time based readout of a silicon photomultiplier (SiPM) for Time Of Flight Positron Emission Tomography (TOF-PET)”, *IEEE Nucl. Sci. Symp. Conf. Rec.*, 2009
40. Karp J S, Kuhn A, Perkins A E, Surti S, Werner M E, Witherspoon M E D, Popescu L, Vandenberghe S, Muehlelehner G, “Characterization of a Time-of-Flight PET Scanner based on Lanthanum Bromide”, *IEEE Nucl. Sci. Symp. Conf. Rec.*, 2005
41. Kapusta M, Moszyński M, Balcerzyk M, Braziewicz J, Wolski D, Pawelke J, Klamra W, “Comparison of the scintillation properties of LSO:Ce manufactured by different laboratories and of LGSO:Ce”, *IEEE Trans. Nucl. Sci.* Vol 47, No. 4, p. 1341-1345, Aug 2000
42. Karp J. S., Surti S, Witherspoon M E D, and Muehlelehner G, “Benefit of Time-of-Flight in PET: Experimental and Clinical Results”, *J Nucl Med*, Vol. 49, No. 3, March 2008
43. Kelly G G, Bell P R, Davis R C and Lazar N A, “Intrinsic energy resolution”, *IRE Trans. on Nucl. Sci.*, NS3, p. 57–58, 1956
44. Knoll G F, “Radiation Detection and Measurements”, 3rd Edition, John Wiley & Sons, In., 2000
45. Knoll G F, Knoll T F, and Henderson T M, “light collection scintillation detector composites for neutron detection”, *IEEE Trans on Nucl. Sci.*, Vol. 35, No. 1, p. 872-875, February 1988
46. Kuhn A, Surti S, Karp J S, Raby P S, Shah K S, Perkins A E and Muehlelehner G, “Design of a lanthanum bromide detector for time-of-flight PET”, *IEEE Trans. Nucl. Sci.*, Vol. 51 p. 2550–2557, 2004
47. Kuntner C, Aiginger H, Auffray E, Glodo J, Kapusta M, Lecoq P, Moszynski M, Schneegans M, Szupryczynski P, Wojtowicz AJ. “Scintillation properties and mechanism in Lu_{0.8}Y_{0.2}AlO₃:Ce”, *Nucl Instrum Methods Phys Res A.*; 486: 176–180, 2002
48. Labruyere A F, Tan H, Hennig W, and Warburton W K, “Time Resolution Studies using Digital Constant Fraction Discrimination”, *Nucl. Instrum. Methods Phys. Res. A*, Vol. 579, pp. 247-251, 2007
49. Labsphere, “A Guide to Reflectance Coatings and Materials”, *Labsphere, Reflections Newsletter*, pp. 8-11, Sep. 1998
50. Lecomte R, “Novel detector technology for clinical PET”, *Eur. J. Nucl. Med. Mol. Imaging*, vol. 36, no. Suppl. 1, p. 69-85, 2009
51. Lempicki A and Glodo J, “Ge-doped scintillators: LSO and LuAP”, *Nucl. Instr. And Meth.*, vol. 416, No. 2-3, p. 333-344, 1998
52. Lempicki A, Wojtowicz A J, and Berman E, “Fundamental limits of scintillator performance”, *Nucl. Instrum. Methods Phys. A* 333, p. 304–311, 1993
53. Levin C S, “Design of a high resolution and high sensitivity scintillation crystal array for PET with nearly complete light collection”, *IEEE Trans. Nucl. Sci.*, Vol. 45, p. 2236-2243., 2002
54. Lewellen TK, Bice AN, Harrison RL, Pencke MD, Link JM, “Performance Measurements of the SP3000/UW Time-of-Flight Positron Emission Tomograph”, *IEEE Trans Nucl Sci.*; Vol. 35, No. 1, p. 665-669. 1988

55. Ling T, Burnett T H and Miyaoka R S, "Parametric positioning of a continuous crystal PET detector with depth of interaction decoding", *Phys. Med. Biol.* Vol. 53, p. 1843–1863, 2008
56. Liu S, Li H, Zhang Y, Ramirez R A, Baghaei H, An S, Wang C, Liu J, and Wong W H, "Monte Carlo Simulation Study on the Time Resolution of a PMT-Quadrant-Sharing LSO Detector Block for Time-of-Flight PET", *IEEE Trans. Nucl. Sci.* Vol. 56, No. 5, October 2009
57. Ludziejewski T, Moszynska K, Moszynski M, Wolski D, Klamra W, Norlin L, Devitsin E, Kozlov V, "Advantages and limitations of LSO scintillator in nuclearphysics experiments", *IEEE Trans Nucl Sci.*, vol. 42, p. 328-336, 1995
58. Maas M C, Schaart D R, van der Laan D J, Bruyndonckx P, Lemaitre C, Beekman F J and van Eijk C W E. "Monolithic scintillator PET detectors with intrinsic depth-of-interaction correction", *Phys. Med. Biol.*, 54. 1893–908, 2009
59. Magdy M and Khalil, "Basic sciences of nuclear medicine", Springer Verlag Berlin Heidelberg, 2011
60. Marx E and Vorburger TV, "Direct and inverse problems for light scattered by rough surfaces", *Applied Optics*, Vol. 29, No. 25, p. 3613-3626, September 1990
61. Mazoyer B, Trebossen R, Schoukroun C et al. "Physical Characteristics of TTV03, a New High-Spatial-Resolution Time-of-Flight Positron Tomograph", *IEEE Trans Nucl Sci*, Vol. 37, No. 2, p. 778-782, 1990
62. Melcher C L, "Scintillation Crystals for PET", *J Nucl Med*, Vol. 41, pp. 1051-1055, 2000
63. Melcher C L and Schweitzer J S, "Cerium-doped Lutetium Oxyorthosilicate: A Fast, Efficient New Scintillator", *IEEE Trans. Nucl. Sci.* Vol 39, No. 4, p. 502-505, Aug 1992
64. Meschede D, "Optics, light and lasers: The Practical Approach to Modern Asepects of Photonics and Laser Physics", Chapter 10, 2nd edition, 2007
65. Moisan C, Cayouet F and McDonald G, "DETECT2000 The Object Oriented C++ Language Version of DETECT A Program for Modeling Optical Properties of Scintillators", Laval University, Quebec City, Quebec, Canada, September 2007
66. Moisan C, Levin A and Laman H, "Testing scintillation transport models with photoelectron yields measured under different surface finishes", *IEEE Nucl. Sci. Symp. Conf. Record 1* p. 824-828, 1997
67. Moisan C, Vozza D and Loope M, "Simulating the performances of an LSO based position encoding detector for PET" *IEEE Nucl. Sci. Symp. Conf. Record*, 1996
68. Moses W W, "Recent advances and future advances in time-of-flight PET", *Nucl. Instrum. Methods Phys. Res. A* 580, p. 919–924, 2007
69. Moses WW, "Current trends in scintillator detectors and materials", *Nucl Instrum Methods Phys Res A.*, 487, p.123-128, 2002
70. Moses W.W., Derenzo S.E., "Empirical observation of resolution degradation in positron emission tomographs utilizing block detectors", *J. Nucl. Med.*, Vol. 34, p. 101, 1993
71. Moses W W and Derenzo S E, "Scintillators for Positron Emission Tomography", *Proceedings of The Scint '95*, pp.234-237, (Edited by P. Dorenbos and C. W. E. v. Eijk Delft, The Netherlands, 1996)
72. Moses W W and Derenzo S E, "Prospects for time-of-flight PET using LSO scintillator", *IEEE Trans. Nucl. Sci.* Vol 46, No. 3, p. 474-478, June 1999
73. Moses W W and Ullisch M, "Factors Influencing Timing Resolution in a Commercial LSO PET Camera", *IEEE Trans. Nucl. Sci.* Vol. 53 p.78-85, 2006
74. Mosset J.B., Devroede O., Krieguer M., Rey M., Vieira J.M., Jung J.H. "Development of an optimized LSO/LuYAP phoswich detector head for the lausanne clearPET demonstrator", *IEEE Trans. Nucl. Sci.*, Vol. 53, p. 25-29, 2006

75. Moszynski M, Kapusta M, Nassalski A, Szcze,śniak T, Wolski D, Eriksson L and Melcher C L, “New Prospects for Time-of-Flight PET With LSO Scintillators”, *IEEE Trans. on Nucl. Sci.*, Vol. 53, No. 5, 2006
76. Moszynski M, Ludziejewski T, Wolski D, Klamra W and Avdejchikov V V, “Timing properties of GSO, LSO and other Ce doped scintillators”, *Nucl. Instrum. Methods Phys. Res. A* 372 p. 51–58, 1996
77. Motta D, Buck C, Hartmann F X, Lasserre Th, Schönert S, and Schwan U, “Prototype scintillator cell for an In-based solar neutrino detector”, *Nucl. Instr. Meth. Phys. Res. A*, Vol. 547, p. 368–388, 2005
78. Motta D and Schönert S, “Optical properties of bialkali photocathodes,” *Nucl. Instrum. Methods Phys. Res. A*, vol. A539, pp. 217–235, Feb. 2005
79. Nayar S K, Ikeuchi K, and Kanade T, “Surface Reflection: Physical and Geometrical Perspectives”, The Robotics Institute, Carnegie Mellon University, Pittsburgh, Pennsylvania, March 1989
80. Nelson M A, Rooney B D, Dinwiddie D R, Brunson G S, “Analysis of digital timing methods with BaF2 scintillators”, *Nucl. Instrum. Methods Phys. Res. A*, 505 pp. 324-327, 2003
81. ORTEC, “Fast-Timing Discriminator Introduction”, ORTEC
82. Pedroso de Lima J J, “Nuclear Medicine Physics Series in Medical Physics and Biomedical Engineering”, Springer Verlag Berlin Heidelberg, 2011
83. Pepin C, Bérard P and Lecomte R, “Assessment of reflective separator films for small crystal arrays”, *IEEE NSS Conf. Rec.*, Vol. 2, iss. 4-10, p. 879-883, 2001
84. Pepin C M, Berard P, Perrot AL, Pepin C, Houde D, Lecomte R, Melcher C, Dautet H, “Properties of LYSO and recent LSO scintillators for phoswich PET detectors”, *IEEE Trans Nucl Sci.*, vol. 51, p789-795, 2004
85. Peng H and Levin C S., “Recent Developments in PET Instrumentation”, *Curr Pharm Biotechnol.*, Vol. 11, No. 6, p.555-571, 2010
86. Peng H, Olcott P D, Foudray A M K, and Levin C S, “Evaluation of free-running ADCs for high resolution PET data acquisition”, *IEEE Nucl. Sci. Symp. Conf. Rec.*, 2007
87. Peng H, Olcott P D, Spanoudaki V, Levin C S, “Investigation of a clinical PET detector module design that employs large-area avalanche Photodetectors”, *Phys. Med. Biol.* 56 p. 3603–3627, 2011
88. Petrick N, Clinthorne N H, Rogers L W and Hero A O, “First photoelectron timing error evaluation of a new scintillation detector model”, *IEEE Trans. Nucl. Sci.* Vol. 38 174–7, 1991
89. Pichler B J, Boning G, Rafecas M, Schlosshauner M, Lorenz E, Ziegler S I, “LGSO Scintillation Crystals Coupled to New Large Area APDs Compared to LSO and BGO”, *IEEE Trans. Nucl. Sci.* Vol 46, No. 3, p. 289-291, June 1999
90. Pichler B J, Kolb A, Nāgele T, and Schlemmer H P, “PET/MRI: Paving the Way for the Next Generation of Clinical Multimodality Imaging Applications”, *J Nucl Med*, Vol. 51, No. 3, p. 333-336, March 2010
91. Pogossian M M T, Ficke DC, Hood JT, Sr., Yamamoto M, Mullani NA. *PETT VI*: “A Positron Emission Tomograph Utilizing Cesium Fluoride Scintillation Detectors”, *J Comput Assist Tomogr.* p. 125-133, 1982
92. Post R F and Schiff L I, “Statistical Limitations on the Resolving Time of a Scintillation Counter”, Stanford University, October 16, 1950
93. Prescott J R and Narayan G H, “Electron response and intrinsic line-widths in NaI(Tl) Crystals”, *Nucl. Instr. Meth.*, Vol. 75, p. 51–55, 1969
94. Qin L, Li H, Lu S, Ding D, Ren G, “Growth and characteristics of LYSO ($\text{Lu}_{2(1-x-y)}\text{Y}_{2x}\text{SiO}_5\text{:Ce}_y$) scintillation crystals”, *J Cryst Growth*, vol. 281, p518-524, 2005

95. Rafecas M, Boning G, Pichler B J, Lorenz E, Schwaiger M, Ziegler S I, "A monte carlo study of high resolution PET with granulated dual layer detectors", IEEE Trans Nucl. Sci., Vol. 48, p. 1490-1495, 2001
96. Renker D and E, "Advances in solid state photon detectors," Journal of Instrumentation, vol. 4, no. 04, p. P04004, 2009
97. Ros A, Lerche Ch W, Sanchez F, Ruiz J S, Marti R., Cantarero A, Sebastia A, Benloch M, "Impact of the scattering coefficient of scintillation crystals (LYSO and LSO) on depth of interaction resolution", IEEE Nucl. Sci. Symp. Conf. Record, p.3715-3718, 2008
98. Rothfuss H, Casey M, Conti M, Doshi N, Eriksson L, and Schmand M, "Monte Carlo Simulation Study of LSO Crystals", IEEE Trans Nucl. Sci, Vol. 51, No. 3, June 2004
99. Saha G. B., "Basics of PET Imaging Physics Chemistry and Regulations", 2nd Edition, Springer New York Dordrecht Heidelberg London, 2010
100. Saoudi A, Pepin C M, Dion F, Bentourkia M, Lecomte R, Andreaco M, Casey M, Nutt R, Dautet H, "Investigation of Depth-of-Interaction by Pulse Shape Discrimination in Multicrystal Detectors Read Out by Avalanche Photodiodes", IEEE Trans Nucl. Sci, Vol. 46, No. 3, June 1999
101. Saoudi A, Pepin C M and Lecomte R, "Study of Light Collection in Multi-Crystal Detectors", IEEE Trans Nucl. Sci, Vol. 47, No. 4, August 2000
102. Schaart D R, Seifert S, Vinke R, Dam H T van, Dendooven P, Löhner H, and Beekman F J, "LaBr₃:Ce and SiPMs for time-of-flight PET: achieving 100 ps coincidence resolving time," Phys. Med. Biol., Vol. 55, p. N179-N189, 2010
103. Schleien B, "The Health Physics and Radiological Health Handbook", Silver Spring, MD, Scinta, 1992
104. Schlemmer HP, Pichler BJ, Schmand M, et al., "Simultaneous MR/PET imaging of the human brain: feasibility study", Radiology, Vol. 248, p.1028–1035, 2008
105. Seifert S, Steenbergen J H L, van Dam H T, Vinke R, Dendooven P, Lohner H, Beekman F J, Drenbos P, van der Kolk E, Schaart D R, "Accurate Measurements of the Rise and Decay Times of Fast Scintillators with Solid State Photon Counters", IEEE NSS Conf. Rec., 2010
106. Seifert S, Vinke R, van Dam H T, Lohner H, Dendooven P, Beekman F J, Schaart D R, "Ultra Precise Timing with SiPM-Based TOF PET Scintillation Detectors", IEEE Nuclear Science Symp. Conf. Rec., p. 2329-2333, 2009
107. Shao Y P, "A new timing model for calculating the intrinsic timing resolution of a scintillator detector", Phys. Med. Biol., Vol. 52, p. 1103-1117, February 2007
108. Shirazi M A M, Swindell W, and Evans P M, "Optimization of the scintillation detector in a combined 3D megavoltage CT Scanner and portal imager", Medical Physics, Vol. 25, No. 10, p. 1880-1890, 1998
109. Spanoudaki V C, Mann A B, Otte A N, Konorov I, Torres-Espallardo I, Paulb S and Ziegler S I, "Use of single photon counting detector arrays in combined PET_MR Characterization of LYSO_SiPM detector modules and comparison with a LSO-APD detector", JOURNAL OF INSTRUMENTATION, 2: Art. No. P12002, December 2007
110. Spanoudaki V Ch and Levin C S, "Photo-Detectors for Time of Flight Positron Emission Tomography (ToF-PET)", 10, p. 10484-10505, Sensors, 2010
111. Spanoudaki V Ch and Levin C S, "Investigating the temporal resolution limits of scintillation detection from pixellated elements: comparison between experiment and simulation", Phys. Med. Biol. 56, p. 735-756, 2011
112. Spurrier M A, Szupryczynski P, Yang K, Carey A A, and Melcher C L, "Effects of Ca²⁺ co-doping on the scintillation properties of LSO:Ce", IEEE Trans. Nucl. Sci., vol. 55, no. 3, Part 2, p. 1178-1182, 2008

113. Steinbach C o, Ujhelyi F, Erdei G and Lorincz E, "Optical scattering length of LYSO scintillator crystals", IEEE Nucl. Sci. Symp. Conf. Rec., p. 2653-2656, 2011
114. Strother SC, Casey ME, Hoffman EJ., "Measuring PET scanner sensitivity: relating countrates to image signal-to-noise ratios using noise equivalent counts", IEEE Trans Nucl Sci, Vol. 37, No. 2, p.783-788, 1990
115. Strul D, Santin G, Lazaro D, Breton V, and Morel C, "GATE(Geant4 Application for Tomographic Emission): a PET/SPECT general-purpose simulation platform", Nuclear Physics 125, p.75-79, 2003
116. Surti S and Karp J S, "Experimental evaluation of a simple lesion detection task with Time-of-Flight PET", *J. Nucl. Med.*, 48, p. 471-480, 2007
117. Surti S, Kuhn Aa, Werner ME, Perkins AE, Kolthammer J, Karp JS. "Performance of Philips Gemini TF PET/CT Scanner with Special Consideration for Its Time-of-Flight Imaging Capabilities." *J Nucl Med*, Vol. 48, p.471-80, 2007
118. Tickener J, and Roach G, "PHOTON – An optical Monte Carlo code for simulating scintillation detector responses", *Nucl Instrum Methods Phys Res*, p. 149-155, April 2007
119. Torrance K E, Sparrow E M, " Theory of Off-Specular Reflection From Roughened Surfaces", *Journal of the Optical Society of America*, No. 57, p. 1105-1114, 1967
120. Townsend D W, Beyer T, Kinahan P E, Brun T, Roddy R, Nutt R, and Byars L G, "The SMART scanner: a combined PET/CT tomograph for clinical oncology". *IEEE NSS/MIC Conf. Rec.*, Vol. 2, pp. 1170–1174, 1998
121. Waldwick B, Chase C, and Chang B, "Increased efficiency and performance in laser pump chambers through use of diffuse highly reflective materials", in *Proc. SPIE*, vol. 6663, pp. 66630N.1-66630N.7, 2007
122. Weidner V R and Hsia J J, "Reflection Properties of Pressed Polytetrafluoroethylene Powder", *J Opt. Soc. Amer.*, Vol. 71, No. 7, p.856-861, 1981
123. Wernick M. N. and Aarsvold John N., "Emission Tomography The Fundamentals of PET and SPECT", Elsevier Academic Press, December 2004
124. Witherspoon M E. D, Surti S, Perkins A E, Kyba C C M, Werner M E, Matej S, and Karp S, "Imaging Performance of a LaBr3-Based Time-of-Flight PET Scanner", *IEEE Nucl. Sci. Symp. Conf. Rec.*, p. 5463-5467, 2008
125. Witherspoon M E D, Surti S, Perkins A, Kyba C C M, Wiener R, Werner M E, Kulp R and Karp J S, "The imaging performance of a LaBr3-based PET scanner" *Phys. Med. Biol.*, vol.55, p.45–64, 2010
126. Wong WH, "PET camera performance design evaluation for BGO and BaF2 scintillators (non time of flight)", *J Nucl Med* Vol. 29, No. 3, p. 338-347, 1988
127. Wong WH, Mullani NA, Philippe EA et al.. "Performance Characteristics of the University-of-Texas TOFPET-I PET Camera". *J Nucl Med*, Vol. 25, No. 5, p. 46-47, 1984
128. van Dam H T, Seifert S, Vinke R, Dendooven P, Lohner H, Beekman F J, Schaart D R, "Silicon Photomultiplier Response Model", *IEEE Nuclear Science Symp. Conf. Rec.*, 2009
129. van der Laan D J, Schaart D R, Maas M C, Beekman F J, Bruyndonckx P, and van Eijk C W E, "Optical simulation of monolithic scintillator detectors using GATE/GEANT4", *Phys. Med. Biol.*55, p1659-1675, February 2010
130. van Loef E, Dorenbos P, van Eijk C, Kramer K, and Guldel H, "High-energy-resolution scintillator: Ce³⁺ activated LaBr3", *Appl. Phys. Letters*, Vol. 79, No. 10, pp. 1573-1575, 2001
131. Vandenbroucke A, Levin C S, "Study of Scintillation Crystal Array Parameters for an Advanced PET Scanner Dedicated to Breast Cancer Imaging", *IEEE Nucl. Sci. Symp. Conf. Record*, p.4914-4919, 2008

132. Yang Y, Dokhale P A, Silverman RW, Shah K S, McClish M A, Farrell R, Entine G, Cherry S R, “Depth of interaction resolution measurements for a high resolution PET detector using position sensitive avalanche photodiodes”, *Phys. Med. Biol.*, Vol. 51, p. 2131-2142, 2006
133. Yang Y, Qi J, Wu Y, James S, St Farrell R, Dokhale P A, Shah K S and Cherry S R, “Depth of interaction calibration for PET detectors with dual-ended readout by PSAPDs”, *Phys. Med. Biol.*, Vol. 54, p. 433–445, 2009
134. Yang Y, Wu Y, Qi J, St James S, Du H, Dokhale PA, Shah KS, Farrell R, Cherry SR, “A prototype PET scanner with DOI encoding detectors”, *J Nucl Med*, Vol. 49, No. 7, p.1132-1140, 2008
135. Yuming, “Page Disussion”, Adjacent Buildings,
http://www.bembook.ibpsa.us/index.php?title=Adjacent_Buildings (1 July, 2012)
136. Zhang J, Olcott P D, Chinn G, Foudray A M K and Levin C S, “Study of the performance of a novel 1 mm resolution dual-panel PET camera design dedicated to breast cancer imaging using Monte Carlo simulation”, *Med. Phys.* 34 p. 689–702, 2007